13. N. Balakrishnan, A. Dalgarno, *Chem. Phys. Lett.* **341**, 652 (2001).
14. E. Bodo, F. A. Gianturco, A. Dalgarno, *J. Chem. Phys.* **116**, 9222 (2002).
15. D. W. Chandler, *J. Chem. Phys.* **132**, 110901 (2010).
16. P. F. Weck, N. Balakrishnan, *J. Chem. Phys.* **122**, 154309 (2005).
17. G. Quéméner, N. Balakrishnan, B. K. Kendrick, *J. Chem. Phys.* **129**, 224309 (2008).
18. B. Brutschy, H. Haberland, K. Schmidt, *J. Phys. B* **9**, 2693 (1976).
19. Q. Wei, I. Lyuksyutov, D. Herschbach, *J. Chem. Phys.* **137**, 054202 (2012).
20. L. Boltzmann, *Vorlesung Uber Gastheorie II* (J. A. Barth, Leipzig, Germany, 1989).
21. D. L. Bunker, N. Davidson, *J. Am. Chem. Soc.* **80**, 5085 (1958).
22. A. Schutte, D. Bassi, F. Tommasini, G. Scoles, *Phys. Rev. Lett.* **29**, 979 (1972).
23. J. P. Toennies, W. Welz, G. Wolf, *J. Chem. Phys.* **61**, 2461 (1974).
24. J. P. Toennies, W. Welz, G. Wolf, *J. Chem. Phys.* **71**, 614 (1979).
25. Ch. Buggle, J. Léonard, W. von Klitzing, J. T. M. Walraven, *Phys. Rev. Lett.* **93**, 173202 (2004).
26. N. R. Thomas, N. Kjaergaard, P. S. Julienne, A. C. Wilson, *Phys. Rev. Lett.* **93**, 173201 (2004).
27. S. Chefdeville et al., *Phys. Rev. Lett.* **109**, 023201 (2012).
28. E. P. Wigner, *Phys. Rev.* **73**, 1002 (1948).
29. J. M. Doyle, B. Friedrich, J. Kim, D. Patterson, *Phys. Rev. A* **52**, R2515 (1995).
30. C. D. Ball, F. C. De Lucia, *Phys. Rev. Lett.* **81**, 305 (1998).
31. B. R. Rowe, G. Dupeyrat, J. B. Marquette, P. Gaucherel, *J. Chem. Phys.* **80**, 4915 (1984).
32. I. W. M. Smith, *Angew. Chem. Int. Ed.* **45**, 2842 (2006).
33. Y. T. Lee, J. D. Mcdonald, P. R. Lebreton, D. Herschbach, *Rev. Sci. Instrum.* **40**, 1402 (1969).
34. C. Berteloite et al., *Phys. Rev. Lett.* **105**, 203201 (2010).
35. J. J. Gilijamse, S. Hoekstra, S. Y. T. van de Meerakker, G. C. Groenenboom, G. Meijer, *Science* **313**, 1617 (2006).
36. L. P. Parazzoli, N. J. Fitch, P. S. Żuchowski, J. M. Hutson, H. J. Lewandowski, *Phys. Rev. Lett.* **106**, 193201 (2011).
37. B. C. Sawyer, B. K. Stuhl, D. Wang, M. Yeo, J. Ye, *Phys. Rev. Lett.* **101**, 203203 (2008).
38. B. C. Sawyer et al., *Phys. Chem. Chem. Phys.* **13**, 19059 (2011).
39. R. H. Neynaber, in *Advances in Atomic and Molecular Physics*, D. R. Bates, E. Immanuel, Eds. (Academic Press, New York, 1969), vol. 5, pp. 57–108.
40. P. E. Siska, *Rev. Mod. Phys.* **65**, 337 (1993).
41. U. Even, J. Jortner, D. Noy, N. Lavie, C. Cossart-Magos, *J. Chem. Phys.* **112**, 8068 (2000).
42. K. Luria, N. Lavie, U. Even, *Rev. Sci. Instrum.* **80**, 104102 (2009).
43. S. Burdenski, R. Feltgen, F. Lichterfeld, H. Pauly, *Chem. Phys. Lett.* **78**, 296 (1981).
44. D. W. Martin, C. Weiser, R. F. Sperlein, D. L. Bernfeld, P. E. Siska, *J. Chem. Phys.* **90**, 1564 (1989).
45. K. T. Tang, J. P. Toennies, *J. Chem. Phys.* **80**, 3726 (1984).
46. D. T. Colbert, W. H. Miller, *J. Chem. Phys.* **96**, 1982 (1992).
47. N. Moiseyev, *Non-Hermitian Quantum Mechanics* (Cambridge Univ. Press, Cambridge, 2011).
48. F. Lique, G. Li, H. -J. Werner, M. H. Alexander, *J. Chem. Phys.* **134**, 231101 (2011).

An Ancient Core Dynamo in Asteroid Vesta

Roger R. Fu,[1]* Benjamin P. Weiss,[1] David L. Shuster,[2,3] Jérôme Gattacceca,[4] Timothy L. Grove,[1] Clément Suavet,[1] Eduardo A. Lima,[1] Luyao Li,[1] Aaron T. Kuan[5]

The asteroid Vesta is the smallest known planetary body that has experienced large-scale igneous differentiation. However, it has been previously uncertain whether Vesta and similarly sized planetesimals formed advecting metallic cores and dynamo magnetic fields. Here we show that remanent magnetization in the eucrite meteorite Allan Hills A81001 formed during cooling on Vesta 3.69 billion years ago in a surface magnetic field of at least 2 microteslas. This field most likely originated from crustal remanence produced by an earlier dynamo, suggesting that Vesta formed an advecting liquid metallic core. Furthermore, the inferred present-day crustal fields can account for the lack of solar wind ion–generated space weathering effects on Vesta.

The terrestrial planets are thought to have formed from the successive growth and accretion of protoplanetary objects <1000 km in diameter (*1*). A fraction of these protoplanets have survived to the present day and include 4 Vesta, the second most massive asteroid (525 km mean diameter). In particular, Vesta's high density, primordial basaltic crust, and large size suggest that it is an intact remnant of the early solar system that escaped catastrophic collisional dis-

ruption (*2*). Vesta therefore provides an opportunity to characterize the building blocks of the terrestrial planets and to study the processes of planetesimal accretion and differentiation.

Meteorites of the howardite-eucrite-diogenite (HED) clan probably sample the crust and upper mantle of Vesta (*3*). Geochemical studies of HED meteorites suggest that Vesta has a fully differentiated structure, with a metallic core ranging from 5 to 25% of the total planetary mass (*4*) that formed within ~1 to 4 million years (My) of the beginning of the solar system (*5, 6*). Recent volume and mass constraints from the NASA Dawn mission provide evidence of a metallic core between 107 and 113 km in radius (*2*).

Vigorous advection in a molten metallic core may generate a dynamo magnetic field. Paleomagnetic studies of meteorites suggest that past dynamos may have existed on other asteroidal objects such as the angrite and the CV carbonaceous chondrite parent bodies (*7, 8*). These data

offer the possibility of studying the physics of dynamo action in a small-body regime not represented by active dynamos in the solar system today, in which Mercury is the smallest body with a known active dynamo (*9*). However, there has been no meteorite group for which evidence of dynamo action has been confidently established and that has been directly associated with a known, intact, asteroidal parent body.

Previous paleomagnetic studies have shown that many HED meteorites are low-fidelity recorders of magnetic fields because of their large (i.e., multidomain), low-coercivity magnetic minerals (*10*). Furthermore, these paleomagnetic studies generally lacked radiometric ages and thermochronometry. As a result, they came to no firm conclusions about the origin of magnetization identified in HED meteorites (*11*). Although dynamo-generated and even nebular fields were considered, other potential sources such as recent magnetic contamination and impact-generated fields could not be ruled out (*10, 12–14*). Here, we present a paleomagnetic study of ALHA81001 (ALH, Allan Hills), a meteorite found in Antarctica in 1981 with exceptional magnetic recording properties (*15*). We also present thermochronologic and petrographic data that constrain the origin of the meteorite's natural remanent magnetization (NRM).

The main–HED-group oxygen isotopic composition of ALHA81001 suggests that it originated on Vesta (*16*). As a eucrite, ALHA81001 has a basaltic composition and probably is a sample of the asteroid's upper crust. Our petrographic observations show that ~99 volume % of ALHA81001 has a fine-grained texture. A previous paleomagnetic study found that ALHA81001 has one of the most stable NRM records observed for any main–oxygen-isotope group HED

[1]Department of Earth, Atmospheric, and Planetary Sciences, Massachusetts Institute of Technology, 77 Massachusetts Avenue, Cambridge, MA 02139, USA. [2]Department of Earth and Planetary Science, University of California, Berkeley, CA 94720, USA. [3]Berkeley Geochronology Center, 2455 Ridge Road, Berkeley, CA 94709, USA. [4]Centre Européen de Recherche et d'Enseignement des Géosciences de l'Environnement, CNRS/ Université Aix-Marseille 3, France. [5]Department of Applied Physics, Harvard University, Cambridge, MA 02138, USA.

*To whom correspondence should be addressed. E-mail: rogerfu@mit.edu

(10). This is probably due to its very fine grain size, which has led to the formation of unusually high-coercivity ferromagnetic crystals [kamacite and iron sulfide (17)]. In particular, the width of plagioclase phenocrysts in the groundmass ALHA81001 indicates that the primary crystallization of the meteorite above 1150°C took place over the course of ~1 hour (18). However, the presence of ~0.4-μm-wide augite exsolution lamellae in host pigeonite grains suggests that the meteorite was reheated to between 800° and 1100°C, possibly due to burial in a hot ejecta blanket, and then cooled slowly over several hundred years (19). Because these temperatures are above the Curie point of FeNi minerals, any remanent magnetization in ALHA81001 must have been acquired during or after this slow-cooling episode. Furthermore, we observed no undulatory extinction in plagioclase phenocrysts in the groundmass (20), indicating that the meteorite escaped impact shock pressures above 5 GPa after this slow cooling (21).

We extracted 13 subsamples (a set of 9 and a second set of 4) from two parent samples of ALHA81001. The subsamples within the first and second sets were mutually oriented to within 5°

and 10°, respectively, whereas the two parent pieces were not mutually oriented. Subsamples taken from near the fusion crust produced by atmospheric passage have systematically different NRM directions from those of seven interior subsamples, whereas two subsamples extracted from between the fusion crust and the interior subsamples have intermediate NRM directions (Fig. 1). These data are consistent with heating and remagnetization of the meteorite's <2-mm-deep exterior during atmospheric passage and suggest that the interior was not strongly contaminated by hand magnets, weathering, or viscous remagnetization since the samples' arrival on Earth.

All 13 subsamples were progressively alternating field (AF) demagnetized or thermally demagnetized to characterize their NRM components. We observed three distinct components of magnetization in each subsample (Figs. 1, 2), with the exception of one fusion-crusted subsample, which has only two components. A low-coercivity (LC) component is blocked up to a coercivity of 3 mT. Its unidirectionality across all subsamples and low coercivity are consistent with a viscous remanent magnetization (VRM) acquired since the meteorite's recovery from Antarctica in 1981. A medium-

coercivity (MC) and medium blocking temperature (MT) component, blocked from 3 to between 21 and 57 mT during AF demagnetization and up to 150°C during thermal demagnetization, is unidirectional across all subsamples (except one fusion-crusted subsample that does not have an MC component). Its low blocking temperature and unidirectionality across all subsamples strongly suggest that it is a VRM acquired during the meteorite's residence in Antarctica. The intensities of both the LC and MC/MT components are also consistent with a VRM origin according to our laboratory VRM-acquisition experiments (22).

Fusion-crusted and interior subsamples each carry distinct high-coercivity components (which we designate HCf and HC, respectively) that are blocked between 21 to 57 mT and 62 to >290 mT. The HC component is unidirectional throughout the interior subsamples (which are separated by up to 0.9 cm), and the HCf component is unidirectional across the fusion-crusted subsamples, but the HC and HCf directions are mutually divergent (Fig. 1). Thermal demagnetization identified a high-temperature (HT) magnetization in the same direction as the HC component and blocked between 150° and >275°C, above which irreversible alteration of the magnetization carriers occurs (23).

Upon AF demagnetization, the HC magnetization decays linearly to the origin with remarkable stability as compared to the NRM observed in all previously measured HED meteorites (10, 12) (Fig. 2). Its AF demagnetization spectrum is most similar to that of an anhysteretic remanent magnetization (ARM) and differs from that of a strong field (280 mT) isothermal remanent magnetization (IRM) or pressure remanent magnetization (PRM) acquired in a laboratory field of 750 μT at a pressure of up to 1.8 GPa [an analog for shock remanent magnetization (SRM) (22)]. All of these characteristics suggest that the HC/HT component is a thermoremanent magnetization (TRM) acquired during cooling in a magnetic field (24).

The $^{40}Ar/^{39}Ar$ plateau age of ALHA81001 indicates that the most recent heating event capable of full thermal remagnetization took place at 3.69 billion years ago (Ga) (Fig. 3C) and that the meteorite has largely escaped subsequent thermal disturbances. In particular, the observed degassing of radiogenic ^{40}Ar can be accounted for by a mean effective temperature between –50° and 140°C during the past 15 My (i.e., during transfer to Earth; see Fig. 3D). This is entirely consistent with our ^{38}Ar analysis, which reveals a cosmic ray exposure age of ~15 My, during which time the meteoroid may have been heated to a constant temperature of no more than 140°C (Fig. 3A). Blocking temperature relationships for kamacite and pyrrhotite (25, 26) and the degree of post–3.69 Ga heating inferred from ^{40}Ar and ^{38}Ar diffusion suggest that the HC/HT component should have survived from 3.69 Ga to the present day.

Our ARM and IRM paleointensity experiments indicate that the magnetizing field that produced the HC/HT component at 3.69 Ga most likely had
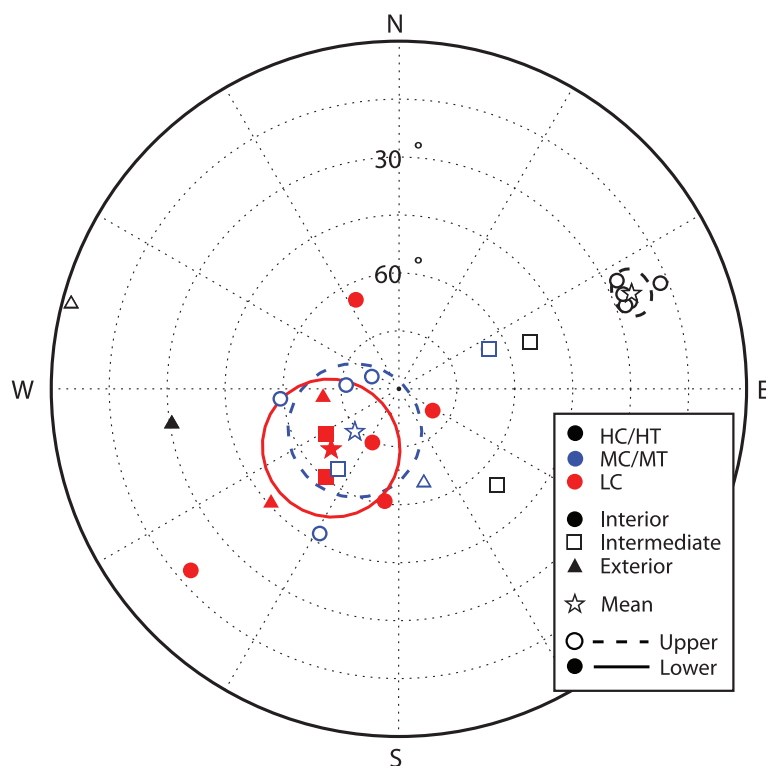

Fig. 1. NRM directions in eucrite ALHA81001. This is an equal-area stereographic projection showing the three components of magnetization observed in each subsample as inferred from principal components analyses. Black, blue, and red symbols represent HC/HT, MC/MT, and LC directions, respectively. Stars indicate average directions for each component. Dashed circles denote the 95% confidence interval for the true direction of magnetization assuming a Fisher distribution in the upper hemisphere, and solid circles denote it in the lower hemisphere. Exterior fusion-crusted subsamples, intermediate-depth subsamples (depth from surface between 0.7 and 2.0 mm), and interior subsamples (depth >2 mm) are shown by triangles, squares, and circles, respectively. Open symbols represent the upper hemisphere; solid symbols represent the lower hemisphere.

an intensity of ~12 µT (with a minimum value of ~2 µT) (27). The young $^{40}Ar/^{39}Ar$ age of ALHA81001 precludes the direct recording of a dynamo, because the longest predicted duration of a dynamo for a Vesta-sized object is on the order of several tens of millions of years to ~100 My after solar system formation (28, 29). Likewise, solar and nebular fields could not be a source of the magnetization, because they should have dissipated within the first ~6 My of solar system formation (30). Furthermore, slow cooling of ALHA81001 over $>10^2$ years rules out the recording of any putative transient, impact-generated fields, which are expected to have persisted for less than several hundred seconds under Vestan impact conditions (31). This leaves remanent magnetization of the Vestan crust and underlying materials as the most likely magnetic field source. This in turn requires that the crust was magnetized by an earlier ambient magnetic field. Given the high inferred paleointensities for ALHA81001, this earlier magnetic field was most likely due to a core dynamo. Although nebular fields may have had intensities comparable to those of core dynamos (32), they should have existed only during the first <6 My after solar system formation and typically varied in direction on time scales of several tens of orbits. Petrographic studies show that Vesta's crust cooled from the 780°C Curie point of kamacite to ambient space temperatures over at least several million years and therefore is unlikely to have coherently recorded such time-variable nebular fields (33). Another possibility is that Vesta's crust near or antipodal to large impact basins may have acquired remanent magnetization due to transient, impact-generated magnetic fields (34, 35). However, the low velocities (~5 km/s) expected for impacts on Vesta should not have typically produced the ionized plasma clouds necessary for generating strong transient magnetic fields (36–38). On the other hand, an early dynamo field should have been capable of generating steady core magnetic fields with intensities up to 2600 µT, resulting in surface fields of up to the order of 100 µT assuming a dominantly dipolar field geometry (13, 39), thereby providing a means of magnetizing the Vestan crust and underlying material.

Following (40), we calculated the expected strength of the remanent crustal field due to this earlier dynamo. Although most HED meteorites exhibit saturation remanence of between 10^{-4} and 10^{-2} A·m² kg⁻¹ (41), certain previously unmeasured metal-rich HEDs may have higher values. We measured the saturation remanence of one such HED meteorite, Camel Donga, to be 5×10^{-2} A·m² kg⁻¹ (31). Using this value for saturation remanence, a 100-µT field is expected to impart a TRM of intensity M_{TRM} up to 3×10^{-6} to 2×10^{-3} A·m² kg⁻¹ in HED material (42). The resulting magnetic fields generated by a crust magnetized to these values depend on the specific geometry of the magnetized material. We calculated the expected field for one plausible geometry. Because ALHA81001 is probably an
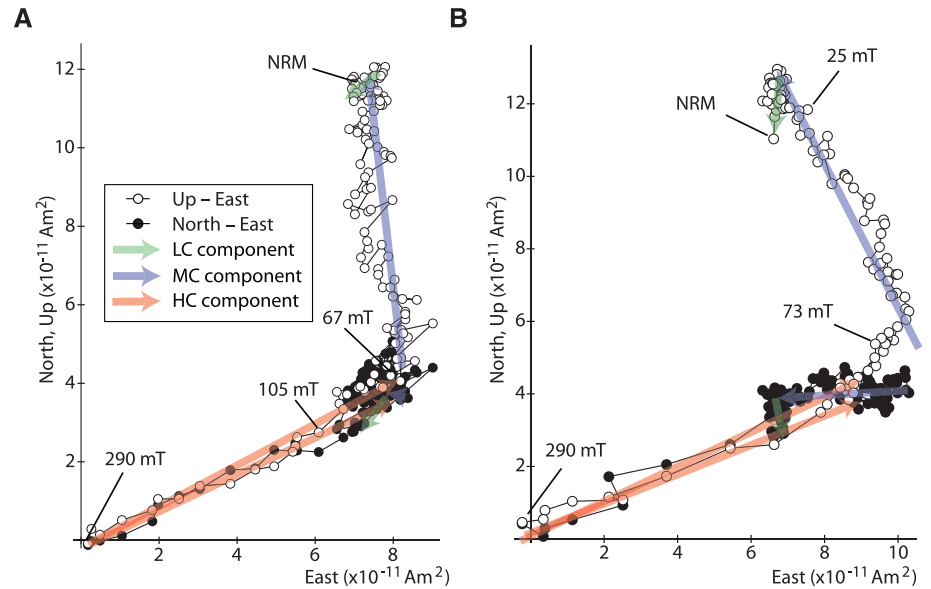

Fig. 2. Demagnetization of eucrite ALHA81001. Orthographic projections of the evolution of the NRM during AF demagnetization of two interior subsamples are shown. Open and solid circles indicate the projection of the NRM vector onto the vertical (up-east) and horizontal (north-east) planes, respectively. Red, blue, and green arrows denote HC, MC, and LC components, respectively. Selected AF levels are labeled. (**A**) AF demagnetization of interior subsample A5. (**B**) AF demagnetization of interior subsample A6. The similarity between the two demagnetization sequences indicates unidirectional magnetization.

impact melt (43), we evaluated the magnetic field within an impact-heated region in a thin crust magnetized perpendicular to the plane (31). The resulting field is $\sim 2/3\mu_0 M_{TRM}\rho$, where μ_0 is the permeability of free space and ρ is the crustal density, assumed to be 3000 kg m⁻³. Crustal material on Vesta magnetized in a dynamo with this geometry can therefore generate magnetic field intensities between 0.01 and ~4 µT.

Although the upper end of this range agrees with our inferred paleointensities, our paleointensities are nevertheless surprisingly high and may suggest the presence of more strongly magnetic material on or beneath the surface of Vesta that is not sampled by HED meteorites. Carbonaceous chondrite material has been observed in howardites and may have been observed as localized dark terrains on the surface of Vesta (44). Mesosiderites have been hypothesized to originate on Vesta because of the similarity of their oxygen isotopic compositions to those of HEDs (45). Carbonaceous chondrites and mesosiderites have saturation remanence values in excess of 10^{-1} A·m² kg⁻¹ (41) and therefore can readily produce >10-µT crustal magnetic fields when magnetized in a 100-µT dynamo field. Therefore, such material, if present on Vesta, may result in localized, highly magnetic terrains. The high paleointensity of ALHA81001, which is stronger than that of most previously studied HEDs (10), may attest to the relative rarity of the purported highly magnetic terrains. Localized regions of high crustal field intensities on Mars and the Moon are similarly too intense to be explained by the observed magnetism of known martian meteorites

and Apollo samples, respectively, and also require the existence of unsampled, highly magnetic material on these bodies (40, 46). A magnetized crust due to a prior dynamo epoch therefore appears to be the only plausible field-generation mechanism consistent with our inferred paleointensities.

Our inferred detection of an early dynamo in Vesta provides further evidence that dynamos could have formed in small differentiated bodies in the early solar system. The presence of a magnetized crust implies that at least parts of the Vestan surface had solidified and cooled below the Curie temperature during the presence of an active dynamo. The strong inferred intensity of remanent crustal magnetization suggests that the dynamo, when it was active, probably generated surface fields with intensities between 10 and 100 µT and that strongly magnetic material unsampled by HED meteorites may be present on or below the surface of Vesta. Furthermore, the existence of crustal magnetization at 3.69 Ga suggests that Vesta is likely to have crustal magnetic fields at the present time, because impact events are unlikely to have demagnetized the entire surface. Spectral features of the Vestan surface indicate that space weathering effects are more subdued than those observed on the Moon (47) and may require shielding from the solar wind ion flux at 2.36 astronomical units by a surface field ≥0.2 µT (48). The existence of >2-µT magnetic fields of the intensities estimated here are therefore sufficient to stand off solar wind ions at the orbital distance of Vesta, providing a possible explanation for the apparently limited effects of solar wind ion-generated space weathering.
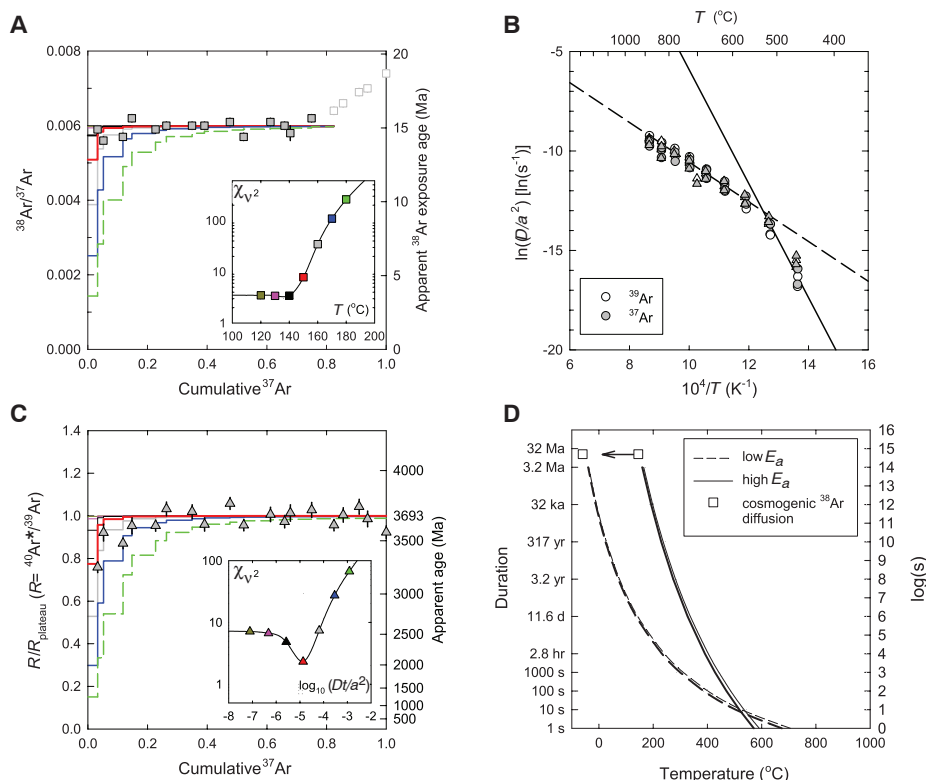
Fig. 3. ^{40}Ar and ^{38}Ar thermochronometry of ALHA81001. (**A**) Cosmogenic ^{38}Ar. Squares are observed ^{38}Ar/^{37}Ar ratios ±1 SD versus the release fraction of ^{37}Ar. Colored steps are synthetic release spectra calculated for the production and diffusion of cosmogenic ^{38}Ar over the apparent exposure duration of 15 My, assuming the Ar diffusion kinetics with maximum activation energy (E_a) in (B) (solid line) and isothermal temperatures ranging from <120° to 180°C. The inset shows reduced chi-squared (χ^2_ν) fit statistics of each model compared to solid points, identifying the best-fit temperatures to be ≤140°C. (**B**) Diffusivity as a function of temperature (T) calculated (49) from ^{37}Ar and ^{39}Ar released during the first 19 heating steps of two degassing experiments; points are diffusion coefficients (D) divided by the square of the effective domain radius (a). The solid line quantifies kinetics with the apparent E_a determined from regression to the initial four extractions of each experiment; the dashed line gives the apparent E_a determined from the subsequent 16 extractions. The difference in these values of E_a may be due to a change in a or a non-uniform spatial distribution of ^{37}Ar and ^{39}Ar (43). We take the values of E_a for the first four extractions and the subsequent extractions as upper and lower bounds on the true value. (**C**) Production and diffusion of radiogenic Ar (^{40}Ar*). Triangles are measured ^{40}Ar*/^{39}Ar ratios (R) normalized to the mean ratio of the apparent plateau ($R_{plateau}$) versus the cumulative ^{37}Ar release fractions. The colored steps are model release spectra for heating conditions, as in (A), normalized to a mean plateau age of 3.693 ± 0.071 Ga (±1 SD); the inset identifies $\log_{10}(Dt/a^2) = -5$ as the best-fit solution, where t is the duration of heating. (**D**) Duration and temperature constraints on possible thermal excursions experienced by ALHA81001. Solid curves are upper bounds on permissible thermal events at 15 million years ago (Ma) (bold curve) and at 1.0 Ga (thin curve) that would best predict the observed ^{40}Ar*/^{39}Ar spectrum shown in (C), using the maximum apparent E_a in (B); dashed curves are calculated from models using the minimum apparent E_a in (B) for thermal events at 15 Ma (bold curve) and 1.0 Ga (thin curve). The squares are upper bounds from (A) for maximum and minimum values of E_a. Solar heating since ~15 Ma to mean effective temperatures between −50° and 140°C provides an internally consistent prediction of the entire Ar data set.

References and Notes

1. J. E. Chambers, *Earth Planet. Sci. Lett.* **223**, 241 (2004).
2. C. T. Russell *et al.*, *Science* **336**, 684 (2012).
3. R. P. Binzel, S. Xu, *Science* **260**, 186 (1993).
4. K. Righter, M. J. Drake, *Meteorit. Planet. Sci.* **32**, 929 (1997).
5. The beginning of the solar system here refers to 4.567 to 4.568 Ga, which corresponds to the formation of calcium-aluminum–rich inclusions, the first macroscopic solids in the solar system.
6. T. Kleine *et al.*, *Geochim. Cosmochim. Acta* **73**, 5150 (2009).
7. B. P. Weiss *et al.*, *Science* **322**, 713 (2008).
8. L. Carporzen *et al.*, *Proc. Natl. Acad. Sci. U.S.A.* **108**, 6386 (2011).
9. D. J. Stevenson, *Space Sci. Rev.* **152**, 651 (2010).
10. S. M. Cisowski, *Earth Planet. Sci. Lett.* **107**, 173 (1991).
11. See supplementary materials section 1.
12. D. W. Collinson, S. J. Morden, *Earth Planet. Sci. Lett.* **126**, 421 (1994).
13. B. P. Weiss, J. Gattacceca, S. Stanley, P. Rochette, U. R. Christensen, *Space Sci. Rev.* **152**, 341 (2010).
14. T. Nagata, *Mem. Natl. Inst. Polar Res. Spec. Issue* **17**, 233 (1980).
15. See supplementary materials sections 2.1 to 2.3.
16. E. R. D. Scott, R. C. Greenwood, I. Franchi, I. S. Sanders, *Geochim. Cosmochim. Acta* **73**, 5835 (2009).
17. See supplementary materials section 2.3.
18. D. Walker, M. A. Powell, G. E. Lofgren, J. F. Hays, *Proc. Lunar Planet Sci. Conf. 9th*, 1369 (1978).
19. T. L. Grove, *Am. Mineral.* **67**, 251 (1982).
20. Undulatory extinction is characterized by dark bands that roll across a crystal when the sample is rotated during crossed-polar transmitted light microscopy. It is due to the realignment of crystallographic axes by heavy shock.
21. A. Bischoff, D. Stoffler, *Eur. J. Mineral.* **4**, 707 (1992).
22. See supplementary materials section 3.5.
23. See supplementary materials section 3.3.
24. A. Stephenson, D. W. Collinson, *Earth Planet. Sci. Lett.* **23**, 220 (1974).
25. I. Garrick-Bethell, B. P. Weiss, *Earth Planet. Sci. Lett.* **294**, 1 (2010).
26. D. J. Dunlop, O. Ozdemir, D. A. Clark, P. W. Schmidt, *Earth Planet. Sci. Lett.* **176**, 107 (2000).
27. See supplementary materials section 3.4.
28. L. T. Elkins-Tanton, B. P. Weiss, M. T. Zuber, *Earth Planet. Sci. Lett.* **305**, 1 (2011).
29. M. G. Sterenborg, J. L. Crowley, in *43rd Lunar and Planetary Science Conference* (Houston, TX, 2012), abstr. 2361.
30. K. E. Haisch Jr., E. A. Lada, C. J. Lada, *Astrophys. J.* **553**, L153 (2001).
31. See supplementary materials section 4.4.
32. N. J. Turner, T. Sano, *Astrophys. J.* **679**, L131 (2008).
33. M. Miyamoto, H. Takeda, abstract in *57th Meeting of the Meteoritical Society* (Prague, 1994).
34. L. L. Hood, N. A. Artemieva, *Icarus* **193**, 485 (2008).
35. D. A. Crawford, P. H. Schultz, *Int. J. Impact Eng.* **23**, 169 (1999).
36. L. L. Hood, A. Vickery, *Proc. Lunar Planet. Sci. Conf. 15th*, C211 (1984).
37. E. Pierazzo, A. M. Vickery, H. J. Melosh, *Icarus* **127**, 408 (1997).
38. E. Asphaug, *Meteorit. Planet. Sci.* **32**, 965 (1997).
39. U. R. Christensen, J. Aubert, *Geophys. J. Int.* **166**, 97 (2006).
40. M. A. Wieczorek, B. P. Weiss, S. T. Stewart, *Science* **335**, 1212 (2012).
41. P. Rochette *et al.*, *Meteorit. Planet. Sci.* **44**, 405 (2009).
42. J. Gattacceca, P. Rochette, *Earth Planet. Sci. Lett.* **227**, 377 (2004).
43. See supplementary materials section 2.2.
44. V. Reddy *et al.*, *Science* **336**, 700 (2012).
45. R. C. Greenwood, I. A. Franchi, A. Jambon, J. A. Barrat, T. H. Burbine, *Science* **313**, 1763 (2006).
46. L. L. Hood, A. Zakharian, *J. Geophys. Res.* **106**, 14601 (2001).
47. M. C. De Sanctis *et al.*, *Science* **336**, 697 (2012).
48. P. Vernazza *et al.*, *Astron. Astrophys.* **451**, L43 (2006).
49. H. Fechtig, S. Kalbitzer, in *Potassium-Argon Dating*, O. A. Schaeffer, J. Zahringer, Eds. (Springer, Heidelberg, 1966), pp. 68–106.

Supplementary Materials for

An Ancient Core Dynamo in Asteroid Vesta

Roger R. Fu,* Benjamin P. Weiss, David L. Shuster, Jérôme Gattacceca, Timothy L. Grove, Clément Suavet, Eduardo A. Lima, Luyao Li, Aaron T. Kuan

*To whom correspondence should be addressed. E-mail: rogerfu@mit.edu

This PDF file includes:

> Supplementary Text
> Figs. S1 to S19
> Tables S1 to S7
> References (*50–120*)

Other Supplementary Material for this manuscript includes the following:
(available at www.sciencemag.org/cgi/content/full/338/6104/238/DC1)

> Table S1
> Database S1

Supplementary Text

1. Introduction and Previous Work

     Previous paleomagnetic studies have been conducted on ALHA81001 and several other HED meteorites (*13*). Most relevantly, Cisowski (*10*) alternating field (AF) demagnetized two mutually oriented subsamples of ALHA81001 up to 100 mT. Unfortunately, the relatively low peak AF levels used in their study did not allow them to isolate a primary thermoremanent magnetization (TRM), as indicated by divergent magnetization directions for their mutually oriented samples and an observed lack of origin-trending magnetization [likely due to spurious anhysteretic remanent magnetization (ARM) noise from their AF system (*13*), as indicated by variability in magnetization directions during repeat AF applications with the same peak field]. As a result, they were unable to isolate the HC component that we observe to be blocked from 60 to >290 mT (Fig. 2). Instead Cisowski (*10*) inferred weak (~6 µT) paleointensities using the isothermal remanent magnetization (IRM) method for natural remanent magnetization (NRM) blocked below 50 mT (calculated using the same ratio of TRM to IRM used in this study; see Section 3.4). Because this AF range did not correspond to a single distinct NRM component as inferred from changes in magnetization direction in orthographic projection plots, Cisowski's 6 µT paleointensity (*10*) is effectively an average over a coercivity range that included up to 3 directionally distinct components, resulting in a systematically underestimated value. Indeed, paleointensities computed from his AF data above 50 mT, which should be less contaminated by low-coercivity components, are significantly higher (~10-16 µT). Furthermore, paleointensities computed from our data without separation of components differ by less than 20% from those of Cisowski (*10*) over the same coercivity ranges (see Section 3.4), suggesting that the mixing of NRM components is indeed the cause of his underestimated paleointensities. In part due to these low paleointensity values, Cisowski (*10*) considered an early Vestan dynamo to be an unlikely source of HED magnetization.

     In contrast, Morden's study (*50*) of the polymict eucrite Millbillillie found strong paleointensities ranging between 6 and 37 µT and argued for a dynamo-generated field on Vesta. However, this study analyzed a piece of Millbillillie with fusion crust, which the author apparently did not remove before performing the measurements. Morden's reported mass-specific NRM intensity values ranged from $5 - 20 \times 10^{-6}$ Am^{2}kg^{-1}, which is one to two orders of magnitude stronger than recent measurements of deep interior Millbillillie material not containing fusion crust (*51*). Furthermore, ref. (*51*) found that Millbillillie subsamples composed of a mixture of fusion crust and interior samples carried mass-specific NRM intensities consistent with the values in Morden's study. The predominantly single-component magnetizations found in Morden's study are also consistent with fusion crusted material. In contrast, non-fusion crusted subsamples in the experiments of ref. (*51*) were found to carry three distinct components of NRM. For these reasons, the samples in Morden's study were very likely contaminated with fusion crust. The relatively strong paleointensities from the Morden study therefore probably reflect at least partly a TRM acquired in the Earth's magnetic field during atmospheric passage.

Collinson and Morden (*12*) also found evidence for extraterrestrial magnetism in HED meteorites, which they tentatively suggested was the product of a dynamo-generated field. However, with the exception of the eucrite Pecora Escarpment 82502, all the meteorites samples in their study did not exhibit unidirectional magnetization or stable AF demagnetization behavior. On the other hand, Pecora Escarpment 82502, which showed the most promising magnetic properties, was recently found to have an oxygen isotopic composition anomalous with respect to most other HEDs, indicating that it is likely not from Vesta (*52*).

In the present work, we aim to resolve the ambiguities of previous studies by performing a detailed study of a single meteorite with exceptionally high magnetic recording fidelity, ALHA81001. Our magnetometer has a moment sensitivity more than a factor of 10 better compared to that of magnetometers used in most previous studies [e.g., ref. (*10*)] (see Section 3.1), which is important given the weak ferromagnetism of eucrites. We conducted AF demagnetization up to ~3 times the maximum field level used in previous studies, allowing us to identify and characterize high-coercivity components of magnetization. We also obtained the first radiometric ages for ALHA81001, which allow us to constrain when and how its NRM was acquired. Finally, we performed detailed petrographic and geochemical analyses that allow us to further constrain its thermal history and mode of magnetization.

2. Description of ALHA81001

2.1. Our samples. ALHA81001 was found in the Allan Hills of Antarctica as a part of the US Antarctic Search for Meteorites (ANSMET) Program in 1981. Its original mass was 52.9 g. The meteorite is classified as weathering stage Ae, indicating "minor" rustiness with the presence of surface evaporites (*53, 54*), although weathering stages may be underestimated for eucrites due to their low metal content.

We received two non-mutually oriented samples of ALHA81001,48 from NASA Johnson Space Center (JSC) with masses of 748.2 and 221.9 mg in April, 2011 in a nonmagnetic shielded container. With the exception of viscous remanent magnetization (VRM) acquisition experiments described below, all samples were subsequently kept in the MIT Paleomagnetism Laboratory magnetically shielded, class ~10,000 clean laboratory (DC field <150 nT) until complete the demagnetization of the NRM.

We subsampled the two parent pieces of ALHA81001 using a diamond wire saw with a 220 μm diameter diamond impregnated wire. Measurements of subsamples before and after cutting showed that the cutting process did not affect the NRM of the meteorite material by more than 5% of the magnetic moment. We obtained nine mutually oriented subsamples from the larger piece of ALHA81001 and four from the smaller piece. Subsamples from the larger piece are denoted by A1 - A6 and B1 - B3 while those from the smaller piece are denoted by C1 - C4. To subsample meteorite material near the fusion crust, we cut 4 slices of thickness 0.4-1.0 mm, each parallel to the plane of the fusion crust. The subsamples taken closest to the surface contained fusion crust overlying small amounts of unmelted interior material.

2.2. Thermal history of ALHA81001. To infer the timing of NRM acquisition in ALHA81001, we conducted $^{40}Ar/^{39}Ar$ and $^{38}Ar/^{37}Ar$ thermochronometry on three ~1 mg

whole-rock aliquots (a, b, and c) of ALHA81001 subsample ,48. The experimental methods involved neutron irradiation for 50 hours in the Oregon State University TRIGA reactor in the Cadmium-Lined In-Core Irradiation Tube (CLICIT) facility, followed by sequential degassing experiments under high vacuum and mass spectrometry under static vacuum conditions at the Noble Gas Thermochronometry Lab at Berkeley Geochronology Center [see ref. (55) for complete analytical details]. Temperatures were controlled and measured to within ± 10˚C at each extraction. Apparent ^{40}Ar/^{39}Ar ages were calculated relative to the Hb3gr fluence monitor [1081 million years (My) old] using the decay constants and standard calibration of refs. (56, 57) and isotope abundances of ref. (58) (full datasets appear in Table S1). Cosmic ray exposure ages were calculated from the ratio of cosmogenic ^{38}Ar (^{38}Ar$_{cos}$) to reactor-produced ^{37}Ar (^{37}Ar$_{Ca}$) according to refs. (55, 59, 60); exposure ages and production rates are listed in Table S2.

The ^{40}Ar/^{39}Ar age spectra and apparent Ca/K spectra of all three aliquots are in good agreement with one another (Fig. S1). Uniform Ca/K ratios observed in the initial 19 heating steps indicate that the first 80% of the gas, corresponding to extraction temperatures of <933˚C, was dominantly extracted from a single mineral with uniform composition, whereas the final 20% was derived from a different phase with much higher Ca/K ratio. We interpret this transition in Ca/K ratio as a threshold beyond which the Ar was extracted from the more retentive phase. Since we ultimately seek an upper bound on permissible thermal conditions of ALHA81001, in our subsequent analysis we focus on the least retentive portion of the sample as observed in the initial 19 steps. The mean plateau ^{40}Ar/^{39}Ar age of the three aliquots, calculated from subsets of the initial 19 steps, indicates that ALHA81001 experienced a major, probably complete Ar degassing event at 3693 ± 71 million years ago (Ma).

The higher measured ^{40}Ar/^{39}Ar ratios for the lowest temperature releases from aliquots b and c (Fig. S1) are likely due to ejection of ^{39}Ar during sample irradiation (i.e., recoil loss). This is consistent with the small, ~1 μm characteristic grain size of plagioclase, which is likely the primary ^{40}K-bearing phase in ALHA81001 (61). Recoil loss of ^{39}Ar from such small grains during the irradiation interval can result in over-estimation of the age by several percent (62).

From the fractional release of ^{39}Ar and ^{37}Ar (i.e., the nuclides produced via neutron irradiation that are most likely to be spatially uniform) observed in the first 19 steps of all three analyses, we calculated values of the apparent Ar diffusion coefficient (D) normalized to the effective radius of a spherical diffusion domain (a) at each step according to (49). When plotted against extraction temperatures, calculated values of D/a^2 for both isotopes from all three aliquots are in excellent agreement with one another in an Arrhenius plot (Fig. 3B). This agreement indicates systematic Ar diffusion in each. However, the experiments do not reveal a single linear Arrhenius relationship, but rather two approximately linear relationships separated by a break in slope at ~550˚C. Possible explanations for this pattern include a range in diffusion domain sizes (i.e., a) within each aliquot, or a slightly non-uniform spatial distribution of ^{37}Ar and ^{39}Ar due to diffusion during production in the nuclear reactor. Although we cannot *a priori* distinguish between these scenarios, we take linear regressions to data collected below and above ~550˚C to be upper and lower bounds on the activation energy, hence bounds on the effective kinetics of Ar diffusion from plagioclase (Table S3).

Under the assumption that the kinetics of Ar diffusion observed at laboratory conditions also apply to natural conditions, we test various thermal histories through geologic time that would result in the apparent spatial distribution of radiogenic ^{40}Ar (^{40}Ar*) or cosmogenic ^{38}Ar (^{38}Ar$_{cos}$), as constrained by observed ^{40}Ar*/^{39}Ar and ^{38}Ar$_{cos}$/^{37}Ar stepwise release spectra (e.g., Figs. 3A and 3C, Table S2). We describe below a number of thermal modeling strategies to constrain permissible thermal conditions of sample ALHA81001 from the observed ^{40}Ar/^{39}Ar datasets (Table S1).

Although the simplest explanation of the datasets is that ALHA81001 experienced complete degassing of ^{40}Ar at 3693 Ma, ALHA81001 may have been incompletely degassed at 3693 Ma and the elevated ^{40}Ar/^{39}Ar ratios from aliquots b and c at low temperature steps are due to retention of radiogenic ^{40}Ar produced prior to that age. Incomplete degassing at 3693 Ma may suggest a lower temperature thermal event and thereby complicate determination of the age of the NRM (Fig. S2). At high temperatures above ~1200˚C, the diffusivity of Ar in pyroxene increases dramatically. Therefore, extremely short duration, high temperature thermal excursions can theoretically lead to more complete degassing of pyroxenes compared to plagioclase and silica glass, even if the latter phases degas at lower temperatures during progressive laboratory heating (59). However, the lower Ca/K ratio measured for the initial 80% of the ^{39}Ar extracted at lowest temperature releases suggest that plagioclase, instead of pyroxene, is the dominant ^{40}K-bearing phase with the lowest retentivity. Therefore, the higher ^{40}Ar/^{39}Ar ratios for aliquots b and c are more likely due to recoil and the 3693 Ma degassing event was likely complete.

The co-existence of ~1 µm wide plagioclase grains and pigeonite-augite exsolution lamellae suggests that although ALHA81001 underwent rapid primary crystallization, it was later reheated to >800˚C and subsequently cooled slowly (Fig. S3). The later reheating event would have been sufficient to fully degas ^{40}Ar in the meteorite (Fig. S2). Because magmatism on Vesta likely lasted for no longer than ~100 My (63), the degassing of ALHA81001 at 3693 Ma must be impact-induced. An impact melt origin for ALHA81001 is also supported by our finding of a minor fraction (~1 vol. %) of relict, mosaicized pyroxene grains indicating that the precursor material for ALHA81001 underwent shock above 30 GPa (Fig. S4) [although after crystallization ALHA81001 was not shocked to >5 GPa (21) as indicated by the low shock stage (S0-S1) groundmass]. The two cooling events, rapid quenching followed by reheating and slow cooling, may have occurred during the same impact event which could have involved impact-melting followed by crystallization and then burial in a hot ejecta blanket.

Alternatively, ALHA81001 may have crystallized as an impact melt before 3693 Ma and the ^{40}Ar/^{39}Ar age represents slow cooling after a second impact-induced thermal event, either from direct shock heating or from conductive heating in a hot ejecta blanket. However, the high maximum coercivity of the HC component (>290 mT) suggests that it is a total TRM (see Section 3.2), which requires heating to above the 780˚C Curie point of kamacite. If these temperatures were directly produced by a shock, this would require pressures in excess of 30 GPa (64). The unshocked groundmass in ALHA81001 (see above) therefore excludes the direct shock heating scenario. On the other hand, burial at 3693 Ma by a hot ejecta blanket may have led to high-temperature reheating of ALHA81001 without high-pressure shock. However, assuming a flat contact surface, an ejecta blanket can only heat the underlying material to the mean temperature of the ejecta

sheet and the original surface. Assuming an original surface temperature of 180 K, thermal diffusion calculations show that the ejecta blanket must have been at a temperature of >1650˚C to heat the surface to 780˚C (*65*). Formation of a large deposit of such high temperature ejecta is unlikely given the slow impact velocities typical on Vesta (*37*). Most likely, ALHA81001 is an impact melt that was quenched, buried, and slowly cooled in a single large impact event at 3693 Ma. The several hundred years cooling timescale inferred from the width of pigeonite-augite exsolution lamellae therefore corresponds to the 3693 Ma age and to the acquisition of TRM at that time.

Subsequent thermal processing of ALHA81001 was insufficient to affect significantly the remanent magnetization of the meteorite. Using the bounds on Ar diffusion kinetics described above, we modeled the expected ^{40}Ar loss upon heating at 1000 Ma, the probable age of ejection from Vesta (*66*), and 15 Ma, the measured minimum cosmic ray exposure (CRE) time for ALHA81001 (see Fig. 3A and Table S2). The true duration of the meteorite's residence on a small meteoroid may have been longer if it was buried at sufficient depth to attenuate the effects of cosmic ray bombardment. Assuming that the ALHA81001 meteoroid was a rapidly rotating blackbody, residence for 15 My at a solar orbital distance between 1 and 2.36 AU (equilibrium temperatures between -5 and -92˚C) is sufficient to explain the full extent of ^{40}Ar loss, assuming that the true Ar diffusivity is closer to the lower end member of our derived range of permissible values. Such temperatures are too low to cause full thermal remagnetization. Therefore, the HC magnetization, whose demagnetization characteristics suggest that it is a total TRM (see Sections 3.2 and 4.3), was most likely acquired during the 3693 Ma ^{40}Ar resetting event.

*2.3. Ferromagnetic mineralogy and grain size.*We utilized low and high temperature (5-1073 K) thermomagnetic analyses, superconducting quantum interference device (SQUID) microscopy, vibrating sample magnetometer (VSM), IRM acquisition and demagnetization, and electron microprobe analyses to constrain the magnetic mineralogy of ALHA81001. Low temperature thermomagnetic data were acquired on a Quantum Design MPMS-XL system with maximum field of 7 T and minimum temperature of 5 K in the MIT Center for Materials Science and Engineering. Using the SQUID Microscope in the MIT Paleomagnetism Laboratory (*67*), we mapped the magnetic field above a 8 mm × 9 mm × 30 μm thin section of ALHA81001 that was given a saturation IRM. The magnetic field was measured at a vertical distance of 195 μm above the thin section surface and was downward continued to a height of 145 μm (*68*), resulting in an effective horizontal spatial resolution of ~150 μm. Electron microprobe analyses were performed on a JEOL-JXA-8200 Superprobe in the MIT Experimental Petrology Laboratory and a Zeiss NVision40 scanning electron microscope (SEM) in the Harvard Center for Nanoscale Systems (CNS) using secondary electron, backscattered electron, in-lens electron, election dispersive spectroscopy (EDS), and wavelength dispersive spectroscopy (WDS) detectors. The maximum spatial resolution achieved with secondary electron imaging was ~10 nm. Although the strong paramagnetic response of ALHA81001 prevented a high-fidelity measurement of its ferromagnetic hysteresis, we estimated its hysteresis parameters using a Princeton Micromag VSM at CEREGE. IRM acquisition and demagnetization experiments were

conducted with the 2G Enterprises Superconducting Rock Magnetometer (SRM) 755 in the MIT Paleomagnetism Laboratory.

Analysis of the ferromagnetic hysteresis of ALHA81001 yielded an average ratio of saturation remanence to saturation magnetization (M_{rs}/M_s) of 0.081 and an average ratio of remanent coercive force to coercive force (H_{rc}/H_c) of 2.71. Assuming shape-anisotropy-dominated grains, the calculated hysteresis parameters indicate predominantly single-domain/pseudo-single-domain behavior with a possible superparamagnetic component (*69*). Given these hysteresis properties, ALHA81001 exhibits distinctly more single-domain behavior than other HED meteorites, consistent with its uniquely very fine-grained, quenched texture.

Stepwise acquisition of a near-saturation IRM up to 2.7 T revealed two probable magnetic phases (Fig. S5). The first is fully saturated by ~0.4 T and the second is not fully saturated by 2.7 T in two of three subsamples. We performed the Lowrie test [thermal demagnetization of IRM of different strengths applied perpendicularly (*70*)] on two subsamples (Fig. S6). The sample exhibited two probable Curie points at 320-350°C and >700°C. The phase with the lower Curie temperature is carried by high-coercivity grains blocked above 2.7 T. We interpret the low coercivity, high Curie temperature phase to be an FeNi mineral and the high coercivity, low Curie temperature phase to be an iron sulfide phase, which has Curie temperature near 320°C and maximum coercivity in excess of 2 T (*71, 72*).

We conducted electron microscopy analyses in an effort to characterize further the ferromagnetic mineralogy of ALHA81001. Characteristic x-rays analyzed using EDS and WDS detectors (resolution ~1 µm) revealed that the meteorite contains 1 to 3 µm diameter grains of ilmenite and iron sulfide and 100 nm to 2 µm diameter grains of Al-bearing chromite (Figs. S3 and S7). Our quantitative WDS analyses on 11 iron sulfide grains (up to 3 µm diameter) found that all measured grains have composition within error of that of stoichiometric troilite (FeS), which is nominally antiferromagnetic. However, stoichiometric troilite may still be able to carry defect remanence and may be responsible for the observed Curie point at 320-350°C (*73*). At the same time, due to the small sizes of some iron sulfide grains, the uncertainty in composition for several analyses is up to several atomic percent in each element, allowing the possibility of remanence-carrying Fe-deficient sulfide (*74*). The ~1 µm characteristic size of FeS grains is consistent with the single-domain/pseudo-single-domain magnetic hysteresis of ALHA81001.

Our electron microprobe analysis also showed that ALHA81001 contains Al-bearing chromite, which likely has a Curie temperature equal to or less than the 90 K Curie point of stoichiometric chromite ($FeCr_2O_4$) (*75*). Ilmenite in ALHA81001 has a near-stoichiometric composition of $Fe_{1.0}Ti_{0.96}Mn_{0.04}O_3$, which is weakly ferromagnetic below its Curie temperature of ~60 K (*72*). Therefore, neither chromite or ilmenite likely contributes to the room temperature ferromagnetism of ALHA81001.

These electron microprobe results are consistent with our low temperature magnetic data. Thermal demagnetization of a saturation IRM acquired at 5 K (Fig. S8A) shows a distinct Curie point between 80 and 90 K, which likely reflects a mixture of ilmenite and chromite magnetization. The lack of transitions at ~120 K and 258 K suggest that magnetite (Fe_3O_4) and hematite (Fe_2O_3), which can form due to terrestrial weathering, are not significant contributors to the magnetization of ALHA81001 (*72, 76*).

The lack of a 35 K transition suggests the absence of stoichiometric monoclinic pyrrhotite (Fe_7S_8), although non-stoichiometric composition, small sulfide grain size and the presence of other phases often render the transition inconspicuous (*72*).

Although our low resolution (~1 µm) compositional analyses using EDS and WDS identified no phase that can account for the high Curie temperature ferromagnetic phase in ALHA81001, high resolution (<20 nm) secondary electron imaging revealed the presence of a small population of apparently high atomic number objects with diameters <20 nm in the silica-rich portions of the mesostasis found between larger pyroxene phenocrysts (Fig. S7). The size range of these bright objects is consistent with single-domain FeNi metal. Smaller single-domain and superparamagnetic [<8 nm, (*72*)] FeNi grains may also be present but would be difficult to identify due to the resolution limits of the SEM. The lack of larger, multidomain (>20 nm) high atomic number objects is consistent with the strongly single-domain and superparamagnetic state of the magnetic phase in ALHA81001 as indicated by low temperature demagnetization and viscous remanent magnetization (VRM) acquisition experiments (see below). We therefore interpret these objects as the FeNi grains responsible for carrying high temperature remanence in ALHA81001, although particulate contamination and topography on the surface of the thin section may account for some of the apparent high atomic number objects. In any case, the high Curie temperature (>700˚C) of the low coercivity phase strongly suggests the presence of FeNi in ALHA81001.

Assuming that the nanometer-scale, high-atomic-number grains are FeNi metal, they can exist in at least three different ferromagnetic phases: kamacite (α-FeNi), taenite (γ_2-FeNi), tetrataenite (γ''-FeNi), or awaruite (γ'-FeNi$_3$) (*77*). While both kamacite and taenite are capable of recording a primary TRM, tetrataenite forms due to Ni diffusion through the taenite lattice during slow annealing below 320˚C. During this process, the material develops strong magnetocrystalline anisotropy, which may lead to remagnetization of any pre-existing remanence (*78*). Although the maximum size of the inferred FeNi grains in ALHA81001 is too small to allow quantitative constraints on composition, we infer that they are most likely kamacite or taenite instead of tetrataenite for three reasons. First, the unidirectionality of NRM in ALHA81001 across 0.9 cm is inconsistent with the observed incoherence of tetrataenite magnetization at the millimeter scale (*78*). Second, heating of a subsample to 550˚C, at which temperature tetrataenite transforms to taenite, did not induce a dramatic transformation from single-domain to multidomain magnetization as is observed in tetrataenite-bearing samples (*79*). A third argument against the presence of tetrataenite and in favor of kamacite in particular is that previous paleomagnetic studies of eucrites have found kamacite to be the main room temperature ferromagnetic mineral (*10, 12, 80*), consistent with the reduced oxidation state and low nickel composition of eucrites (*81, 82*). FeNi phases with high Ni content such as taenite and tetrataenite have been found in very few unbrecciated eucrites (e.g., NWA 011, EET 92023, and EET 92004), all of which either have anomalous oxygen isotopic compositions (suggesting that they are from a different parent body than Vesta) or are suspected to be clasts from mesosiderites (*61, 83*). Awaruite has not been identified in HED meteorites. The lack of a ~620˚C Curie point in our Lowrie test (Fig. S6) provides further evidence against the presence of awaruite (*84*).

Due to the small size range for single-domain grains [~10-20 nm (*72*)] and the high metal content of most extraterrestrial rocks, most kamacite-bearing samples are

dominated by multidomain grains. In contrast, the fast cooling rate and low metal content in ALHA81001 have resulted in the apparent absence of multidomain grains and the presence of a population of superparamagnetic grains. Our thermal demagnetization of a saturation IRM acquired at 5 K found that grains blocked between 150 and 300 K carry a magnetization of 5×10^{-5} Am^{2}kg^{-1}, which is equivalent to ~17% of the saturation IRM at room temperature and indicates the presence of a significant population of superparamagnetic grains (Fig. S8B). Further evidence for the presence of superparamagnetic grains comes from the high efficiency of VRM acquisition, measured to be ~0.03% of the saturation IRM per $\log_{10}(s)$ (see Section 3.5). Such a high rate of VRM acquisition is a factor of ~5-15 greater than has been observed for multidomain kamacite-bearing lunar rocks (*55, 85*) but is similar (to within 10%) to the glassy lunar regolith breccia 14313 (*86*). Similarly, the ratio of low field susceptibility to saturation magnetization (χ_0/M_s), for which a high value indicates single-domain and superparamagnetic magnetization, is 8.6×10^{-7} T^{-1} for ALHA81001, a high value for kamacite-bearing lunar rocks but nearly identical to that of regolith breccia 14313 (*87*). This lunar sample has been shown to contain a mixture of mostly single-domain and some superparamagnetic kamacite. Furthermore, its ferromagnetic mineralogy has a similar impact melt origin as that of ALHA81001 (*88*). These affinities between the magnetic and petrographic properties of ALHA81001 and lunar regolith breccia 14313 suggest that the latter may serve as an analog to the ferromagnetic mineralogy of ALHA81001. The significant superparamagnetic component of ALHA81001 suggests the presence of fine ferromagnetic grains with low blocking temperatures that may explain the relatively large loss of moment below ~300°C.

The remanence-carrying iron sulfide phase in ALHA81001 may be stoichiometric troilite with a defect moment or iron-deficient sulfide in small grains with unconstrained composition. We argue for a preterrestrial origin of these minerals using six lines of evidence. First, troilite is ubiquitously observed in HED meteorites, while primary Fe-deficient sulfide (pyrrhotite) has also been observed in a number of unweathered HED falls (*89, 90*). Second, although terrestrial oxidation is known to affect sulfides, the principal products of the process are iron oxides and oxyhydroxides (e.g., maghemite, magnetite, and goethite) instead of ferromagnetic iron sulfides (*76, 91, 92*). We do not observe these phases in ALHA81001 (see below). Third, textures produced by this weathering process, such as oxide- and clay-filled microfractures and staining of silicates surrounding iron sulfide grains (*93, 94*), are not observed in our optical petrographic or electron microscopy analyses (Fig. S7B), even at ~20 nm resolution. Fourth, the stoichiometric or near-stoichiometric troilite compositions from our quantitative WDS measurements are inconsistent with terrestrial weathering, which produces sulfides with Fe content as low as Fe$_{0.46}$S$_{0.54}$ (*95*). Fifth, the relatively flat rare earth element (REE) abundances of ALHA81001 compared to CI chondrites, particularly the lack of Ce enrichment, suggests the lack of oxidation in the metal and sulfide phases (*96, 97*). In contrast, weathered Antarctic eucrites show overall depletion of REEs, large variations in the relative abundances of REEs, and large, usually positive Ce anomalies (*98*).

Sixth, we observed a similar remanence-bearing sulfide phase in Millbillillie, an unweathered eucrite fall. We extracted three small subsamples consisting of pure interior material from a large sample of Millbillillie provided by the Western Australia Museum. The three subsamples, called M1, M2, and M3, have masses of 382.5 mg, 227.9 mg, and

126.8 mg, respectively. Similar to our thermal demagnetization of saturation IRM experiment (Lowrie test) for ALHA81001 (Fig. S6A), we imparted a 2.5 T remanence to each sample in the east direction followed by a 1.05 T remanence in the up direction. All kamacite grains, which have maximum coercivities of ~1.05 T (*86*), should have been magnetized in the up direction, while a portion of sulfide grains, which may have higher coercivities (*71*), were magnetized in the east direction. During stepwise thermal demagnetization, the high coercivity (>1.05 T) component of magnetization shows a distinct Curie point at 320°C - 350°C, which is identical to the demagnetization behavior of ALHA81001 (Fig. S6C). Given that Millbillillie is a highly shocked eucrite containing impact melt veins with potentially similar petrography as ALHA81001 (*99*), the similarity between the magnetic mineralogy of the two eucrites may be expected.

Other weathering phases such as maghemite, magnetite, goethite, and hematite are also unlikely to be present in ALHA81001. As mentioned above, there is no SEM or optical petrographic evidence for iron oxides or corrosion textures around sulfides. Furthermore, the high maximum coercivities, even for the low coercivity phase (~0.4 T), are inconsistent with maghemite and magnetite (*70*). Furthermore, the low coercivity phase has a Curie temperature of >700°C (Fig. S6), which is higher than the inversion or Curie temperatures of maghemite and magnetite. Hematite requires a very high degree of weathering and is very rarely observed in Antarctic meteorites (*91*). Furthermore, both observed Curie temperatures of ALHA81001 are inconsistent with that of hematite. The high coercivity of goethite is consistent with that of the high coercivity phase in ALHA81001. However, a Curie temperature at 120°C is not clearly observed in our data (Fig. S6). More importantly, given that the lowest blocking temperature of the HC/HT component is above 150°C, any presence of goethite does not change our interpretation of this magnetization. Summarizing these lines of evidence, we observe no signs of terrestrial weathering in ALHA81001 and find that the magnetic mineralogy of ALHA81001 is fully consistent with that of an unweathered eucrite.

High resolution (~150 μm) SQUID microscopy maps of ALHA81001 (Fig. S9) show that magnetization due to a strong field IRM in ALHA81001 is associated with the fine-grained mesostasis material found in between larger lathes of mostly pyroxene (Fig. S10). The mesostasis consists of finely intergrown (1-10 μm width) plagioclase and silica with accessory troilite and ilmenite. Metal is thought to have been one of the last phases to have crystallized in eucrites (*100*) and therefore is also expected to be concentrated in the mesostasis of ALHA81001. Sulfide grains larger than ~1 μm in size show no statistically significant preferential distribution within areas of high magnetization, although the finer grain texture of mesostasis regions may contain higher concentrations of smaller sulfide grains. Therefore, the SQUID microscopy maps provide further evidence that one source of magnetization is the nanometer-scale grains of high atomic number material, probably kamacite, found embedded in the silica-rich portions of the mesostasis (e.g., Fig. S7). Furthermore, because chromite is only spatially associated with the pyroxene phases in ALHA81001, this distribution of magnetization also confirms that chromite in ALHA81001 is not ferromagnetic at room temperature.

3. Magnetization Measurements

  3.1. Measurement and demagnetization methodology. Most measurements of magnetization were performed on a 2G Enterprises SRM 755 in the MIT Paleomagnetism Laboratory, which has an intrinsic sensitivity of $\sim 1 \times 10^{-12}$ Am^2. In practice, because subsamples were mounted on 3 mm diameter GE 124 quartz rods or 25 mm diameter GE 124 quartz disks with cyanoacrylate or double-sided tape, the minimum distinguishable sample moment was $\leq 4 \times 10^{-12}$ Am^2. For very weak samples, extra care was taken to reduce the moments of the sample mount to $\leq 2 \times 10^{-12}$ Am^2.

  Most subsamples were demagnetized using three-axis AF demagnetization, which has several key advantages over thermal demagnetization for analyzing extraterrestrial samples (*55*). To reduce spurious ARM noise, we made repeat three-axis AF applications (up to 4 times, depending on the field level) and calculated the vector mean for each field level. Moment measurements were made after AF application along each of the three orthogonal axes and then averaged to reduce the effects of gyroremanent magnetization (GRM) following the Zijderveld-Dunlop method (*13, 101*). NRM component directions were estimated using principal component analysis (PCA) (*102*).

  3.2. AF demagnetization. All subsamples that contain fusion crust material (subsamples A1, B1, and C1) carry a distinct high coercivity component of magnetization (HCf) not present in samples from deeper inside the meteorite (Figs. 1 and S11 and Table S4). Subsamples deeper than 2.0 mm away from the surface of the meteorite (subsamples A4 - A6, B2 - B3, C3 - C4, which we refer to as "interior subsamples") exhibit a unidirectional HC component divergent in direction from the HCf component (Fig. 1). This is consistent with remagnetization of only the exterior of the meteorite during atmospheric entry. Further evidence for this is provided by the intermediate material from between 0.7 and 2.0 mm of the surface (subsamples A2 and A3), which have intermediate magnetization directions that are likely a mixture of HCf magnetization acquired during atmospheric entry and preterrestrial HC magnetization (Fig. 1). In summary, ALHA81001 passes a fusion crust baked contact test (*13*), indicating that the meteorite interior HC magnetization is preterrestrial (see Sections 4.2 and 4.3 for further discussion of the origin of the HC component).

  Interior subsamples exhibit a narrow range of NRM intensities between 9.2 and 20.7×10^{-7} Am^{2}kg^{-1}. The ratio of these NRM intensities to saturation IRM (the REM ratio) is $\sim 4 \times 10^{-3}$, which is consistent with a TRM acquired in weak fields and inconsistent with an IRM due to strong field sources such as hand magnets (*42*). This is consistent with the multicomponent IRM and ARM paleointensities (see Section 3.4)

  The LC and MC components, which we interpret to be terrestrial VRM (see Section 4.2), are present in and unidirectional across all subsamples from the larger parent sample with the exception of the fusion crusted subsample A1, which lacks a clear MC component (Fig. 1). The LC and MC components for the twelve remaining subsamples show moderate scatter with a Fisher precision parameter (*103*) $\kappa = 9.6$ and 11.3, respectively (Table S4).

  AF demagnetization removes the LC component in all subsamples by 3 mT. The MC component in interior subsamples began to demagnetize at between 16 and 21 mT and was completely removed by between 63 and 72 mT. The MC component in fusion

crust and intermediate subsamples is blocked over a narrower range of coercivities between 15 mT and 61 mT (Fig. S11, Table S4). Most subsamples experienced little to no demagnetization between 3 mT and the beginning of the MC component.

The interior HC component, which likely represents extraterrestrial magnetization (see Section 4.3 below), is found in all interior subsamples of both parent samples. This component is found to be highly unidirectional (κ=235) across five mutually oriented subsamples in the larger parent sample separated by up to 0.9 cm.

During AF demagnetization, the HC component is isolated after AF demagnetization to between 63 and 72 mT and, in the case of three subsamples, is not fully demagnetized even by 290 mT, the maximum level achievable with our AF demagnetization system. The magnetization decays to the origin, indicating that it represents a primary remanence. We quantify the degree to which the HC component trends to the origin by comparing the deviation angle (DANG) and the maximum angular deviation (MAD) (*104*). The first quantity, DANG, is the angular difference between the non-origin-constrained best-fit vector along the HC component according to PCA and the vector from the origin to the centroid of data points that make up the HC component. The second quantity, MAD, is the angular error to the PCA fit to the HC component. If DANG < MAD, then the agreement between the best-fit trend of the HC component and the closest-fit true origin-crossing trend is less than the error of the best-fit trend, qualitatively suggesting that the measured trend is truly origin-crossing. For all 5 interior subsamples from the larger parent sample, DANG < MAD (mean values are 6.9˚ and 13.4˚, respectively). The HC component of magnetization therefore appears to be true origin trending magnetization, consistent with its being the highest coercivity (i.e., characteristic) component in ALHA81001. At the same time, the remaining intensity of the HC component after demagnetization to 290 mT is ~5%, which is similar to the ~7% moment remaining for a saturation IRM demagnetized to the same level (Fig. S12). This further suggests that the HC component is a primary remanence that is blocked up to the Curie point of ALHA81001.

Because only two interior subsamples were extracted from the smaller parent sample (C3 and C4), there are insufficient statistics for a quantitatively meaningful estimate of the scatter of the directions of magnetization components in these subsamples. Furthermore, the smaller sizes of these subsamples lead to greater uncertainty both in determining their mutual orientation (within ~10˚) and in the precise measurement of their magnetization direction. Both interior subsamples show non-unidirectional low coercivity components and moderately unidirectional medium and high coercivity components (angular separations between magnetization in the two subsamples for the LC, MC, and HC components are 107˚, 37˚, and 23˚, respectively). The wide scatter of the LC component (removed below 10 mT during AF demagnetization) suggests that this component in the smaller parent sample is a weak IRM overprint. Although the two parent samples of ALHA81001 are not mutually oriented, the unidirectionality of the MC and HC components within each sample and the agreement between the mean angular separation between the two components (76˚ ± 20˚ and 61˚ ± 12˚ for the larger and smaller pieces, respectively, with uncertainties given as 95% confidence intervals) suggest that both the MC and HC components are unidirectional across the two parent samples.

3.3. Thermal demagnetization. We also performed thermal demagnetization of the NRM of an interior subsample (B2). Using a calibrated mixture of H_2 and CO_2 gas, the oxygen fugacity in the sample oven was set to 0.5 log units below the iron-wüstite buffer in an effort to reduce the alteration of kamacite in the subsample (*100, 105*). The thermally demagnetized subsample, B2, was first AF demagnetized to 15 mT in order to remove any possible IRM overprints. This completely removed the LC component. The MC component was then observed to demagnetize between 75 and 150˚C, while the HC/HT component decayed between 150 and 275˚C, at which point directional coherence of the magnetization was lost (Fig. S11A). Another interior subsample imparted with a high-field laboratory ARM (AC field of 280 mT, DC bias field of 50 µT) showed a similar rate of decay upon thermal demagnetization in the same controlled atmosphere (Fig. S13). Directional coherence was also lost at between 225˚C and 275˚C. Although the 275˚C temperature at which the NRM direction becomes unstable is well below the Curie point of kamacite, the similarity between the NRM and ARM demagnetization patterns suggests that this is a result of sample alteration or the predominance of the ferromagnetic sulfide phase over kamacite rather than the NRM being a 275˚C partial TRM. The demagnetization of saturation IRM also shows that the blocking temperature spectrum of magnetic minerals in ALHA81001 is strongly biased towards low temperatures (Figs. S6 and S14), and its similarity to the demagnetization of NRM suggests that all grain populations in ALHA81001 were magnetized. The occurrence of alteration is supported by the observation that the saturation IRM intensity of the subsample heated to 350˚C was factor of 6 greater than that of unheated subsamples (Fig. S15), suggesting that mineralogical changes have taken place. Such sample alteration has been previously commonly observed for kamacite and sulfide-bearing samples such as lunar rocks and most eucrites (*24*) and may be due to difference in the oxygen fugacity of the sample's formation environment compared to that of the laboratory oven where the sample was heated. Therefore, 275˚C represents only a lower limit on the upper bound of the HC component's true blocking temperature range.

3.4. Paleointensities. To constrain the strength of the magnetic field in which ALHA81001 was magnetized, we conducted three sets of multicomponent paleointensity experiments. We performed experiments with ARM acquisition, AF demagnetization of saturation IRM, and thermal demagnetization of saturation IRM. We did not perform Thellier-Thellier dual-heating paleointensity experiments because the sample alteration that we observed during thermal demagnetization renders the necessary partial TRM acquisition steps unreliable. We also performed one ARM demagnetization paleointensity experiment on subsample A5.

For each component of the magnetization in each subsample, the ARM acquisition paleointensity is given by (*24*):

$$B_{ARM} = f^{-1} B_{bias} \frac{\Delta NRM}{\Delta ARM}$$

where B_{ARM} is the paleointensity, B_{bias} is the bias field of the ARM, ΔARM is the ARM moment acquired in the AF range of the component of magnetization, and f is the ratio of ARM to TRM acquired in the same background field. Because ARM paleointensity estimates are most accurate when the laboratory bias field is similar to the paleofield intensity (*106*), we conducted these experiments using $B_{bias} = 50$ µT. The

value of f is on the order of unity but typically varies by up to a factor of 3-5 depending on lithology [see below and refs. (*7, 55, 101, 107*) for a more complete discussion]. In the absence of heating experiments to calibrate the value of f for ALHA81001 (which are prevented by sample alteration during heating; see Section 3.3), we assume a value of $f =1.34$ (*55*).

An ARM demagnetization paleointensity determination is similar to that of ARM acquisition except a high AF level ARM (280 mT) is acquired and then AF demagnetized, with ΔARM in the paleointensity function referring to the ARM *lost* during AF demagnetization in a given AF range. We found no systematic difference in the paleointensities inferred from ARM acquisition and ARM demagnetization experiments on subsample A5 and use only the ARM acquisition procedure on other subsamples.

Similar to ARM paleointensities experiments, the ratio between change in NRM and IRM can also be used to estimate paleofield strengths (*55*):

$$B_{IRM} = a\frac{\Delta NRM}{\Delta IRM}$$

where B_{IRM} is the paleointensity in µT, ΔNRM is the vector-subtracted change in NRM magnitude in the component's AF or thermal demagnetization interval and ΔIRM is the change in a saturation IRM when demagnetized through the same interval, and a is the ratio of IRM to low-field TRM in this interval. In the case of the HC/HT component, because the remanence is primary and origin-trending (see Section 3.2), ΔNRM and ΔIRM are taken to be the remaining NRM and IRM at the lowest AF level or temperature at which the HC/HT component is isolated [the REMc method (*108*)]. The calibration factor a may typically vary by a factor of 3-5 depending on the rock type [see below and refs. (*7, 55, 101, 109*) for a more complete discussion]. Due to the absence of direct measurements of IRM/TRM ratio for ALHA81001 (which are prevented by sample alteration during heating; see Section 3.3), for this study we adopt a value of $a= 3 \times 10^3$ (*42*).

We obtained IRM paleointensities using both thermal and AF demagnetization of the NRM and a saturation IRM. We performed thermal demagnetization of NRM on one interior subsample (B2; see Section 3.3). Due to heating alteration, we could not impart and thermally demagnetize a saturation IRM on the same subsample. Therefore, thermal demagnetization curves for a saturation IRM (7 T) were obtained from two other interior subsamples (A4 and A6). Due to the similarities in the demagnetization curves (Fig. S14B) and the similar paleointensities derived from using subsample A4 or A6 to calculate ΔIRM (Table S6), we conclude that the paleointensities derived from this method are robust.

We performed AF demagnetization of both NRM and saturation IRM on two fusion crusted (A1 and B1) and two interior subsamples (A5 and B3). However, three other interior subsamples (B2, A4, and A6) and one intermediate sample (A3) were subjected to heating before we imparted a saturation IRM. Therefore, among interior and intermediate subsamples, reliable AF demagnetization of IRM paleointensities are only available for the subsamples A5 and B3. Because we calculate the paleointensity of the HT component using remaining NRM and IRM at 150˚C, the result is unlikely to be affected by mineralogical alteration that occurs at higher temperatures.

Interior subsamples paleointensities obtained with the IRM and ARM methods agree to within the uncertainties of the methods for all three components of the NRM (Fig. S16, Tables S5 and S6). However, since only the HC component is a probable TRM (see Section 4.3), only the results for this component represent true paleofield intensities. We find that, for the interior subsamples, the ARM method yields an average paleointensity of 12 µT, the thermal demagnetization of IRM yields an average value of 11 µT, and the AF demagnetization of IRM yields 14 µT. The mean paleointensity derived from these three methods is ~12 µT. Previous calibrations of a and f on samples subjected to thermal paleointensity experiments suggest that these empirical factors may vary by a factor of several among samples with different lithologies. Lunar samples have been observed with $a = 275$ (resulting in paleointensities $10\times$ lower than our values) and at least two lunar samples have been found to have a less than 1200 (paleointensities $>3\times$ lower) (*109*). Values as high as 9 have been observed for f (paleointensities $>6\times$ lower) (*107*). Following (*55*), we adopt a factor of 5 as our uncertainty, giving ~2 µT as a lower bound on the true paleointensity of the magnetic field in which ALHA81001 was magnetized.

Fusion crusted subsamples have significantly lower apparent paleointensities relative to interior subsamples (Fig. S17, Tables S5 and S6). As in the case of interior samples, only the HCf is a probable TRM. Its weak paleointensities (< 10 µT) are anomalous compared to the majority of meteorite studies, where fusion crust magnetization is usually stronger than that of interior samples [e.g., (*8*)] and typically have paleointensities consistent with Earth's ~50 µT field. These differences may be due to incomplete remagnetization of part of the material in fusion crusted subsamples, which would lead to mixing of the widely divergent HC and HCf magnetizations and partial cancellation of magnetization. The intermediate NRM directions recorded in the intermediate subsamples (Fig. 1) suggest that such mixing of magnetization component has occurred and likely accounts for the weak paleointensities in those subsamples. The weak fusion crusted and intermediate subsample paleointensities may also be due to rotation or tumbling of the meteoroid during atmospheric entry.

Magnetic anisotropy in bulk samples can affect the results of IRM and ARM paleointensities (*110*). To assess this possibility, we measured the IRM and ARM anisotropy of ALHA81001 by magnetizing a subsample along each of the three mutually perpendicular axes with a moderate field IRM (80 mT) and ARM (AC field of 80 mT and DC bias field of 0.2 mT). The resulting degree of anisotropy, P, is defined as the ratio between the highest and lowest eigenvalues of the anisotropy tensor and reflects the extent to which remanence acquisition is dependent on the orientation of the subsample relative to the magnetizing field. Our experiments measured $P = 1.07$ for both ARM and IRM. Following ref. (*110*), this means that anisotropy corrections to the paleointensity values in Table S5 are at most 7%. This error is much smaller than the systemic uncertainties due to the calibration constants and the variation among subsamples. We therefore have not applied anisotropy corrections to our paleointensity results.

3.5. Pressure remanent magnetization (PRM) and VRM experiments. To assess the origin of each component of magnetization, we subjected several demagnetized subsamples to laboratory PRM and VRM acquisition experiments. We then compared the resulting laboratory magnetizations to the observed NRM.

Although ALHA81001 was never shocked to above 5 GPa following its primary crystallization as an impact melt, shock pressures below this limit can still produce shock remanent magnetization (SRM) (*111*). To simulate such a process, we imparted a laboratory PRM to subsample B3 following AF demagnetization of its NRM in the paleomagnetism laboratory at CEREGE in Aix-en-Provence, France. The subsample was placed in a Teflon cup immersed in polyethylsiloxane fluid to insure even distribution of pressure. A press was used to bring the subsample and fluid to the designated peak pressure and a laboratory-generated field of 750 µT was turned on. The pressure was then released over the course of ~1 minute. The subsample was then subjected to AF demagnetization until the newly imparted magnetization was removed. We repeated this process for a set of increasing pressures (0.36, 0.72, 1.08, 1.49, and 1.8 GPa). Note that although the timescale of our pressure application is longer than expected for a true impact-generated shock remanent magnetization (SRM), SRM acquisition experiments have been observed to produce similarly soft and weak (17 to 36% of a TRM in the same background field) remanence as shocks in the <5 GPa range (*111*). We therefore regard our PRM acquisition experiments as an adequate simulation of true weak-pressure (<5 GPa) SRM. We find that both the intensity and magnetic hardness of the acquired PRM increases linearly with the peak applied pressure (Fig. S18).

ALHA81001 may have acquired a VRM due to exposure to the terrestrial magnetic field during its residence in Antarctica or its storage at JSC since 1981. Although the terrestrial residence age of ALHA81001 has not been measured, those of other eucrites from the Allan Hills have been measured to be between 15 and 310 thousand years (ky) (*112*). We consider these values to be the lower and upper bounds of the terrestrial age of ALHA81001 in the subsequent analysis. There is also the possibility that the meteorite may have also acquired an extraterrestrial VRM on its parent body.

To constrain the efficiency of VRM acquisition, we placed one undemagnetized interior subsample of ALHA81001 (B2, prior to thermal demagnetization experiments) in the terrestrial field (46 µT) for a period of 13 days and 6 hours. The sample was then quickly returned to the magnetically shielded room (field <150 nT) and the decay of its VRM was monitored over the course of 6 days (Fig. S19). Using the fact that the rate of VRM decay is typically similar to that of VRM acquisition within a factor of 1-3 (*72*), we used the measured VRM decay constant to estimate the expected magnitude of VRM acquired during difference periods in the history of the meteorite. We made the approximation that the acquisition of VRM varies linearly with logarithmic time. The accuracy of such an assumption varies with rock type (*113*). We therefore also assumed a quadratic dependence of VRM on logarithmic time in order to constrain the possible error due to our assumption of linear dependence.

4. Origin of the NRM

4.1. Motivation. Our scientific interpretations rest on the inference that the HC/HT magnetization of interior samples, which remains stable to >290 mT and is blocked to >275˚C, is a TRM produced by cooling in ambient magnetic fields on the surface of Vesta. In this section, we present evidence to support this view.

4.2. Origin of the LC and MC components. As described in Section 3.2, both the LC and MC magnetizations are unidirectional across all subsamples of the larger parent sample except for the fusion crusted subsample A1, which lacks a clear MC component. Furthermore, an MC-like component is quasi-unidirectional across the smaller parent sample. This unidirectionality is consistent with a VRM origin for both components. Furthermore, the observed degree of scatter in directions is expected for a VRM since the orientation of the meteorite with respect to the local field may have varied during the course of VRM acquisition.

The LC and MC components are present in fusion crust, intermediate, and interior subsamples. The presence of the LC and MC magnetization in the fusion crusted subsamples cannot be explained by the inclusion of interior material on these subsamples. This is because the presence of mixed HC/HCf magnetization in the intermediate depth subsamples (A2 and A3) implies that the HC component in these samples has been partially overprinted (Fig. 1). Given that the MC component is completely removed during thermal demagnetization at temperatures below that at which the HC component begins to be demagnetized (Fig. S11A), the most heated portion of the intermediate samples must have had the entirety of any purported MC component removed during atmospheric entry. The fusion crusted subsamples themselves encountered even stronger atmospheric heating than the intermediate subsamples and therefore could not have retained any existing MC magnetization from before atmospheric entry. Therefore, the presence of the LC and MC components in the fusion crusted subsamples requires that these components were acquired after arrival on Earth. The LC and MC components are therefore extremely unlikely to be SRM, as atmospheric passage does not provide sufficient pressure to significantly alter the magnetization of small meteoroids (*114*). Small meteoroids such as ALHA81001 with a mass of only 52.9 g impact the ground at velocities below ~20 m s^{-1}, which is insufficient to cause remagnetization upon landing (*115*). Finally, the AF demagnetization spectrum of the MC component is inconsistent with an IRM or a PRM (Fig. S19).

The blocking temperature range of the MC component also strongly suggests a VRM origin. According to Néel theory for the relaxation of single-domain pyrrhotite and kamacite grains (*25, 26*), a VRM acquired over 15 to 310 ky in the -30°C mean annual temperature of the Allan Hills (*116*) should be removed by lab heating to between room temperature and ~145°C for a heating interval of $t_{lab} = 2400$ s, which is fully consistent with the observed removal of the MC magnetization between room temperature and 150°C (Fig. S11A).

The intensities of the LC and MC magnetizations are also consistent with terrestrial VRMs. Empirically, for grain size distributions that are not grossly non-uniform, the magnitude of VRM acquisition is approximately constant over each fixed interval of log time (*72*):

$$S = \frac{\partial M_{VRM}}{\partial (\log t)}$$

where S is the viscosity coefficient, M_{VRM} is the magnitude of a VRM (in this case the mass-specific moment), and t is time. As such, values of M_{VRM} plotted against the logarithm of time (Fig. S19) should lie roughly along a line of slope S. Although our VRM decay experiment initially exhibits non-linear behavior, the trend becomes linear

for times greater than ~1 hour after the beginning of VRM decay. Using data from this time interval, we estimate a viscosity coefficient for ALHA81001 of:

$$S = 1.0 \times 10^{-7} \frac{\text{Am}^2}{\text{kg} \log_{10} \text{s}}.$$

This constant can then be used to estimate the VRM acquired during various stages of the meteorite's history. To check the robustness of our predicted VRM intensities using the linear fit described above, we use an alternative quadratic fit to the VRM acquired as a function of logarithmic time (*55*), which corresponds to the following governing expression for VRM acquisition:

$$\frac{\partial M_{VRM}}{\partial (\log t)} = S_0 + S_1 \log t.$$

Beginning with the most recent exposure to a background field, a VRM acquired during a maximum of 30 years of storage at JSC followed by 8 months of decay in our magnetically shielded room should have a maximum specific moment of 1.7×10^{-7} Am^{2}kg^{-1} according to the linear fit and 2.8×10^{-7} Am^{2}kg^{-1} according to the quadratic fit. These values are upper limits because they assume that the meteorite was kept in the same position relative to ambient fields during the entire period of 30 years. Furthermore, the prediction of VRM acquisition is subject to significant uncertainty due to the unknown form of the VRM acquisition function for times greater than the laboratory VRM decay time (*113*). The observed LC components in interior and intermediate subsamples have a specific moments of between 0.8-1.2×10^{-7} Am^{2}kg^{-1}, which is 30 to 53% less than the maximum value estimated from the linear fit and 57 to 71% less than that of the quadratic fit. Therefore, the LC component is consistent with a VRM acquired after the meteorite's collection from Antarctica and suggests that the meteorite's position may have changed during its residence at JSC.

By the same analysis, a VRM acquired over 15 to 310 ky in Antarctica and left to remagnetize over 30 years at JSC is expected to have a specific intensity of between 2.2×10^{-7} and 3.3×10^{-7} Am^{2}kg^{-1} according to the linear fit and between 5.6×10^{-7} and 8.9×10^{-7} Am^{2}kg^{-1} from the quadratic fit. For this case, we have corrected for the lower VRM acquisition efficiency at Antarctic temperatures by assuming linear dependence of S on temperature (*72*):

$$S_{ALH} = S \frac{T_{ALH}}{T_{amb}}$$

where S_{ALH} and T_{ALH} are the viscosity coefficient and average annual temperature (243 K) for the Allan Hills where the meteorite was found, and S and T_{amb} are the measured viscosity coefficient and temperature in our lab (at 293 K). The observed intensities of the MC components of non-fusion crusted samples are between 1.80-11×10^{-7} Am^{2}kg^{-1} with a mean value of 5.3×10^{-7} Am^{2}kg^{-1}, which falls between the values predicted by the linear and quadratic fits. Given the uncertainties described above as well as the significant extrapolation in timescale used in our analysis, this is consistent with an Antarctic VRM origin for the MC component (*113*).

In summary, we find that both the LC and MC components of magnetizations represent terrestrial VRMs and as such carry no information about magnetic fields on Vesta. The HC component of interior subsamples is therefore the only magnetization with a possible extraterrestrial origin.

4.3. Origin of the HC component. Several lines of evidence suggest that the HC component of interior subsamples is extraterrestrial in origin. The systematic change from the HCf to HC component directions from the fusion crust to interior subsamples (Fig. 1) suggests that the interior HC magnetization predates atmospheric entry. Furthermore, because the MC component is very likely a VRM acquired during residence in Antarctica (see Section 4.2), any component blocked to higher temperatures and coercivities must predate the arrival of the meteorite in Antarctica. The HC magnetization of the meteorite's interior, which was not affected during atmospheric entry, is therefore extraterrestrial in origin.

The reliability of our paleointensity estimates depends on the mode of acquisition of the HC component. Accurate paleointensities are only possible if the HC component is a TRM. During AF demagnetization, the decay of the HC component is distinctly more similar to that of an ARM [an analog for TRM; see ref. (*117*)] compared to that of an IRM (Fig. S14), suggesting that this component is a TRM but cannot represent an IRM (*24*). A non-IRM origin is also strongly supported by the HC component's low NRM/IRM values of $\sim 4 \times 10^{-3}$.

Furthermore, the blocking temperature range of the HC component is consistent with a TRM acquired at 3693 Ma. Due to viscous decay at 180 K (the blackbody temperature at 2.36 AU) over the last ~3700 Ma, such a TRM is expected to be blocked between ~90°C and 780°C for single-domain kamacite and between room temperature and 320°C for iron sulfides (*25, 26*). Viscous decay also occurred during the transfer of the meteoroid to Earth, possibly at elevated temperatures. Although the CRE age of ALHA81001 is 15 My (Fig. 3A, Table S2), the orbital elements of the meteoroid during this time interval, and therefore its temperature, are unconstrained. Assuming that the meteoroid's distance from the Sun was between 2.4 and 1.0 AU during its transfer, its blackbody temperature would have been between -93 and 6°C. The corresponding minimum blocking temperature of a previously existing TRM, assuming a 15 My transfer period and a blackbody temperature of -6°C, is ~70°C for remanence carried by kamacite and pyrrhotite (*26*). The lowest blocking temperature of <150°C observed for the HC component is therefore consistent with an ancient TRM pre-dating the transfer of ALHA81001 from Vesta to the Earth.

We argue against an SRM origin for the HC component based on two lines of evidence provided by our PRM acquisition experiment (see Section 3.5). First, the observed coercivity spectrum of the HC magnetization is much harder than is expected for a PRM (Fig. S19). This is because our laboratory PRM experiments show that the maximum coercivity of remanence increases linearly with applied pressure (Fig. S17A). Extrapolating the measured maximum coercivities to the maximum possible post-formation shock pressure of ALHA81001 (5 GPa), the PRM is projected to have a maximum coercivity of only ~56 mT, which is much weaker than the observed maximum coercivity of ≥290 mT for the HC component.

Second, the intensity of the HC magnetization is likely too strong to represent an SRM. SRM intensity increases linearly with increasing background field strength (*111*). For low shocks below 1 GPa, SRM also increases linearly with peak pressure but likely ceases to increase above a certain pressure value (*111*). A linear extrapolation of our PRM acquisition experiments to 5 GPa (Fig. S18B) therefore provides an upper bound on

the possible SRM intensity in ALHA81001. We find that, in our laboratory background field of 750 µT, SRM intensity is expected to be $< 1.1 \times 10^{-5}$ Am^2 kg^{-1}.

Because the HC component has been overprinted by the MC component, we cannot directly compare this expected value to the observed intensity of the HC component and instead must estimate its original strength before the overprinting events. Since its demagnetization spectrum is similar to that of an ARM (Fig. S19), we can estimate the full, original intensity of the HC magnetization as follows:

$$M_{total} = \frac{ARM_{total}}{ARM_{HC}} M_{HC}$$

where M_{total} is the estimated original magnetization, ARM_{total} is the ARM acquired in a given bias field across the full coercivity spectrum, ARM_{HC} is the ARM acquired in the same bias field in the same coercivity range as the HC component (~70 to ~290 mT), and M_{HC} is the observed strength of the HC magnetization within the same coercivity range. The calculated M_{total} for the HC component is 2.47×10^{-6} Am^{2}kg^{-1}. Given that SRM intensity varies linearly with local field strength, a background field of >162 µT is required to explain the high intensity of the HC component if it were an SRM. Such a strong field, three times the value of the Earth's surface field, is unlikely to have existed on Vesta at 3.62 Ga.

Finally, the HC also is unlikely to be a terrestrial VRM, as the expected maximum blocking temperature for a 310 ky VRM is only 154˚C according to single domain blocking temperature theory (*25*). Such a blocking temperature is too low to be consistent with the HC component. Similarly, the HC cannot be an extraterrestrial VRM, as even a 4 Gy VRM at the cryogenic temperatures of the asteroid belt (blackbody temperature of 180 K at 2.4 AU) should be blocked up to a similar temperature as the MC component assuming single-domain kamacite and pyrrhotite to be the magnetic carrier.

We have shown above that the HC component is unlikely to be an IRM, SRM, or VRM and that it is probably a TRM acquired upon cooling in a stable background field over a period of several thousand years (see main text). We now address the possible sources of this background field.

4.4. Origin of extraterrestrial fields. Although ALHA81001 crystallized rapidly over a ~1 hour period, the presence of pigeonite-augite exsolution shows that cooling between 1100˚C and ambient blackbody temperatures likely took place over several hundred years. This cooling event likely represents the acquisition of the HC magnetization (see Section 2.2). We now show that impact-generated fields on Vesta are not expected to be stable at such timescales.

We consider two scenarios of field generation by impacts. In the first scenario, ionized vapor from the impact undergoes charge separation, leading to an electric current and its associated magnetic field (*118*). This phenomenon has been studied in the laboratory for impactor velocities up to ~5 km/s (*35,118*). According to calibrated scaling laws (*35*), the duration τ in seconds of such a field is approximated by:

$$\tau = 20 \frac{x}{v_{imp}}$$

where x is the distance from the impact point and v_{imp} is the impact velocity, which is approximately 5.4 km/s for large impacts on Vesta (*38*). Taking *x* to be the radius of

Vesta (~260 km), the maximum duration of such fields on Vesta is only ~1000 sec. In the second scenario, a plasma cloud created in an impact may expand along the surface of Vesta, concentrating ambient magnetic field near the antipode of the impact. Such a process has been proposed as an explanation for lunar surface magnetic anomalies (*34, 36*). However, the generation of sufficient ionized vapor to efficiently perturb ambient fields is unlikely given the low velocity of a Vesta large crater-forming impact (*36, 37*). Although vaporization is expected for impact velocities of the lunar basin-forming events (>10 km/s), slower impact velocities below ~7.5 km/s should produce no vapor (*36, 37*). Therefore, neither mechanism generates magnetic fields of long duration necessary to explain the HC component, which was likely acquired over several thousand years.

A remanent crustal field is the only plausible source of magnetic fields stable over the necessary timescales at 3693 Ma on Vesta. As discussed in the main text, for the strength of a crustal field to be consistent with our inferred paleointensities, the crust must have been magnetized in an earlier steady magnetic field and the crustal material must itself be sufficiently magnetic. The TRM acquired by a material with saturation remanent magnetization M_{rs} during cooling in a weak magnetic field of strength B_0 is approximately:

$$M_{TRM} = aB_0M_{rs}$$

where M_{TRM} is the resulting magnetization of the material and a is an empirical constant approximately equal to 3×10^{-3} μT^{-1} for B_0 in µT and M_{TRM} and M_{rs} in the same units (*42*). Although previously measured HED meteorites have values of M_{rs} less than 10^{-2} Am^2kg^{-1}, a number of yet unmeasured metal-rich HED meteorites, including Petersburg, Camel Donga, Pomozdino, Bununu, and Bolghati (*41,119*), may have higher values of M_{rs}.

To constrain the M_{rs} of such metal-rich HED meteorites, we acquired three small (1-2.5 g) stones of Camel Donga from two different private meteorite dealers. All fusion crust material was removed with a diamond wire saw (see Section 2.1). We measured at least one large fragment from each stone consisting of pure interior material (Table S7). The weighted mean value of M_{rs} is 5.07×10^{-2} Am^2kg^{-1}. Crustal material with this value of M_{rs} is expected to be magnetized to $M_{TRM} \approx 2 \times 10^{-3}$ Am^2kg^{-1} in a 100 µT field [see main text and (*42*)].

Given a value for the magnetization intensity of the crust, the actual magnetic field intensities generated depend strongly on the geometry of the magnetized region. Strictly speaking, the magnetic field due to material with uniform magnetization intensity may vary from 0 [e.g., inside a long cylinder magnetized parallel to its axis (*72*)] to arbitrarily high values [above an arbitrarily thick body magnetized to maximize the surface field at one point (*120*)]. We therefore calculated the magnetic field expected for one plausible geometry. We assumed that a magnetized portion of the Vestan crust can be modeled by a thin disk with small thickness compared to its horizontal extent and that it is magnetized perpendicular to the surface. Because ALHA81001 is an impact melt, we assumed that it formed inside an impact basin. Impact heating that caused melting of ALHA81001 would have demagnetized the surrounding regions. Therefore, following (*37*), we modeled the impact heated material as a fully demagnetized spherical region inside the crust. This fully demagnetized region can be represented by the superposition of the uniformly magnetized disk and a spherical region magnetized to the same intensity

in the opposing direction. The magnetic field inside this region is therefore the sum of the internal field of the uninterrupted thin disk (0) and that of the sphere ($2/3\mu_0 M_{TRM}\rho$), resulting in $2/3\mu_0 M_{TRM}\rho$ (*72*), where ρ is the density of the crust. A more prolate (height is greater than width) or oblate demagnetized region would result in stronger or weaker fields, respectively, with a maximum field of $\mu_0 M_{TRM}\rho$.

The above geometry (spherical demagnetized region) and value for M_{TRM} result in remanent crustal fields of ~4 µT given a 0.1 mT magnetizing dynamo surface field. Therefore, the expected strength of remanent crustal fields due to an earlier dynamo on Vesta is consistent with our minimum inferred paleointensity of 2 µT.
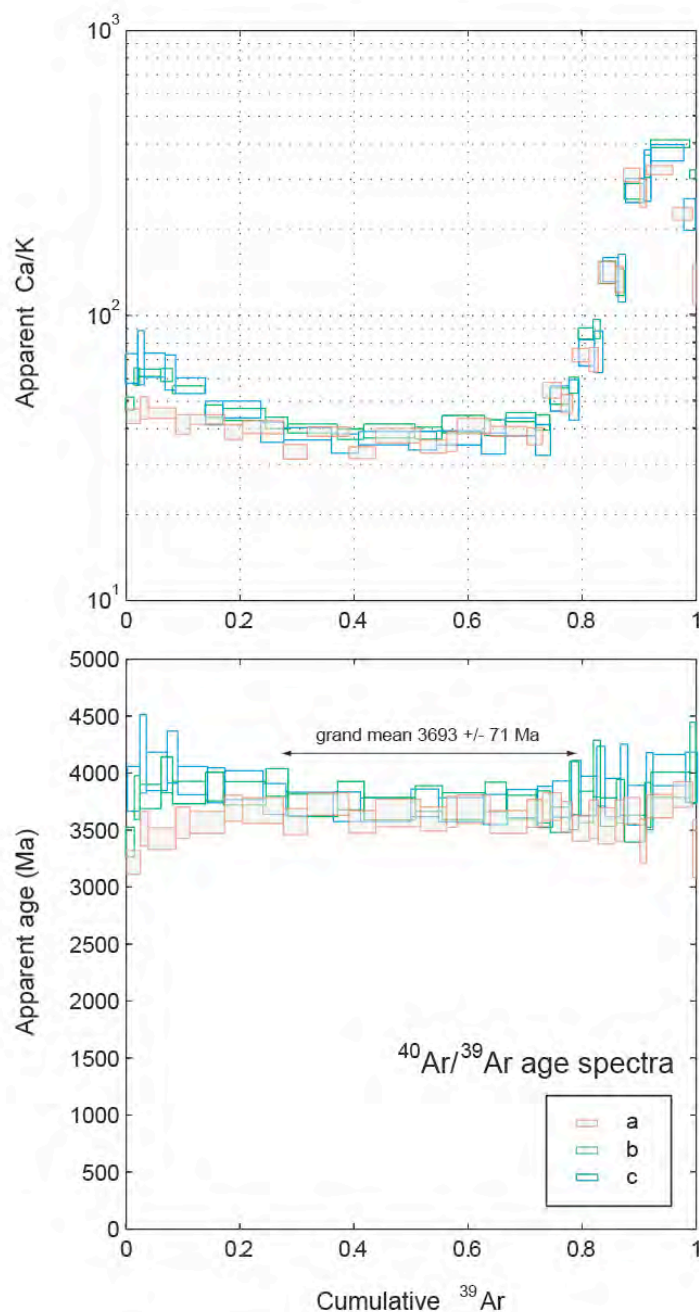
Fig. S1.

[40]Ar/[39]Ar chronometry of ALHA81001. Apparent Ca/K (**A**) and [40]Ar/[39]Ar age (**B**) spectra for three aliquots (a, b and c) of whole-rock sample ALHA81001. Each spectrum is plotted against the cumulative release fraction of [39]Ar. Dimensions of boxes indicate ± 2 SD (vertical) and the fraction of [39]Ar released (horizontal). Ca/K ratios were calculated from the $^{37}Ar_{Ca}/^{39}Ar_K$ ratio assuming the relative production ratio for Ca to K is 1:1.96. A mean plateau age of 3693 ± 71 Ma (1 SD) is shown, calculated from sub-selected steps for each analysis between 622˚C and 931˚C as indicated by the arrow.
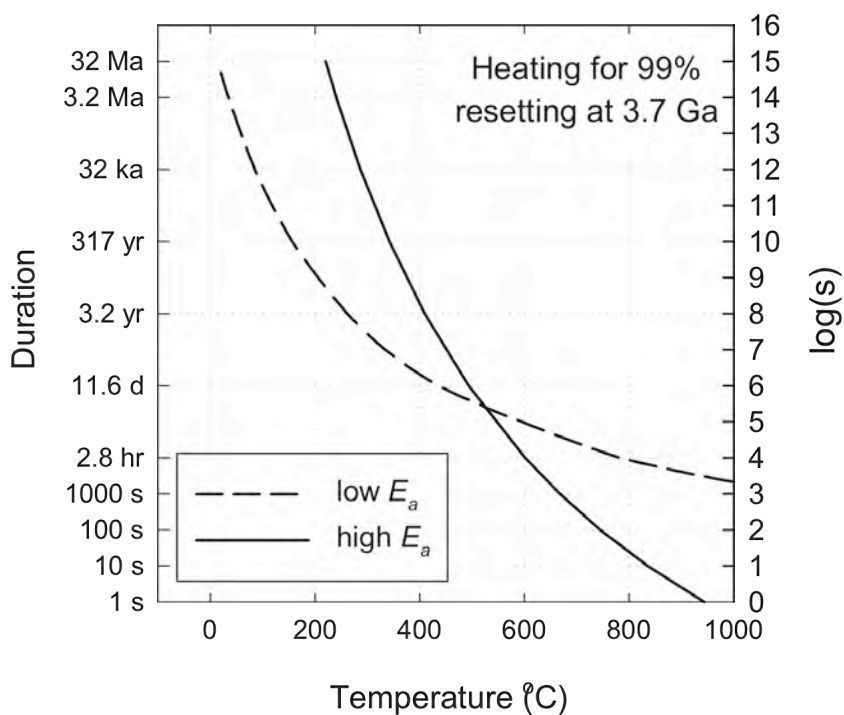
Fig. S2

Thermal constraints on ALHA81001 at ~3700 Ma. Assuming that the "high E_a" and "low E_a" models shown in Fig. 3B provide bounds on the kinetics of [40]Ar diffusion in ALHA81001 at 3.7 Ga, the solid and dashed curves, respectively, are the reheating conditions that would be required to diffuse 99% of the radiogenic [40]Ar accumulated between 4500 Ma and 3700 Ma.
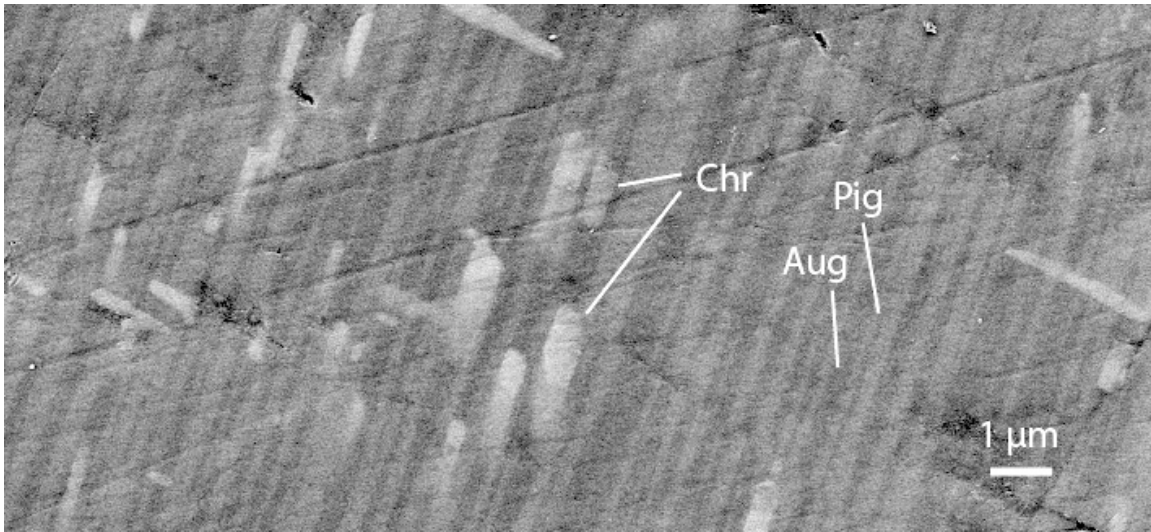
Fig. S3

Electron microscopy image showing augite-pigeonite (Aug-Pig) exsolution lamellae and associated chromite (Chr) grains in interior subsample A4. Image obtained with in-lens detector, which responds to both backscattered and secondary electrons, on a Zeiss NVision40 SEM.
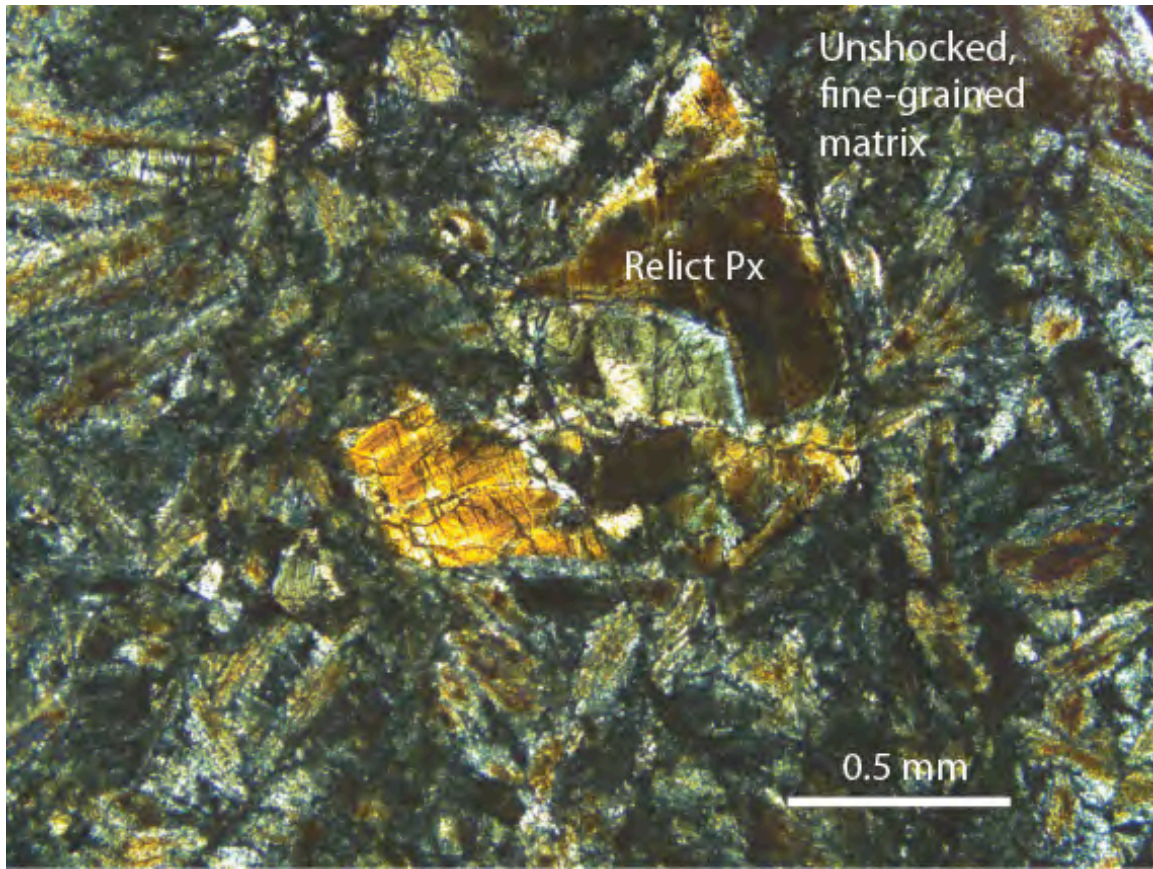
Fig. S4

Crossed polar transmitted light optical image of ALHA81001. Shown is a large, mosaicized relict pyroxene clast that has experienced shock to >30 GPa surrounded by unshocked matrix. Such relict pyroxene clasts make up ~1% of ALHA81001 by volume.
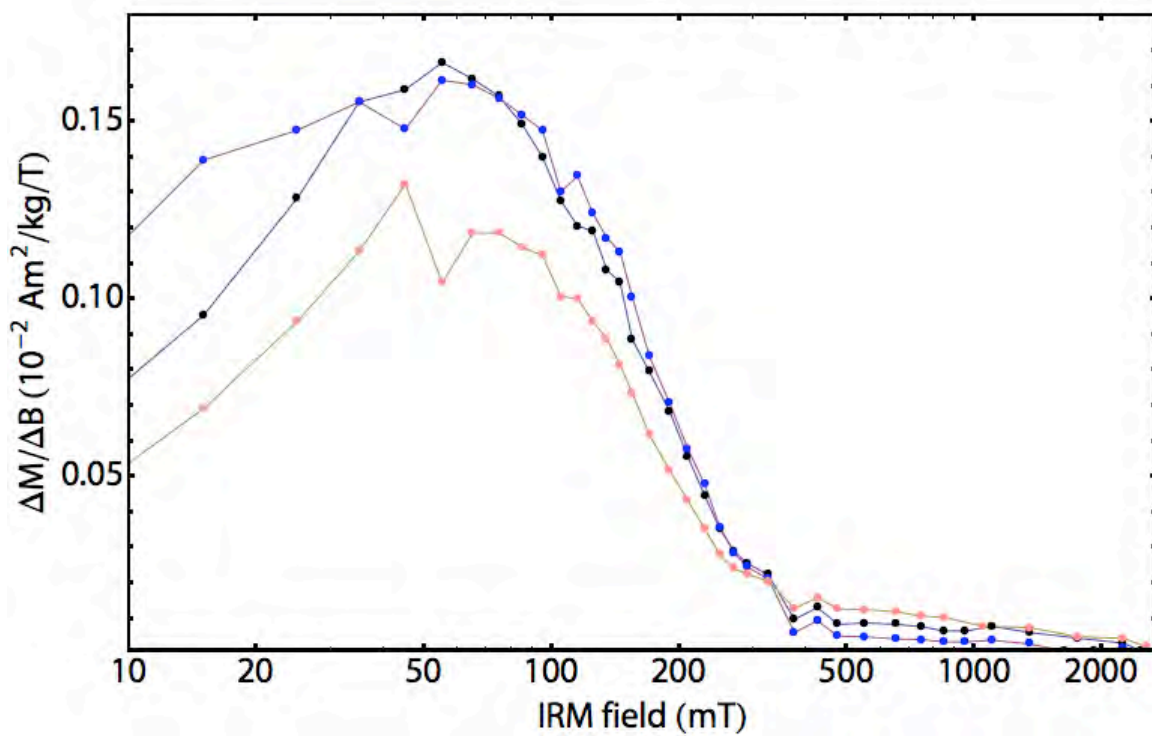
Fig. S5

Derivative of remanence gained during acquisition of a near-saturation IRM. Experiment performed on three interior subsamples A4 (black), A6 (pink), and C4 (blue) in fields up to 2.7 T. Note the high degree of homogeneity among the subsamples.
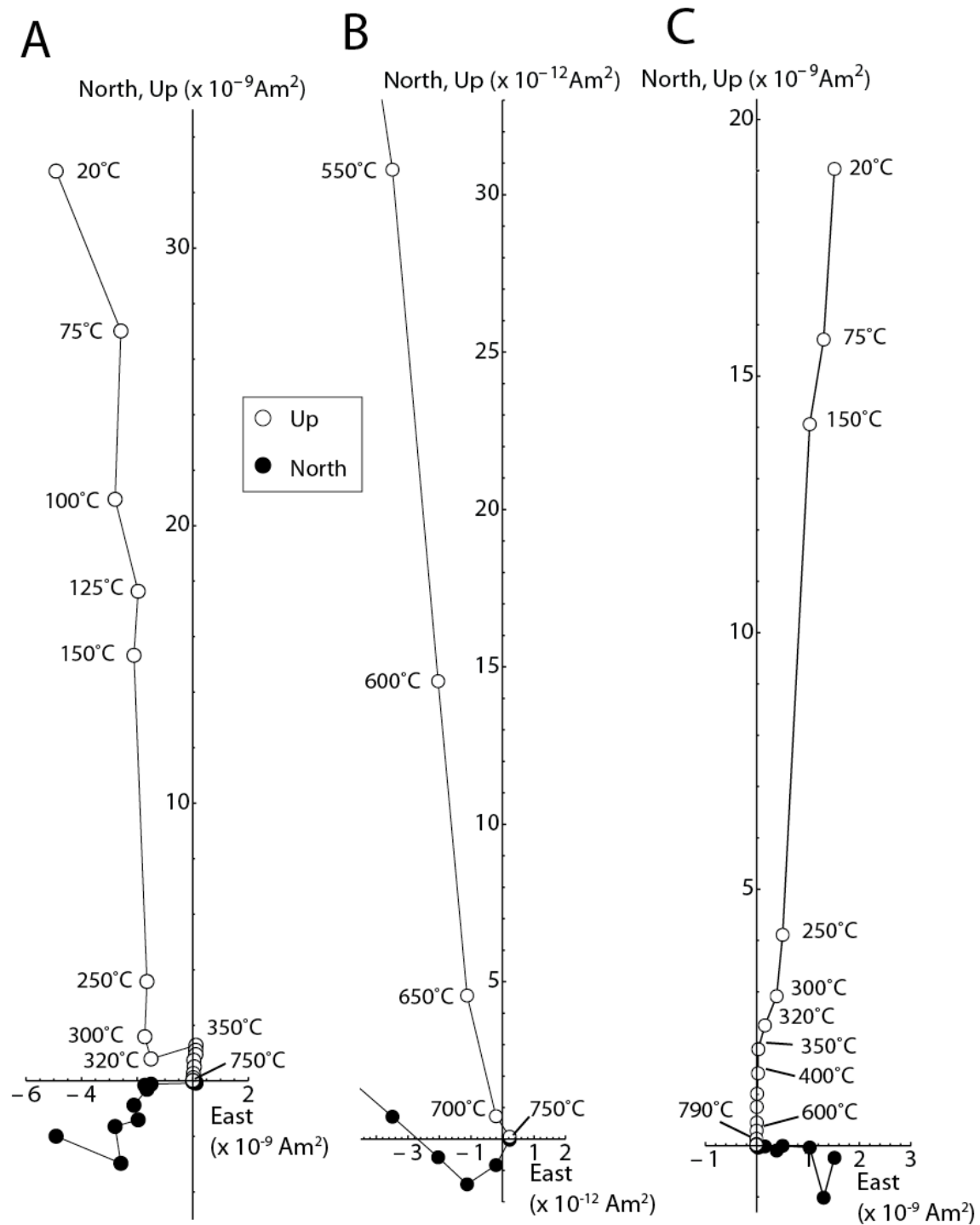
Fig. S6

Thermal demagnetization of saturation IRM. (**A**) Orthographic projection for thermal demagnetization sequence of a 7 T saturation IRM acquired in the west direction followed by a 2.7 T IRM acquired in the up direction for interior subsample A6. Note the removal of westward (2.7 - 7 T) magnetization between 320 and 350˚C. (**B**) Close up orthographic projection of the final steps in the thermal demagnetization of a 2.7 T IRM

acquired in the up direction for interior subsample A4. (**C**) Orthographic projection for thermal demagnetization of a 2.5 T saturation IRM acquired in the east direction followed by a 1.05 T IRM acquired in the up direction for subsample M3 from the Millbillillie eucrite. As in (A), note decay of high-coercivity magnetization between 320˚C and 350˚C.
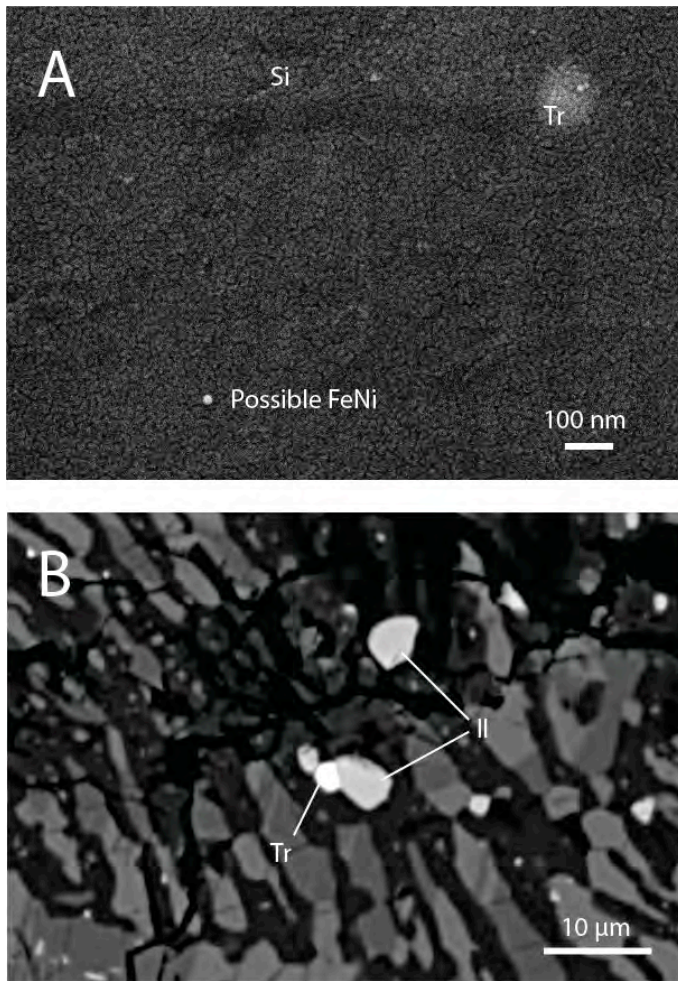
Fig. S7

High-resolution electron microscopy image of probable ferromagnetic phases. **(A)** Troilite (Tr) and possible FeNi metal particles embedded in a silica-rich phase (Si) in interior subsample A4. Image obtained with in-lens detector on a Zeiss NVision40 SEM. **(B)** Troilite (Tr) and ilmenite (Il) in thin section ALHA81001,48 showing a lack of weathering textures. Backscattered electron microscopy image acquired with JEOL-JXA-8200 microprobe.
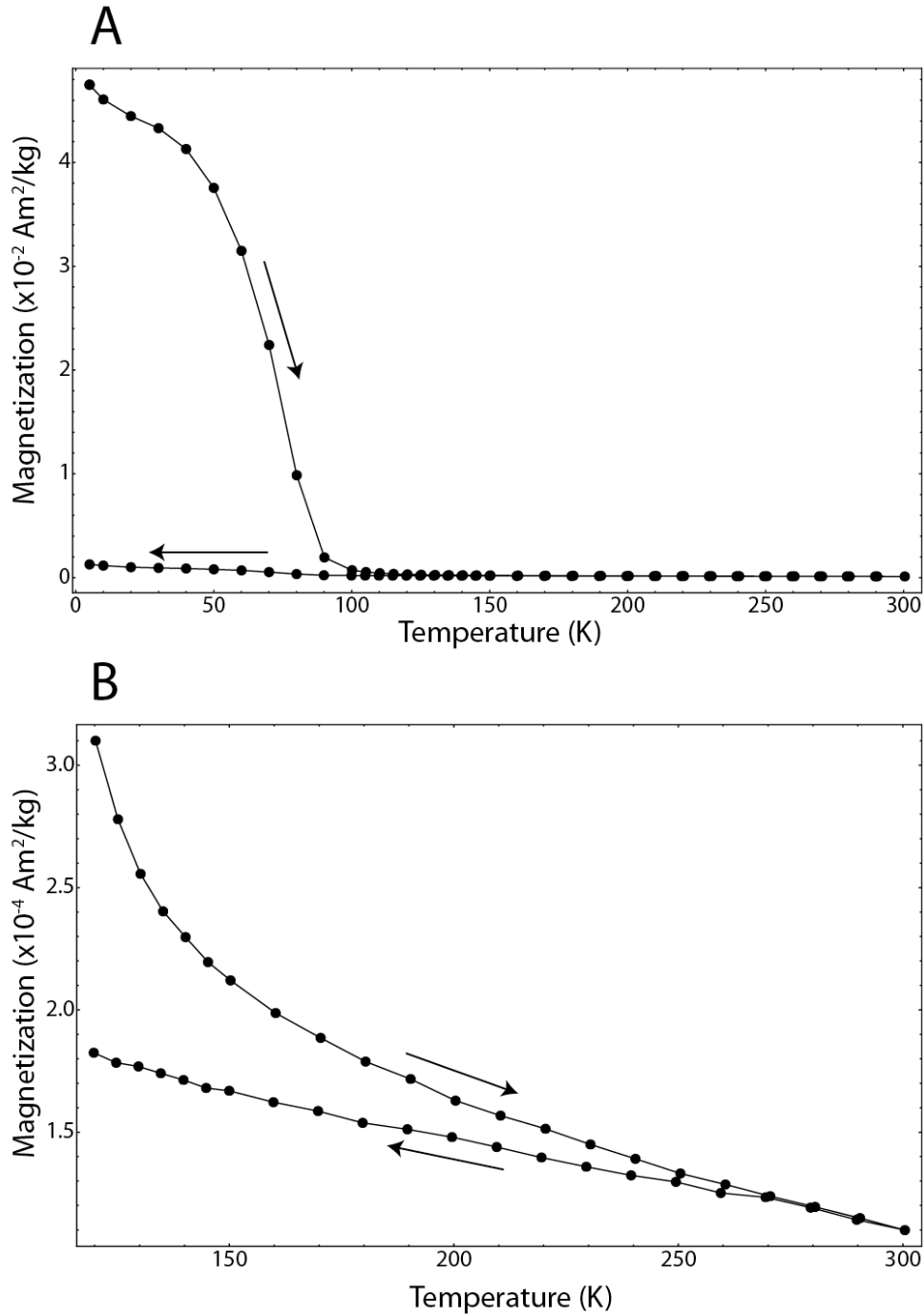
Fig. S8

Low temperature thermal demagnetization of interior subsample A6. Thermal cycling (from 5 K to 300 K and back to 5 K) of a 5 K saturation IRM (7 T field). The background field during cycling was <0.2 mT. (**A**) All data from 5 to 300 K. A Curie point at ~90 K is clearly observed. (**B**) Data above 120 K to emphasize superparamagnetic grains.
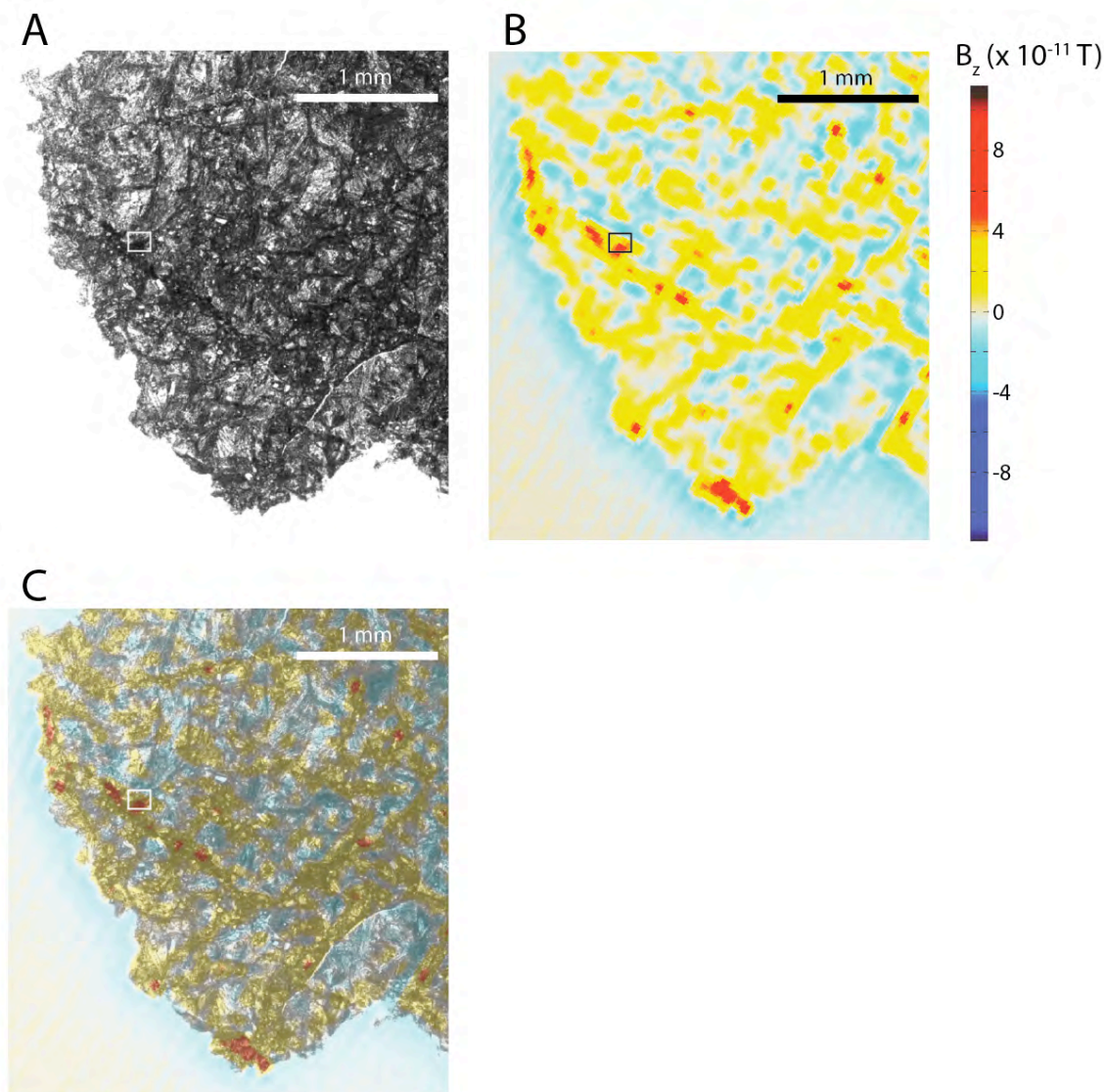
Fig. S9

SQUID microscope study of 30 µm thin section ALHA81001,39. (**A**) Crossed polars transmitted light photograph. (**B**) SQUID microscope map of the magnitude of the vertical magnetic field (a proxy for magnetization) measured from a height of 195 µm and downward continued to 145 µm above a 30 µm thick thin section. The sample was given a strong field IRM (280 mT) in the positive direction, resulting in the predominance of positive (red) magnetic fields above regions of high local magnetization. (**C**) Overlay of crossed polars transmitted light image (A) and SQUID microscope map (B). Areas of high magnetization overlap strongly with dark, mesostasis assemblages of plagioclase and silica along with accessory ilmenite and troilite. The brighter, coarse-grain regions, which are dominated by pyroxene lathes, exhibit much weaker magnetization. Region inside small box is shown at high magnification in Fig. S10.
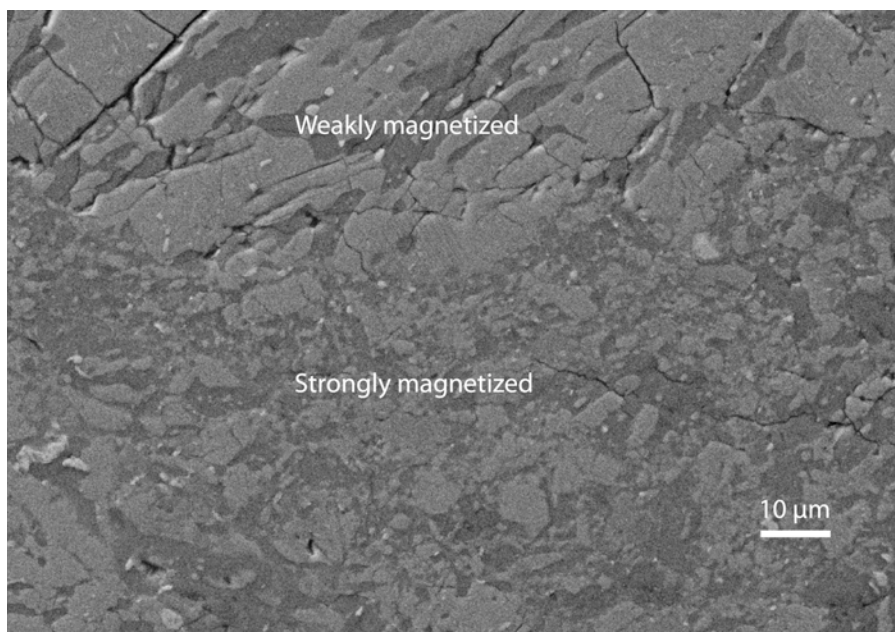
Fig. S10

Electron microscopy image of regions of high magnetization as observed by the SQUID microscope as indicated by boxes in Fig. S9. Fine-grained regions labeled "Strongly magnetized" are only found in regions of high magnetization in the SQUID microscopy maps. Image obtained with in-lens detector on a Zeiss NVision40 SEM.
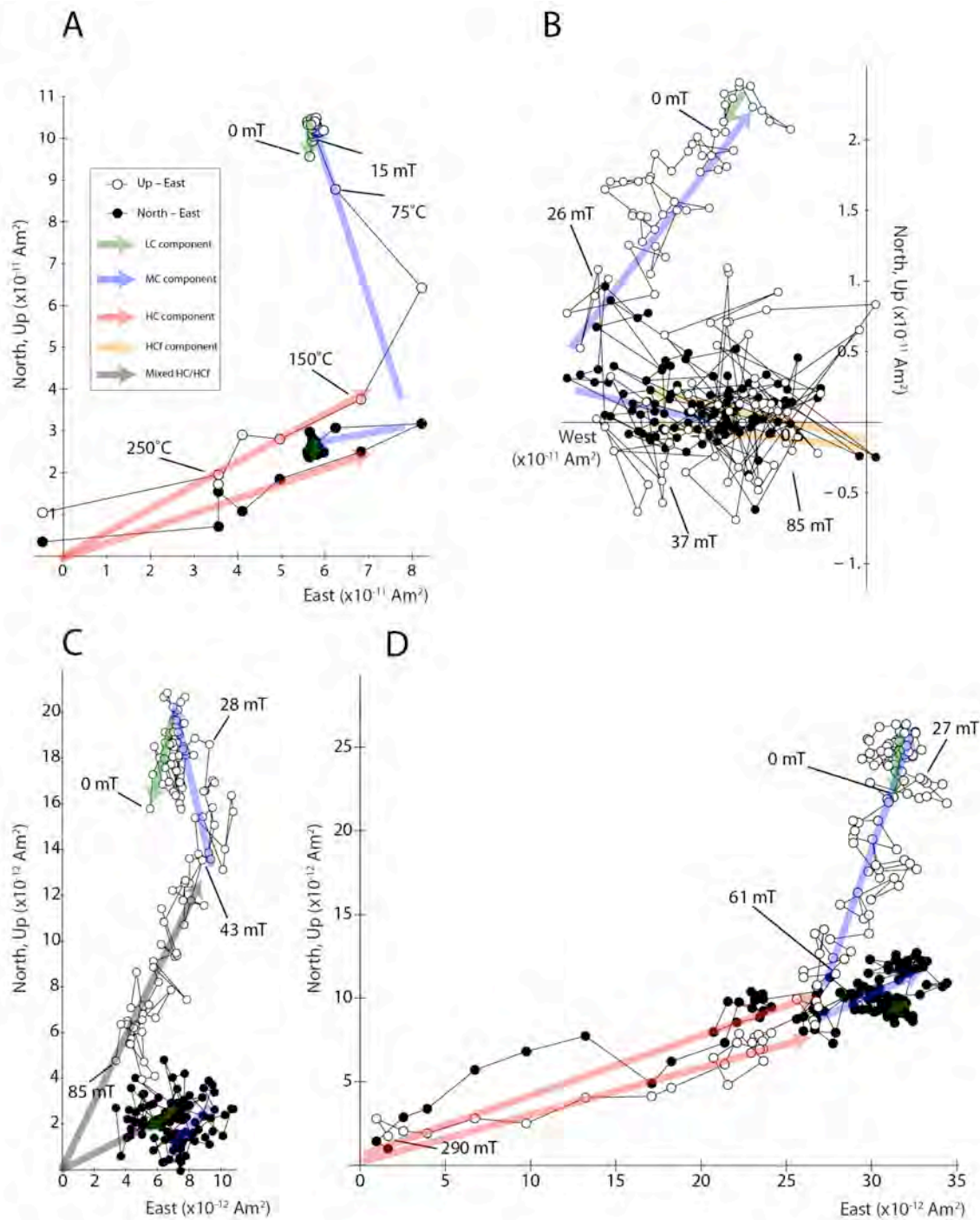
Fig. S11

NRM demagnetization of subsamples of ALHA81001. Orthographic projections showing the evolution of the NRM during AF demagnetization of NRM for one interior and one fusion crusted subsample. Open and closed circles indicate the projection of the magnetization vector onto the vertical (up-east) and horizontal (north-east) planes,

respectively. (**A**) AF followed by thermal demagnetization of interior subsample B2. (**B**) AF demagnetization of fusion crusted subsample B1. Magnetic mineralogy of the fusion crust is characterized by greater noise during AF demagnetization. (**C**) AF demagnetization of intermediate subsample A3 (1.6 mm from fusion crusted surface). (**D**) AF demagnetization of interior subsample A4. Similarly oriented LC and MC components are present in both subsamples (green and blue arrows, respectively. The two subsamples have divergent HC and HCf components (red and orange arrows, respectively). The intermediate sample (C) has a high-coercivity component that is a mixture of the HC and HCf components and is intermediate in direction (gray arrows).
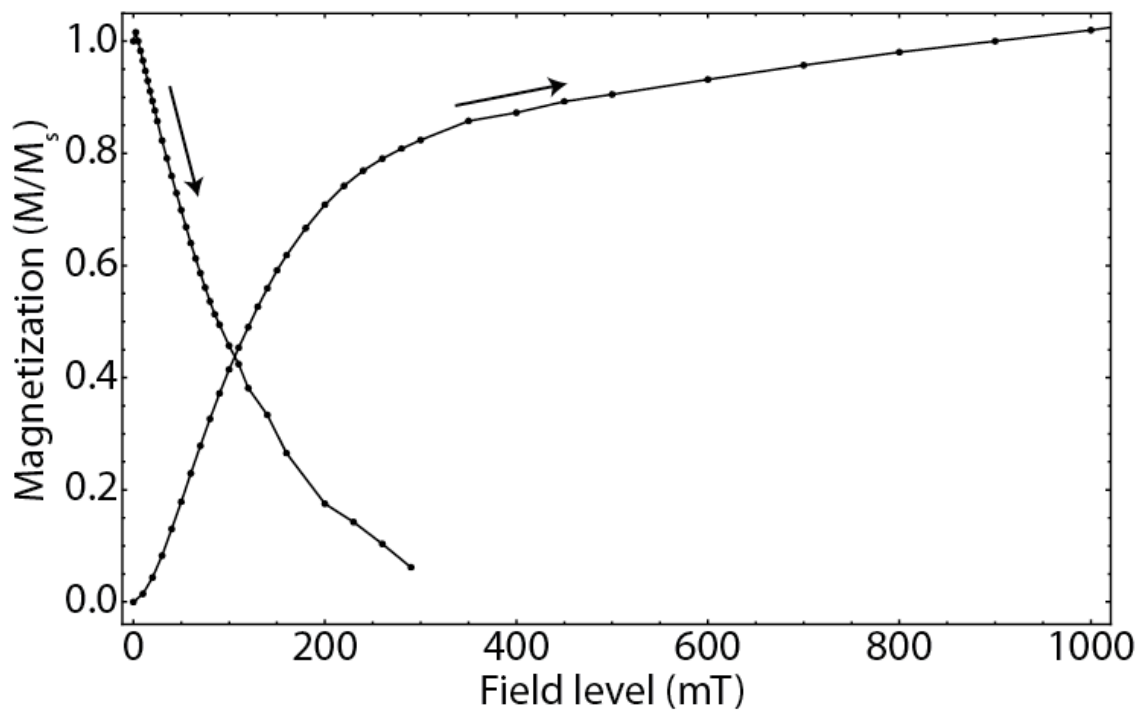
Fig. S12

Acquisition and demagnetization of IRM on interior subsample A4. Moment is
normalized to the saturation remanence (M_s). AF demagnetization was performed on 3
axes to simulate the procedure used for the AF demagnetization of NRM. The
demagnetization curve terminates at 290 mT, the maximum level of our AF
demagnetization system.
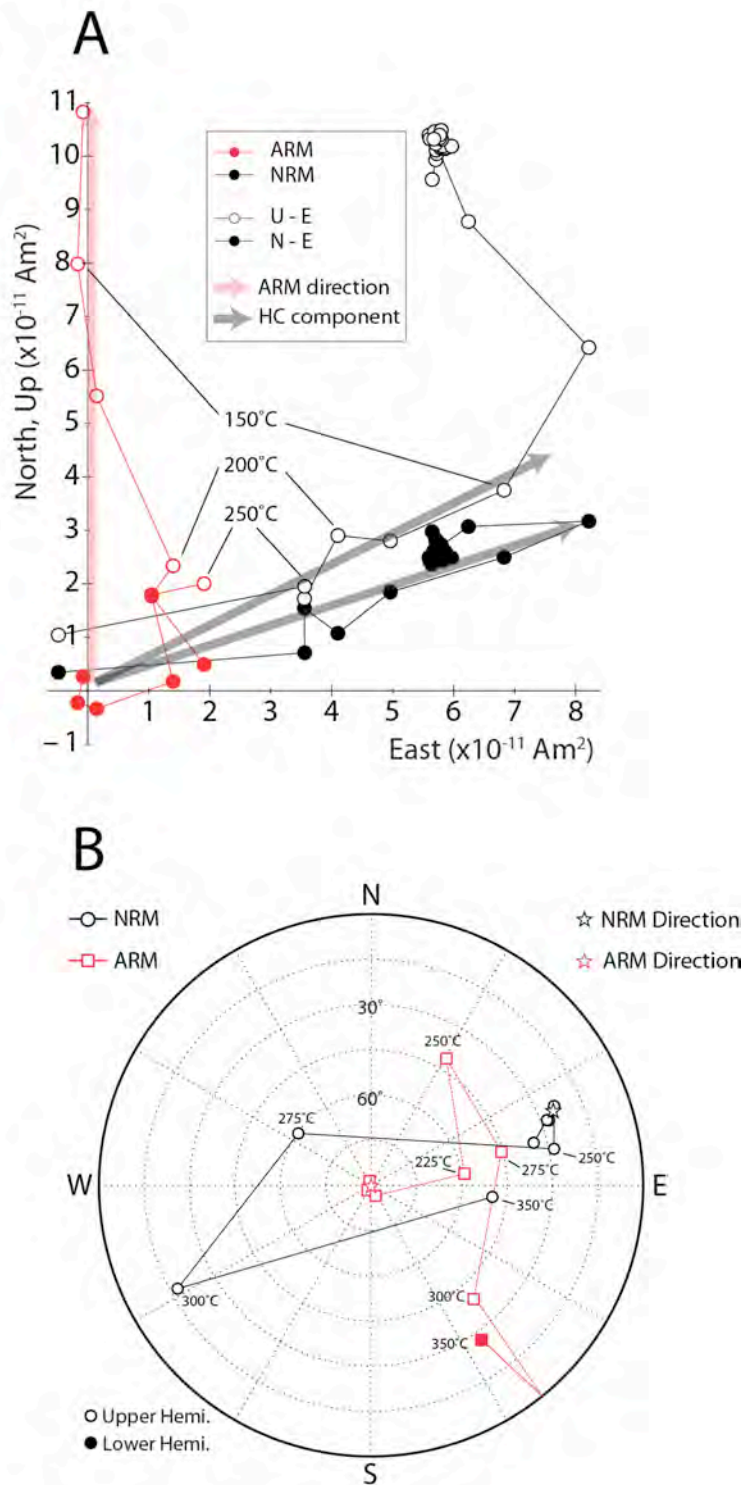
Fig. S13

Controlled-atmosphere thermal demagnetization of interior NRM (gray) and a laboratory ARM (red) for subsamples B2 and A3, respectively. (**A**) Orthographic projections

showing the evolution of the NRM during AF demagnetization of NRM for two interior subsamples. Open and closed circles indicate the projection of the magnetization vector onto the vertical (up-east) and horizontal (north-east) planes, respectively. (**B**) Equal area stereographic projection showing the three components of magnetization observed in each subsample as inferred from PCA. The similar rates of demagnetization and the loss of directional coherence for both subsamples between 225˚C and 275˚C suggest that alteration is occurring and that the erratic behavior of the NRM above these temperatures does not reflect true recording of a background field when the NRM was acquired.
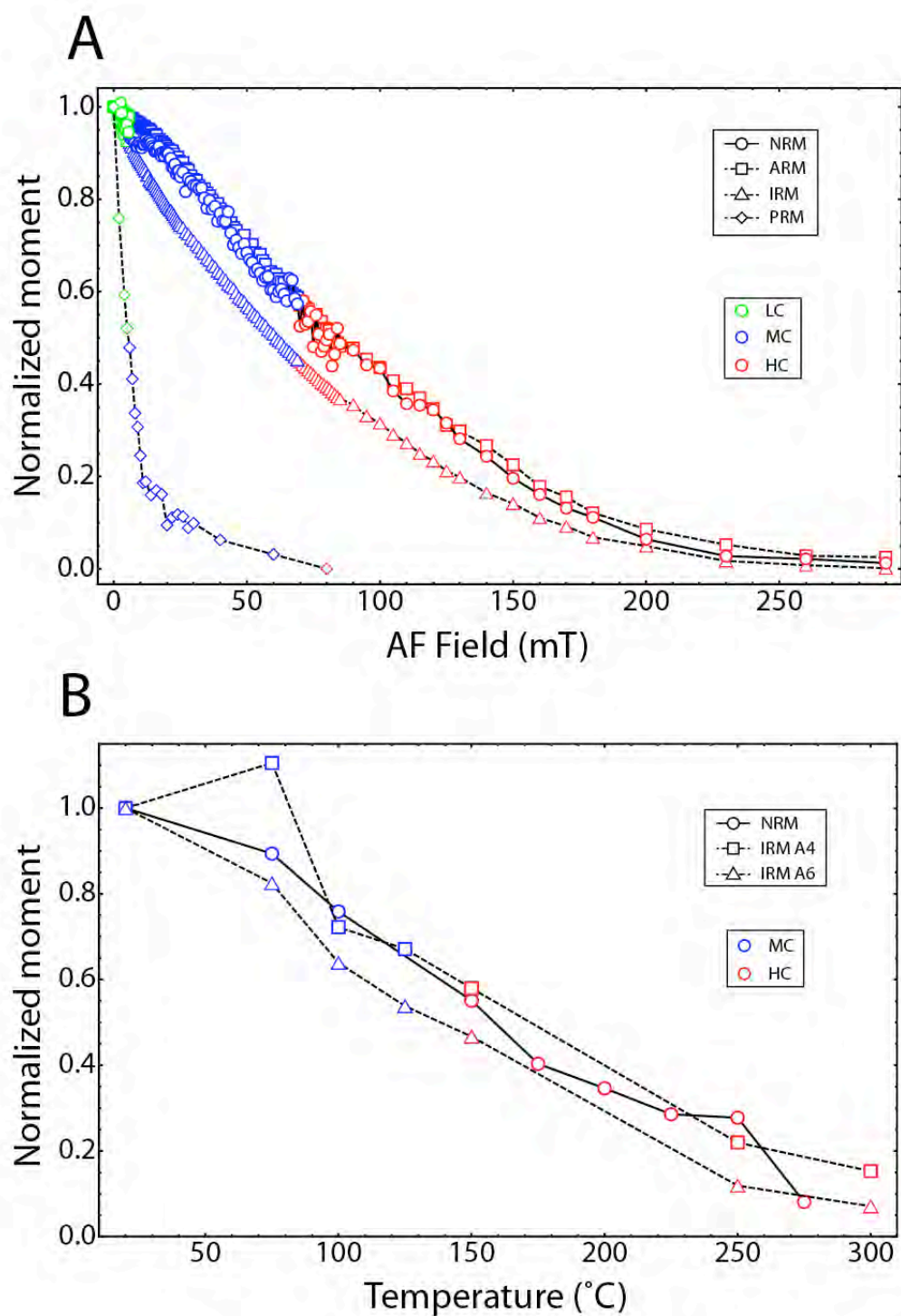
Fig. S14

AF and thermal demagnetization spectra. (**A**) AF demagnetization of the NRM in interior subsample A5 compared to that of an ARM and IRM for the same subsample and PRM for subsample B3. For both the HC and MC components of magnetization, the

NRM coercivity spectrum is similar to that of an ARM (AC field 280 mT; DC bias field 50 µT), but distinct from a strong field (280 mT) IRM or a PRM acquired at 1.8 GPa in a 750 µT background field. This suggests that the HC component is not a hand magnet overprint or a shock remanence and is consistent with a TRM origin. (**B**) Thermal demagnetization of the NRM in interior subsample B2 compared to that of a saturation IRM for the subsamples A4 and A6. Possible mineralogical alteration prevents using the same subsample for multiple thermal demagnetization runs. Plotted NRM moments have been corrected for the non-parallel directions of the HC/HT, MC/MT, and LC components.
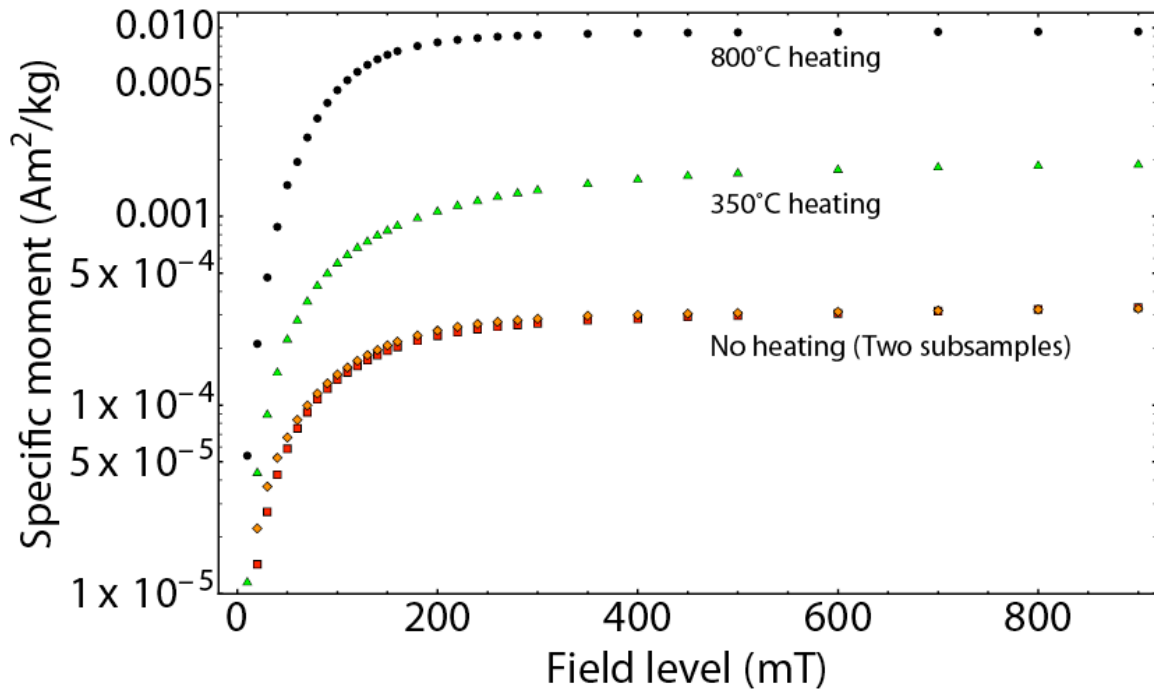
Fig. S15

IRM acquisition experiments. Starting with an AF-demagnetized subsample, magnitude of remanent magnetization is measured after IRM acquisition at progressively higher fields up to 900 mT. Experiment performed on two unheated subsamples (A4 and C4), one subsample heated to 350˚C (B2), and one subsample heated to 800˚C (A3). The large increases in the intensity of saturation IRM for the heated subsamples suggest that changes to the magnetic mineralogy are occurring.
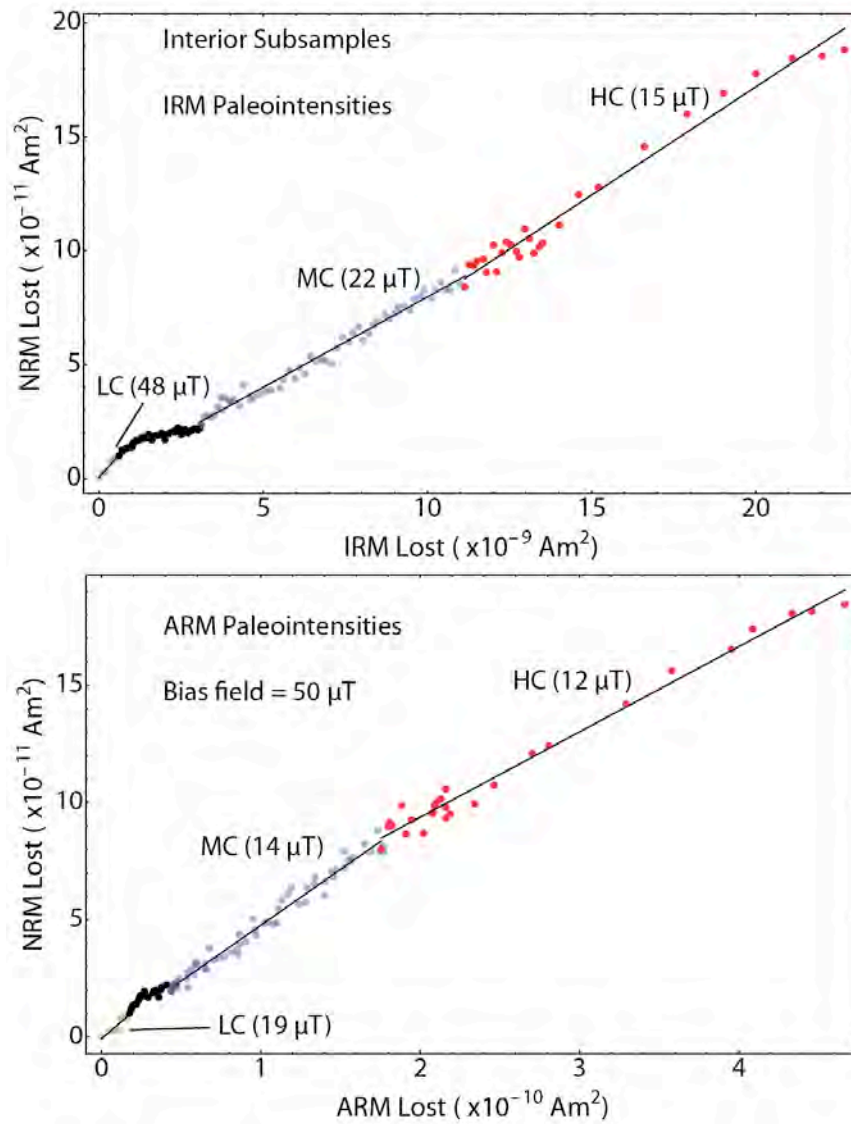
Fig. S16

Representative IRM and ARM paleointensity experiments for the interior subsample A5. Data points within each component are color-coded for clarity (compare with Figs. 2 and S11). Black data points between the LC and MC components do not constitute a component of magnetization due to lack of decay upon AF demagnetization.
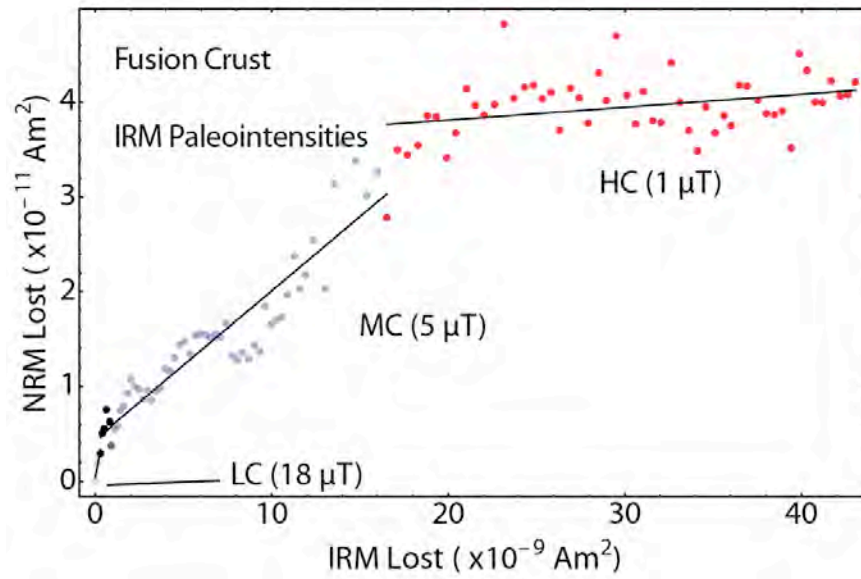
Fig. S17

Representative IRM paleointensity experiment for the fusion crusted subsample B1.
Black data points between the LC and MC components do not constitute a component of
magnetization due to lack of decay upon AF demagnetization.
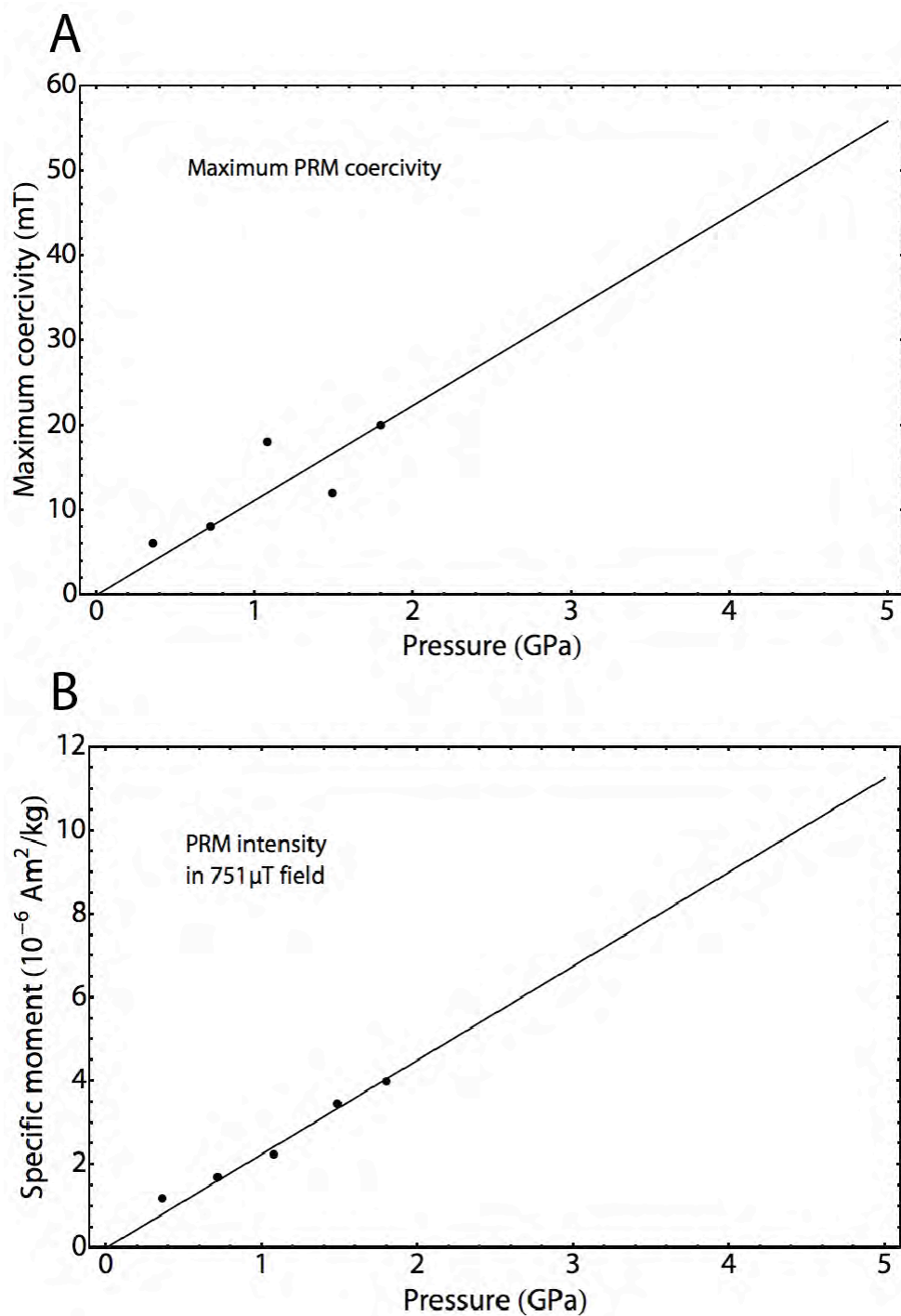
Fig. S18

PRM experiments on interior subsample B3. Shown are the (**A**) intensity and (**B**) maximum coercivity of PRM acquired in a laboratory field of 750 μT under pressures of up to 1.8 GPa. The trends are linearly extrapolated up to a maximum possible shock pressure of 5 GPa as indicated by the petrography of ALHA81001.
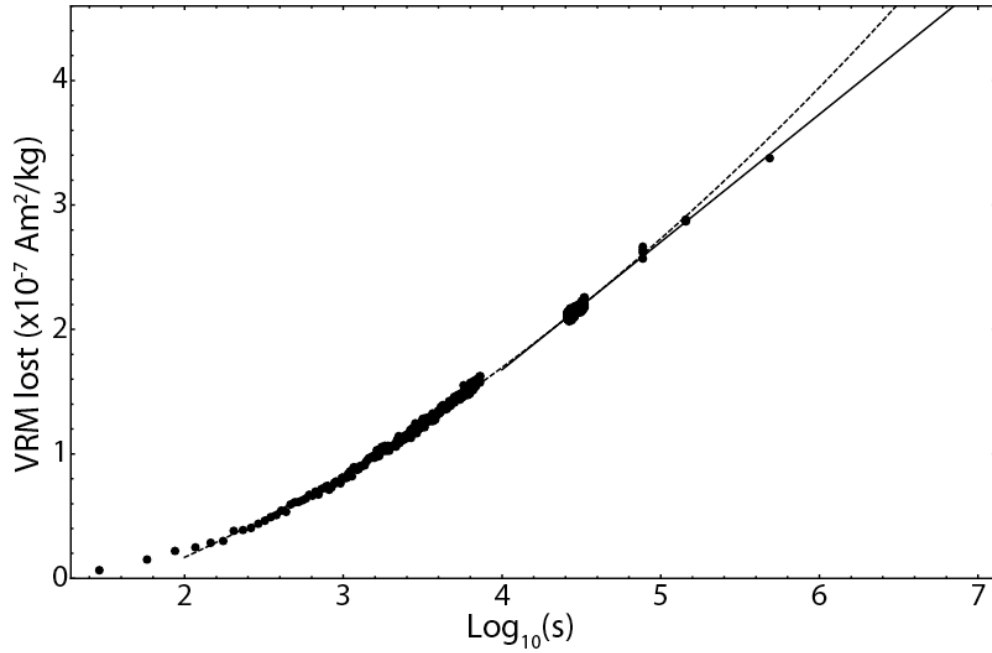
Fig. S19

VRM decay experiments on interior subsample B2. Shown is the progressive decay of a VRM acquired at room temperature over 13 days in the Earth's field as the subsample subsequently resided for 6 days in our shielded room (DC field < 150 nT). The solid line is a linear fit to data acquired after 10^4 s. The dotted line is an alternative quadratic fit to data after 100 s.

Table S1: Analytical Details

COMPLETE ^{40}Ar/^{39}Ar INCREMENTAL HEATING RESULTS

| #	Temp (°C)	^{40}Ar ± 1σ	^{39}Ar ± 1σ	^{38}Ar ± 1σ	^{37}Ar ± 1σ	^{36}Ar ± 1σ	^{40}Ar* (%)	^{39}Ar$_k$ (%)	^{38}Ar$_{cos}$ (%)	^{38}Ar$_{trap}$ (%)	^{38}Ar$_{Cl}$ (%)	^{36}Ar$_{cos}$ (%)	^{36}Ar$_{trap}$ (%)	Ca/K	Apparent Age ± 1s (Ma)
ALHA81001-a		**whole-rock fragment**													
1	463 °C	5.47704 ± 0.00501	0.01441 ± 0.00016	0.00209 ± 0.00003	0.31923 ± 0.00316	0.00145 ± 0.00002	100.0	98.5	90.1	0.0	0.0	100.0	0.0	44.1	3215 ± 26
2	463 °C	3.67778 ± 0.00381	0.00798 ± 0.00016	0.00119 ± 0.00002	0.18938 ± 0.00206	0.00084 ± 0.00002	100.0	98.4	90.1	1.5	0.0	82.7	11.3	47.3	3511 ± 37
3	516 °C	12.28800 ± 0.00731	0.02820 ± 0.00023	0.00403 ± 0.00004	0.63989 ± 0.00422	0.00276 ± 0.00003	100.0	98.4	90.2	1.1	0.0	85.4	8.4	45.2	3424 ± 24
4	517 °C	6.77744 ± 0.00331	0.01419 ± 0.00025	0.00504 ± 0.00004	0.29446 ± 0.00278	0.00141 ± 0.00002	100.0	98.6	89.9	1.4	0.0	83.5	11.0	41.3	3564 ± 35
5	570 °C	17.13983 ± 0.01200	0.03587 ± 0.00029	0.00587 ± 0.00004	0.77287 ± 0.00422	0.00342 ± 0.00003	100.0	98.5	90.1	1.0	0.0	86.0	8.1	42.9	3565 ± 24
6	569 °C	9.47658 ± 0.00731	0.01830 ± 0.00022	0.00239 ± 0.00003	0.35750 ± 0.00318	0.00161 ± 0.00003	100.0	98.6	89.5	1.0	0.0	86.4	7.7	38.8	3689 ± 28
7	622 °C	21.17489 ± 0.00701	0.04143 ± 0.00052	0.00562 ± 0.00004	0.83894 ± 0.00456	0.00372 ± 0.00003	100.0	98.6	90.1	0.8	0.0	87.9	6.1	40.3	3669 ± 29
8	622 °C	11.77344 ± 0.00581	0.02442 ± 0.00031	0.00278 ± 0.00004	0.40788 ± 0.00343	0.00191 ± 0.00003	100.0	98.8	87.6	1.5	0.0	82.6	11.7	33.1	3574 ± 29
9	675 °C	22.66666 ± 0.01200	0.04272 ± 0.00034	0.00569 ± 0.00004	0.83560 ± 0.00466	0.00371 ± 0.00004	100.0	98.6	90.1	0.5	0.0	89.6	4.5	38.9	3727 ± 24
10	675 °C	12.99372 ± 0.00631	0.02704 ± 0.00024	0.00295 ± 0.00003	0.44791 ± 0.00377	0.00209 ± 0.00003	100.0	98.7	86.6	2.0	0.0	79.0	15.3	32.8	3569 ± 25
11	727 °C	23.37534 ± 0.01400	0.04629 ± 0.00064	0.00600 ± 0.00005	0.87796 ± 0.00516	0.00406 ± 0.00004	100.0	98.7	89.3	1.1	0.0	85.6	8.7	37.7	3649 ± 30
12	727 °C	12.97315 ± 0.00721	0.02656 ± 0.00028	0.00315 ± 0.00004	0.46153 ± 0.00393	0.00216 ± 0.00003	100.0	98.8	88.2	1.4	0.0	83.4	10.9	34.5	3595 ± 27
13	701 °C	5.29505 ± 0.00301	0.01041 ± 0.00018	0.00124 ± 0.00003	0.18856 ± 0.00217	0.00086 ± 0.00002	100.0	98.7	88.1	1.5	0.0	82.5	11.7	36.0	3659 ± 34
14	780 °C	17.54631 ± 0.00820	0.03407 ± 0.00050	0.00484 ± 0.00004	0.69756 ± 0.00460	0.00332 ± 0.00003	100.0	98.6	90.0	1.2	0.0	85.0	9.5	40.7	3681 ± 31
15	830 °C	17.89309 ± 0.00920	0.03730 ± 0.00033	0.00521 ± 0.00005	0.73186 ± 0.00386	0.00352 ± 0.00003	100.0	98.6	90.1	1.0	0.0	86.5	7.9	39.0	3569 ± 25
16	830 °C	8.04044 ± 0.00571	0.01596 ± 0.00022	0.00221 ± 0.00003	0.30150 ± 0.00314	0.00157 ± 0.00003	100.0	98.7	89.3	1.8	0.0	81.5	13.4	37.5	3645 ± 30
17	881 °C	9.98495 ± 0.00571	0.01920 ± 0.00027	0.00388 ± 0.00004	0.52296 ± 0.00364	0.00269 ± 0.00003	100.0	98.1	92.7	1.1	0.0	86.7	8.2	54.4	3704 ± 31
18	881 °C	5.52507 ± 0.00451	0.01122 ± 0.00018	0.00209 ± 0.00003	0.27443 ± 0.00259	0.00146 ± 0.00002	100.0	98.3	92.0	1.3	0.0	85.3	9.8	48.8	3616 ± 33
19	933 °C	7.84110 ± 0.00471	0.01713 ± 0.00020	0.00481 ± 0.00004	0.61534 ± 0.00406	0.00336 ± 0.00003	100.0	97.5	94.5	1.0	0.0	87.7	7.5	72.2	3514 ± 28
20	932 °C	4.43159 ± 0.00261	0.00919 ± 0.00021	0.00240 ± 0.00003	0.31988 ± 0.00275	0.00174 ± 0.00002	100.0	97.6	93.6	1.6	0.0	83.6	11.5	69.9	3593 ± 42
21	984 °C	7.88739 ± 0.00501	0.01741 ± 0.00037	0.00900 ± 0.00005	1.19480 ± 0.00639	0.00653 ± 0.00004	100.0	95.2	96.2	1.3	0.0	85.9	9.3	141.2	3535 ± 40
22	982 °C	3.90792 ± 0.00331	0.00834 ± 0.00020	0.00396 ± 0.00004	0.54282 ± 0.00391	0.00292 ± 0.00003	100.0	95.5	95.8	1.5	0.0	84.1	11.0	133.5	3583 ± 45
23	1034 °C	7.95540 ± 0.00481	0.01704 ± 0.00020	0.01687 ± 0.00006	2.42311 ± 0.01007	0.01236 ± 0.00005	100.0	91.3	97.4	1.2	0.0	86.1	8.7	309.3	3668 ± 29
24	1034 °C	2.60869 ± 0.00202	0.00654 ± 0.00017	0.00581 ± 0.00004	0.81829 ± 0.00532	0.00428 ± 0.00003	100.0	89.8	97.1	1.3	0.0	85.3	9.6	268.6	3403 ± 47
25	1084 °C	12.80726 ± 0.00561	0.02683 ± 0.00022	0.02659 ± 0.00009	3.94912 ± 0.01093	0.01937 ± 0.00006	100.0	89.8	97.5	1.1	0.0	86.7	7.9	321.4	3709 ± 26
26	1084 °C	10.64691 ± 0.00441	0.02030 ± 0.00022	0.01600 ± 0.00007	2.16674 ± 0.00675	0.01167 ± 0.00005	100.0	92.6	97.1	1.2	0.0	86.2	8.9	226.0	3810 ± 28
27	1134 °C	1.48907 ± 0.00143	0.00372 ± 0.00014	0.00200 ± 0.00003	0.23651 ± 0.00277	0.00141 ± 0.00002	100.0	95.6	96.7	0.9	0.0	88.7	6.9	130.2	3337 ± 63
28	1132 °C	BDL	BDL	BDL	BDL	BDL									
29	1182 °C	BDL	BDL	BDL	BDL	BDL									
ALHA81001-b		**whole-rock fragment**													
1	460 °C	3.37370 ± 0.00380	0.00790 ± 0.00013	0.00123 ± 0.00002	0.19257 ± 0.00184	0.00087 ± 0.00002	100.0	98.3	90.5	1.5	0.0	11.3	11.3	48.6	3395 ± 32
2	460 °C	2.71049 ± 0.00271	0.00496 ± 0.00013	0.00092 ± 0.00002	0.15038 ± 0.00167	0.00062 ± 0.00001	100.0	97.9	92.5	0.7	0.0	88.1	5.5	60.7	3785 ± 48
3	514 °C	10.57928 ± 0.00730	0.01924 ± 0.00019	0.00385 ± 0.00004	0.59808 ± 0.00408	0.00254 ± 0.00002	100.0	97.8	93.4	0.3	0.0	91.5	2.2	62.3	3796 ± 26
4	513 °C	6.42971 ± 0.00511	0.01039 ± 0.00021	0.00191 ± 0.00002	0.31830 ± 0.00289	0.00135 ± 0.00002	100.0	97.9	91.9	1.3	0.0	84.3	9.4	61.3	3985 ± 39
5	567 °C	16.67865 ± 0.00730	0.02964 ± 0.00024	0.00511 ± 0.00004	0.80680 ± 0.00475	0.00341 ± 0.00003	100.0	98.1	92.2	0.6	0.0	89.3	4.4	54.4	3829 ± 25
6	567 °C	9.53739 ± 0.00632	0.01635 ± 0.00023	0.00237 ± 0.00003	0.37604 ± 0.00293	0.00158 ± 0.00002	100.0	98.4	90.7	0.7	0.0	88.1	5.6	45.8	3881 ± 31
7	620 °C	21.62650 ± 0.01201	0.03847 ± 0.00033	0.00572 ± 0.00005	0.86140 ± 0.00507	0.00382 ± 0.00004	100.0	98.4	90.9	0.8	0.0	88.0	6.0	44.6	3822 ± 25
8	620 °C	12.06518 ± 0.00729	0.02018 ± 0.00027	0.00286 ± 0.00004	0.42243 ± 0.00334	0.00183 ± 0.00003	100.0	98.5	91.0	0.2	0.0	92.2	1.6	41.6	3918 ± 31
9	672 °C	23.63994 ± 0.01501	0.04485 ± 0.00036	0.00586 ± 0.00005	0.89914 ± 0.00532	0.00387 ± 0.00003	100.0	98.6	89.8	0.7	0.0	88.0	5.8	39.8	3717 ± 24
10	672 °C	13.22718 ± 0.00786	0.02377 ± 0.00034	0.00305 ± 0.00003	0.45490 ± 0.00311	0.00190 ± 0.00003	100.0	98.7	90.3	0.0	0.0	93.7	-0.1	38.0	3802 ± 31
11	726 °C	23.91597 ± 0.01901	0.04623 ± 0.00039	0.00612 ± 0.00005	0.90665 ± 0.00430	0.00396 ± 0.00004	100.0	98.6	90.2	0.0	0.0	90.3	3.7	39.0	3687 ± 25
12	725 °C	13.43110 ± 0.00538	0.02453 ± 0.00029	0.00324 ± 0.00004	0.47333 ± 0.00397	0.00211 ± 0.00003	100.0	98.7	90.0	0.0	0.0	89.4	4.7	38.3	3777 ± 28
13	777 °C	20.22008 ± 0.01101	0.03859 ± 0.00050	0.00566 ± 0.00004	0.80124 ± 0.00510	0.00366 ± 0.00003	100.0	98.6	91.2	0.4	0.0	91.2	3.0	41.3	3709 ± 29
14	776 °C	10.57045 ± 0.00766	0.01915 ± 0.00030	0.00269 ± 0.00004	0.38604 ± 0.00383	0.00175 ± 0.00003	100.0	98.5	90.7	0.4	0.0	90.5	3.6	40.1	3790 ± 33
15	828 °C	14.05374 ± 0.00911	0.02699 ± 0.00028	0.00415 ± 0.00004	0.59133 ± 0.00442	0.00292 ± 0.00003	100.0	98.5	90.5	0.4	0.0	83.6	11.0	43.6	3700 ± 27
16	829 °C	6.72083 ± 0.00404	0.01287 ± 0.00023	0.00187 ± 0.00003	0.27027 ± 0.00276	0.00130 ± 0.00002	100.0	98.5	90.1	1.4	0.0	84.0	10.5	41.8	3703 ± 35
17	880 °C	8.40643 ± 0.00791	0.01735 ± 0.00021	0.00349 ± 0.00003	0.44954 ± 0.00381	0.00236 ± 0.00002	100.0	98.2	93.0	0.8	0.0	89.0	6.0	51.7	3592 ± 28
18	880 °C	4.61914 ± 0.00269	0.00835 ± 0.00037	0.00183 ± 0.00003	0.23614 ± 0.00261	0.00113 ± 0.00002	100.0	98.0	94.2	0.0	0.0	94.2	0.3	56.5	3803 ± 75
19	931 °C	6.78666 ± 0.00563	0.01320 ± 0.00022	0.00420 ± 0.00004	0.56063 ± 0.00492	0.00292 ± 0.00003	100.0	97.0	95.2	0.8	0.0	88.6	6.4	85.8	3703 ± 34
20	931 °C	4.17624 ± 0.00428	0.00658 ± 0.00023	0.00224 ± 0.00003	0.28979 ± 0.00332	0.00157 ± 0.00002	100.0	96.9	95.3	0.0	0.0	87.8	7.3	89.0	4040 ± 62
21	982 °C	6.99284 ± 0.00531	0.01426 ± 0.00020	0.00745 ± 0.00004	0.97606 ± 0.00576	0.00530 ± 0.00003	100.0	95.6	96.6	1.0	0.0	87.9	7.2	140.9	3659 ± 31
22	982 °C	3.87908 ± 0.00334	0.00742 ± 0.00019	0.00343 ± 0.00003	0.47162 ± 0.00423	0.00250 ± 0.00002	100.0	95.2	95.9	1.4	0.0	85.1	9.9	130.3	3753 ± 48
23	1032 °C	7.82809 ± 0.00672	0.01830 ± 0.00023	0.01586 ± 0.00007	2.30342 ± 0.00800	0.01149 ± 0.00004	100.0	91.3	97.4	1.0	0.0	87.0	7.7	270.4	3512 ± 30
24	1033 °C	2.75681 ± 0.00189	0.00576 ± 0.00015	0.00485 ± 0.00005	0.87334 ± 0.00521	0.00350 ± 0.00004	100.0	89.5	97.5	0.8	0.0	87.4	6.0	332.4	3720 ± 50
25	1083 °C	18.53826 ± 0.01001	0.03532 ± 0.00034	0.04230 ± 0.00013	6.27083 ± 0.01603	0.03080 ± 0.00007	100.0	87.7	97.8	1.0	0.0	87.0	7.6	397.0	3898 ± 28
26	1083 °C	3.00713 ± 0.00211	0.00495 ± 0.00024	0.00532 ± 0.00005	0.70466 ± 0.00468	0.00377 ± 0.00004	100.0	90.1	98.0	0.7	0.0	89.4	5.6	309.8	4089 ± 89
27	1132 °C	BDL	BDL	BDL	BDL	BDL									
28	1132 °C	BDL	BDL	BDL	BDL	BDL									
29	1182 °C	BDL	BDL	BDL	BDL	BDL									

Table S1: Analytical details (continued)

ALHA81001-c   whole-rock fragment

#	Temp															Age
1	460 °C	6.05767 ± 0.00380	0.01061 ± 0.00029	0.00237 ± 0.00010	0.34381 ± 0.00422	0.00156 ± 0.00009	100.0	97.7	94.2	0.1	0.0	1.2	1.2	65.0	3857 ± 49
2	460 °C	3.70396 ± 0.00310	0.00537 ± 0.00027	0.00120 ± 0.00010	0.19271 ± 0.00382	0.00077 ± 0.00009	100.0	97.5	94.3	0.0	0.0	0.3	93.0	72.1	4165 ± 86
3	513 °C	11.14838 ± 0.00850	0.01776 ± 0.00039	0.00381 ± 0.00010	0.58921 ± 0.00638	0.00256 ± 0.00009	100.0	97.7	93.7	0.4	0.0	3.3	90.6	66.6	4011 ± 42
4	514 °C	6.05440 ± 0.00510	0.00892 ± 0.00028	0.00180 ± 0.00010	0.28094 ± 0.00426	0.00113 ± 0.00009	100.0	97.8	93.7	0.0	0.0	0.3	93.2	63.1	4136 ± 57
5	567 °C	15.06382 ± 0.00530	0.02517 ± 0.00035	0.00461 ± 0.00010	0.70853 ± 0.00552	0.00308 ± 0.00010	100.0	98.0	92.7	0.5	0.0	3.9	90.0	56.3	3929 ± 31
6	566 °C	8.56080 ± 0.00510	0.01462 ± 0.00029	0.00218 ± 0.00010	0.33222 ± 0.00454	0.00144 ± 0.00009	100.0	98.4	91.1	0.6	0.0	4.8	89.1	45.3	3888 ± 38
7	619 °C	18.91700 ± 0.01000	0.03228 ± 0.00047	0.00503 ± 0.00011	0.75156 ± 0.00713	0.00331 ± 0.00010	100.0	98.4	91.5	0.5	0.0	4.0	90.0	46.4	3889 ± 32
8	620 °C	10.63206 ± 0.00890	0.01952 ± 0.00033	0.00244 ± 0.00010	0.38021 ± 0.00474	0.00164 ± 0.00009	100.0	98.6	89.0	1.0	0.0	8.3	85.6	38.7	3768 ± 34
9	672 °C	21.25314 ± 0.01200	0.04013 ± 0.00038	0.00518 ± 0.00010	0.76884 ± 0.00622	0.00359 ± 0.00010	100.0	98.7	88.9	1.5	0.0	11.2	83.1	38.1	3724 ± 26
10	672 °C	11.96133 ± 0.00490	0.02289 ± 0.00036	0.00272 ± 0.00010	0.40765 ± 0.00484	0.00178 ± 0.00009	100.0	98.8	88.8	0.7	0.0	6.1	87.9	35.3	3701 ± 33
11	724 °C	21.86970 ± 0.01300	0.04261 ± 0.00041	0.00551 ± 0.00010	0.78973 ± 0.00756	0.00363 ± 0.00010	100.0	98.7	89.7	0.7	0.0	6.0	88.2	36.8	3674 ± 26
12	724 °C	12.44359 ± 0.00740	0.02332 ± 0.00032	0.00291 ± 0.00010	0.42396 ± 0.00560	0.00188 ± 0.00010	100.0	98.7	89.6	0.5	0.0	4.2	89.8	36.1	3735 ± 30
13	777 °C	19.52296 ± 0.01100	0.03803 ± 0.00040	0.00479 ± 0.00010	0.70618 ± 0.00698	0.00324 ± 0.00010	100.0	98.7	89.0	1.2	0.0	9.1	85.1	36.9	3674 ± 27
14	776 °C	10.39553 ± 0.00680	0.02021 ± 0.00033	0.00248 ± 0.00010	0.35909 ± 0.00505	0.00160 ± 0.00009	100.0	98.8	89.3	0.6	0.0	4.7	89.3	35.3	3676 ± 33
15	829 °C	13.56072 ± 0.00780	0.02558 ± 0.00036	0.00361 ± 0.00011	0.52016 ± 0.00603	0.00252 ± 0.00010	100.0	98.6	89.7	1.5	0.0	11.3	83.2	40.4	3727 ± 31
16	829 °C	6.66052 ± 0.00621	0.01276 ± 0.00032	0.00170 ± 0.00010	0.23459 ± 0.00444	0.00119 ± 0.00009	100.0	98.7	89.1	1.6	0.0	12.4	82.4	36.5	3700 ± 45
17	880 °C	8.48594 ± 0.00621	0.01567 ± 0.00033	0.00303 ± 0.00010	0.40009 ± 0.00580	0.00209 ± 0.00009	100.0	98.2	92.5	1.1	0.0	8.4	86.6	50.9	3766 ± 40
18	880 °C	4.68215 ± 0.00261	0.00811 ± 0.00028	0.00147 ± 0.00010	0.20584 ± 0.00453	0.00112 ± 0.00009	100.0	98.2	90.5	2.6	0.0	18.2	76.9	50.7	3868 ± 60
19	931 °C	7.27816 ± 0.00321	0.01331 ± 0.00031	0.00383 ± 0.00010	0.48706 ± 0.00568	0.00271 ± 0.00009	100.0	97.5	94.4	1.2	0.0	9.1	86.2	73.6	3794 ± 44
20	931 °C	4.35189 ± 0.00401	0.00714 ± 0.00027	0.00193 ± 0.00010	0.26609 ± 0.00483	0.00144 ± 0.00009	100.0	97.4	93.3	2.0	0.0	14.2	80.9	75.0	3968 ± 66
21	982 °C	6.90729 ± 0.00324	0.01306 ± 0.00029	0.00694 ± 0.00011	0.91308 ± 0.00733	0.00525 ± 0.00010	100.0	95.1	95.6	1.9	0.0	13.6	81.8	144.1	3780 ± 42
22	982 °C	3.58380 ± 0.00401	0.00612 ± 0.00027	0.00303 ± 0.00010	0.46657 ± 0.00538	0.00224 ± 0.00009	100.0	95.4	95.8	1.6	0.0	11.4	83.8	136.4	3937 ± 78
23	1033 °C	7.62681 ± 0.00312	0.01569 ± 0.00035	0.01462 ± 0.00012	1.99491 ± 0.01132	0.01044 ± 0.00010	100.0	91.2	97.7	0.8	0.0	6.3	88.6	273.3	3713 ± 44
24	1033 °C	3.01719 ± 0.00341	0.00581 ± 0.00027	0.00600 ± 0.00010	0.83695 ± 0.00663	0.00444 ± 0.00010	100.0	90.0	97.3	1.4	0.0	9.8	85.2	313.7	3838 ± 85
25	1083 °C	15.74394 ± 0.01104	0.02754 ± 0.00040	0.03120 ± 0.00015	4.58943 ± 0.01427	0.02323 ± 0.00011	100.0	88.4	97.3	1.4	0.0	10.1	84.7	369.4	4021 ± 34
26	1082 °C	5.66572 ± 0.00450	0.00983 ± 0.00029	0.00749 ± 0.00011	1.04800 ± 0.00782	0.00565 ± 0.00010	100.0	92.6	96.5	1.7	0.0	12.2	82.9	225.6	3959 ± 55
27	1132 °C	BDL	BDL	BDL	BDL	BDL									
28	1132 °C	BDL	BDL	BDL	BDL	BDL									

Isotope abundances given in nanoamps (spectrometer sensivity is ~1.4 x 10^{-10} mols/nA),
and corrected for [37]Ar and [39]Ar decay, half lives of 35.2 days and 269 years, respectively,
and for spectrometer discrimination per atomic mass unit of 1.004535 ± 0.002968.

Isotope sources calculated using the reactor constants in Renne et al. (1998),
assuming ([38]Ar/[36]Ar)$_{cos}$ = 1.54, ([38]Ar/[36]Ar)$_{trap}$ = 0.188, and ([40]Ar/[36]Ar)$_{trap}$ = 0.

No corrections were made for cosmogenic [40]Ar.

Ages calculated using the decay constants and standard calibration of Renne et al. (2011) and isotope abundances of Steiger and Jäger (1977)
and calculated relative to Hb3gr fluence monitor (1081 Ma).

J-Value is 0.012746 ± 0.0001683.

Average analytical blanks are: [40]Ar = 0.015; [39]Ar = 0.0001; [38]Ar = 0.00002; [37]Ar = 0.0001; [36]Ar = 0.00007 (nanoamps).

Temperature was controlled with approximately ± 5 °C precision and ± 10 °C accuracy; each heating duration was 600 seconds.

Steps shown in gray are indeterminate or below the detection limit.

Table S2: Summary of cosmic ray exposure ages

Aliquot	Steps Used	Cosmochron Analysis $^{38}Ar_{cos}/^{37}Ar_{Ca} \pm 1$	CRE Age (Ma) ± 1
ALHA81001,a	1 - 14	0.00595 ± 0.00019	15.2 ± 0.5
ALHA81001,b	1 - 14	0.00597 ± 0.00026	15.2 ± 0.7
ALHA81001,c	1 - 14	0.00606 ± 0.00018	15.5 ± 0.5

CRE Ages calculated using the following parameters:
^{38}Ar Prod. Rate = 8.095×10^{-13} moles/gCa/Ma:
γ, which relates ^{37}Ar produced during the neutron irradiation
to the mass of Ca, is 2.06×10^{-9} moles/gCa

Table S3: Summary of Arrhenius regressions

Aliquot	Isotope	Steps Used	E_a (kJ/mol) $\pm$ 1σ	$\ln(D_o/a^2)$ [ln(s^{-1})] $\pm$ 1σ
			High E_a regressions	
ALHA81001,a	^{39}Ar	1 - 4	202.3 $\pm$ 2.2	17.3 $\pm$ 0.4
	^{37}Ar		198.2 $\pm$ 1.7	16.9 $\pm$ 0.3
ALHA81001,b	^{39}Ar	1 - 4	218.6 $\pm$ 2.9	19.2 $\pm$ 0.5
	^{37}Ar		**238.2 $\pm$ 1.6**	**22.7 $\pm$ 0.3**
ALHA81001,c	^{39}Ar	1 - 4	174.9 $\pm$ 5.3	12.7 $\pm$ 0.8
	^{37}Ar		180.9 $\pm$ 2.5	14.4 $\pm$ 0.4
			Low E_a regressions	
ALHA81001,a	^{39}Ar	5 - 19	95.2 $\pm$ 0.8	1.1 $\pm$ 0.1
	^{37}Ar		83.0 $\pm$ 0.5	-0.6 $\pm$ 0.0
ALHA81001,b	^{39}Ar	5 - 19	114.6 $\pm$ 0.7	3.5 $\pm$ 0.1
	^{37}Ar		93.4 $\pm$ 0.5	0.8 $\pm$ 0.1
ALHA81001,c	^{39}Ar	5 - 19	99.8 $\pm$ 1.6	1.6 $\pm$ 0.2
	^{37}Ar		**80.4 $\pm$ 0.8**	**-0.8 $\pm$ 0.1**

Values of E_a and D_o/a^2 determined from error-weighted linear regression to sub-selected steps.
Values shown in bold are the "high E_a" and "low E_a" values used in diffusion models.

Table S4: Summary of interior paleomagnetic samples and NRM components

Sample and Component	Mass (mg)	AF/Thermal Range (mT or ˚C)	Dec., Inc. (˚)	MAD (˚)	DANG (˚)	N_m
A1 – Fusion	17.7					
LC		0 - 3 mT	228.8, 46.0	12.3		30
MC		30 - 49 mT	304.0, -4.0	25.2		120
HCf		49 - >85 mT	254.2, 32.2	45.8	46.8	222
B1 – Fusion	36.8					
LC		0 - 2.5 mT	265.3, 70.3	10.0		24
MC		15 - 33 mT	164.8, -65.4	18.9		116
HCf		33 - >85 mT	281.2, -7.0	74.3	41.4	318
A2 – Intermediate	29.6					
LC		0 - 3 mT	219.5, 60.5	9.6		30
MC		20 - 61 mT	245.4, -57.2	40.4		282
HC/HCf		61 - >85 mT	134.5, -54.4	58.6	45.7	150
A3 – Intermediate	31.4					
LC		0 - 3 mT	238.4, 67.8	4.6		30
MC		25 - 37 mT	217.0, -64.2	22.6		72
HC/HCf		37 - >85 mT	70.2, -53.9	22.6	16.8	294
A4 – Interior	34.9					
LC		0 - 3 mT	206.3, 74.5	7.1		30
MC		21 - 72 mT	66.1, -64.6	16.1		224
HC		72 - >290 mT	67.8, -16.2	8.6	5.6	96
A5 – Interior	90.0					
LC		0 - 5.5 mT	228.9, 18.5	11.0		60
MC		15.5 - 69 mT	294.3, -82.3	12.1		256
HC		69 - >290 mT	63.6, -27.0	6.0	3.0	136
A6 – Interior	102.6					
LC		0 - 3 mT	187.2, 60.7	15.0		92
MC		20.5 - 63 mT	265.2, -59.2	8.4		192
HC		63 - >290 mT	69.3, -26.0	8.0	2.5	136
B2 – Interior	127.1					
LC		0 - 3 mT	334.2, 64.4	8.2		20
MC		150˚C	274.1, -76.3	17.2		4
HC		>275˚C	71.1, -28.4	10.7	11.1	6
B3 – Interior	130.1					
LC		0 - 2.5 mT	122.8, 79.6	30.6		16
MC		17.5 - 71 mT	208.7, -47.3	29.6		248
HC		71 - 260 mT	67.1, -27.2	33.9	12.3	100

Note: All subsamples in table are mutually oriented to within ~5˚. The first column gives the subsample or component name; the second column gives the subsample mass; the third column gives the range of AF fields or temperatures in which the

component is blocked; the fourth column gives the orientation of the magnetization vector as determined from least squares fitting; the fifth column gives the maximum angular deviation (MAD) of the component (see SOM text); the sixth column gives the deviation angle (DANG); and the seventh column gives the number of individual measurements of the magnetic moment associated with each component.

Table S5: Paleointensity slopes for LC and MC components

Subsample	LC Component		MC Component	
	IRM slope	ARM slope	IRM slope	ARM slope
A1 – Fusion	0.013	0.27	0.0016	0.21
B1 – Fusion	0.0059	0.27	0.0018	0.31
A3 – Intermediate	0.015	0.40	0.0077	0.48
A4 – Interior	0.012	0.46	0.0050	0.27
A5 – Interior	0.016	0.59	0.0073	0.48
A6 – Interior	0.0040	0.59	0.010	0.59
B3 – Interior	0.0010	0.35	0.0033	0.19
Interior Mean	0.0065	0.51	0.0078	0.38

Note: For all but the last row, the first column identifies the name and location of the subsample; the second column gives the slopes of NRM lost vs. IRM lost for the LC component; the third column gives the slopes of NRM lost vs. ARM gained for the LC component; the fourth column gives the slopes of NRM lost vs. IRM lost for the MC component; the fifth column gives the slopes of NRM lost vs. ARM gained for the MC component. The final row gives the mean slopes for interior subsamples only.

Table S6: Paleointensities for HC and HCf components

Subsample	HC or HCf Component		
	ARM acquisition (µT)	Thermal demagnetization of IRM (µT)	AF of IRM (µT)
A1 – Fusion	0.8	N/A	1
B1 – Fusion	2	N/A	1
A3 – Intermediate	8	N/A	N/A
A4 – Interior	10	N/A	N/A
A5 – Interior	13	N/A	15
A6 – Interior	15	N/A	N/A
B3 – Interior	8	N/A	12
B2 – Interior	N/A	9 (A4); 13 (A6)	N/A
Interior Mean	12	11	14

Note: For the first eight rows, the first column identifies the name and location of the subsample; the second, third, and fourth columns give the inferred paleointensities for the HC component (interior subsamples) or HCf component (fusion crust subsamples) from each paleointensity method. Paleointensities for interior subsample B2 are calculated using the IRM measured in subsample A4 and A6 (see Section 3.4). The final row gives the mean values of the inferred paleointensity for interior subsamples only.

Table S7: Saturation remanence for Camel Donga samples

Sample	Parent Stone	Mass (mg)	M_{rs} ($\times 10^{-2}$ Am^2kg^{-1})
CD1	CD1	354.2	7.57
CD2	CD2	325.8	2.63
CD3a	CD3	275.1	4.98
CD3b	CD3	115.2	4.49
Weighted Mean			5.07

Note: The first column gives the sample name; the second column the individual stone (<2.5 g, fusion crusted on all or nearly all sides) from which the sample was extracted; the third column gives the sample mass; and the fourth column gives the measured saturation remanence. Weighted Mean is weighted by the mass of each sample, thereby yielding the saturation remanence if all samples were measured together.

References and Notes

1. J. E. Chambers, Planetary accretion in the inner Solar System. *Earth Planet. Sci. Lett.* **223**, 241 (2004). doi:10.1016/j.epsl.2004.04.031

2. C. T. Russell *et al.*, Dawn at Vesta: Testing the protoplanetary paradigm. *Science* **336**, 684 (2012). doi:10.1126/science.1219381 Medline

3. R. P. Binzel, S. Xu, Chips off of Asteroid 4 Vesta: Evidence for the parent body of basaltic achondrite meteorites. *Science* **260**, 186 (1993). doi:10.1126/science.260.5105.186 Medline

4. K. Righter, M. J. Drake, A magma ocean on Vesta: Core formation and petrogenesis of eucrites and diogenites. *Meteorit. Planet. Sci.* **32**, 929 (1997). [doi:10.1111/j.1945-5100.1997.tb01582.x](doi:10.1111/j.1945-5100.1997.tb01582.x)

5. The beginning of the solar system here refers to 4.567 to 4.568 Ga, which corresponds to the formation of calcium-aluminum–rich inclusions, the first macroscopic solids in the solar system.

6. T. Kleine *et al.*, Hf-W chronology of the accretion and early evolution of asteroids and terrestrial planets. *Geochim. Cosmochim. Acta* **73**, 5150 (2009). [doi:10.1016/j.gca.2008.11.047](doi:10.1016/j.gca.2008.11.047)

7. B. P. Weiss *et al.*, Magnetism on the angrite parent body and the early differentiation of planetesimals. *Science* **322**, 713 (2008). doi:10.1126/science.1162459 Medline

8. L. Carporzen *et al.*, Magnetic evidence for a partially differentiated carbonaceous chondrite parent body. *Proc. Natl. Acad. Sci. U.S.A.* **108**, 6386 (2011). doi:10.1073/pnas.1017165108

9. D. J. Stevenson, Planetary magnetic fields: Achievements and prospects. *Space Sci. Rev.* **152**, 651 (2010). [doi:10.1007/s11214-009-9572-z](doi:10.1007/s11214-009-9572-z)

10. S. M. Cisowski, Remanent magnetic properties of unbrecciated eucrites. *Earth Planet. Sci. Lett.* **107**, 173 (1991). [doi:10.1016/0012-821X(91)90053-K](doi:10.1016/0012-821X(91)90053-K)

11. See supplementary materials section 1.

12. D. W. Collinson, S. J. Morden, Magnetic properties of howardite, eucrite and diogenite (HED) meteorites: Ancient magnetizing fields and meteorite evolution. *Earth Planet. Sci. Lett.* **126**, 421 (1994). [doi:10.1016/0012-821X(94)90122-8](doi:10.1016/0012-821X(94)90122-8)

13. B. P. Weiss, J. Gattacceca, S. Stanley, P. Rochette, U. R. Christensen, Paleomagnetic records of meteorites and early planetesimal differentiation. *Space Sci. Rev.* **152**, 341 (2010). [doi:10.1007/s11214-009-9580-z](doi:10.1007/s11214-009-9580-z)

14. T. Nagata, *Mem. Natl. Inst. Polar Res. Spec. Issue* **17**, 233 (1980).

15. See supplementary materials sections 2.1 to 2.3.

16. E. R. D. Scott, R. C. Greenwood, I. Franchi, I. S. Sanders, Oxygen isotopic constraints on the origin and parent bodies of eucrites, diogenites, and howardites. *Geochim. Cosmochim. Acta* **73**, 5835 (2009). [doi:10.1016/j.gca.2009.06.024](doi:10.1016/j.gca.2009.06.024)

17. See supplementary materials section 2.3.

18. D. Walker, M. A. Powell, G. E. Lofgren, J. F. Hays, *Proc. Lunar Planet Sci. Conf. 9th*, 1369 (1978).

19. T. L. Grove, *Am. Mineral.* **67**, 251 (1982).

20. Undulatory extinction is characterized by dark bands that roll across a crystal when the sample is rotated during crossed-polar transmitted light microscopy. It is due to the realignment of crystallographic axes by heavy shock.

21. A. Bischoff, D. Stoffler, *Eur. J. Mineral.* **4**, 707 (1992).

22. See supplementary materials section 3.5.

23. See supplementary materials section 3.3.

24. A. Stephenson, D. W. Collinson, Lunar magnetic field palaeointensities determined by an anhysteretic remanent magnetization method. *Earth Planet. Sci. Lett.* **23**, 220 (1974). doi:10.1016/0012-821X(74)90196-4

25. I. Garrick-Bethell, B. P. Weiss, Kamacite blocking temperatures and applications to lunar magnetism. *Earth Planet. Sci. Lett.* **294**, 1 (2010). doi:10.1016/j.epsl.2010.02.013

26. D. J. Dunlop, O. Ozdemir, D. A. Clark, P. W. Schmidt, Time-temperature relations for the remagnetization of pyrrhotite (Fe_7S_8) and their use in estimating paleotemperatures. *Earth Planet. Sci. Lett.* **176**, 107 (2000). doi:10.1016/S0012-821X(99)00309-X

27. See supplementary materials section 3.4.

28. L. T. Elkins-Tanton, B. P. Weiss, M. T. Zuber, Chondrites as samples of differentiated planetesimals. *Earth Planet. Sci. Lett.* **305**, 1 (2011). doi:10.1016/j.epsl.2011.03.010

29. M. G. Sterenborg, J. L. Crowley, in *43rd Lunar and Planetary Science Conference* (Houston, TX, 2012), abstr. 2361.

30. K. E. Haisch Jr., E. A. Lada, C. J. Lada, Disk frequencies and lifetimes in young clusters. *Astrophys. J.* **553**, L153 (2001). doi:10.1086/320685

31. See supplementary materials section 4.4.

32. N. J. Turner, T. Sano, Dead zone accretion flows in protostellar disks. *Astrophys. J.* **679**, L131 (2008). doi:10.1086/589540

33. M. Miyamoto, H. Takeda, abstract in *57th Meeting of the Meteoritical Society* (Prague, 1994).

34. L. L. Hood, N. A. Artemieva, Antipodal effects of lunar basin-forming impacts: Initial 3D simulations and comparisons with observations. *Icarus* **193**, 485 (2008). doi:10.1016/j.icarus.2007.08.023

35. D. A. Crawford, P. H. Schultz, Electromagnetic properties of impact-generated plasma, vapor and debris. *Int. J. Impact Eng.* **23**, 169 (1999). doi:10.1016/S0734-743X(99)00070-6

36. L. L. Hood, A. Vickery, *Proc. Lunar Planet. Sci. Conf. 15th*, C211 (1984).

37. E. Pierazzo, A. M. Vickery, H. J. Melosh, A reevaluation of impact melt production. *Icarus* **127**, 408 (1997). doi:10.1006/icar.1997.5713

38. E. Asphaug, Impact origin of the Vesta family. *Meteorit. Planet. Sci.* **32**, 965 (1997). doi:10.1111/j.1945-5100.1997.tb01584.x

39. U. R. Christensen, J. Aubert, Scaling properties of convection-driven dynamos in rotating spherical shells and application to planetary magnetic fields. *Geophys. J. Int.* **166**, 97 (2006). doi:10.1111/j.1365-246X.2006.03009.x

40. M. A. Wieczorek, B. P. Weiss, S. T. Stewart, An impactor origin for lunar magnetic anomalies. *Science* **335**, 1212 (2012). doi:10.1126/science.1214773 Medline

41. P. Rochette *et al*., Magnetic classification of stony meteorites: 3. Achondrites. *Meteorit. Planet. Sci.* **44**, 405 (2009). doi:10.1111/j.1945-5100.2009.tb00741.x

42. J. Gattacceca, P. Rochette, Toward a robust normalized magnetic paleointensity method applied to meteorites. *Earth Planet. Sci. Lett.* **227**, 377 (2004). doi:10.1016/j.epsl.2004.09.013

43. See supplementary materials section 2.2.

44. V. Reddy *et al*., Color and albedo heterogeneity of Vesta from Dawn. *Science* **336**, 700 (2012). doi:10.1126/science.1219088 Medline

45. R. C. Greenwood, I. A. Franchi, A. Jambon, J. A. Barrat, T. H. Burbine, Oxygen isotope variation in stony-iron meteorites. *Science* **313**, 1763 (2006). doi:10.1126/science.1128865 Medline

46. L. L. Hood, A. Zakharian, Mapping and modeling of magnetic anomalies in the northern polar region of Mars. *J. Geophys. Res.* **106**, 14601 (2001). doi:10.1029/2000JE001304

47. M. C. De Sanctis *et al*., Spectroscopic characterization of mineralogy and its diversity across Vesta. *Science* **336**, 697 (2012). doi:10.1126/science.1219270 Medline

48. P. Vernazza *et al*., Asteroid colors: A novel tool for magnetic field detection? The case of Vesta. *Astron. Astrophys.* **451**, L43 (2006). doi:10.1051/0004-6361:20065176

49. H. Fechtig, S. Kalbitzer, in *Potassium-Argon Dating*, O. A. Schaeffer, J. Zahringer, Eds. (Springer, Heidelberg, 1966), pp. 68–106.

50. S. J. Morden, A magnetic study of the Millbillillie (eucrite) achondrite: Evidence for a dynamo-type magnetising field. *Meteoritics* **27**, 560 (1992). doi:10.1111/j.1945-5100.1992.tb01077.x

51. R. R. Fu, B. P. Weiss, in *EPSC-DPS Joint Meeting* (Nantes, France, 2011), abstr. 1646..

52. L. Li, B. P. Weiss, R. R. Fu, J. Gattacceca, C. Sonzogni, Paleomagnetism of an anomalous eucrite and implications for the diversity of asteroid dynamos. Paper presented at the AGU Fall Meeting, San Francisco, CA, 2011, abstr. GP21B-1001.

53. J. L. Gooding, *Antarct. Meteorite News.* **9**, 1 (1986).

54. M. A. Velbel, The distribution and significance of evaporitic weathering products on Antarctic meteorites. *Meteoritics* **23**, 151 (1988). doi:10.1111/j.1945-5100.1988.tb00910.x

55. E. K. Shea *et al*., A long-lived lunar core dynamo. *Science* **335**, 453 (2012). doi:10.1126/science.1215359 Medline

56. P. R. Renne, G. Balco, K. Ludwig, R. Mundil, K. Min, Response to the comment by W.H. Schwarz et al. on "Joint determination of ^{40}K decay constants and ^{40}Ar∗/^{40}K for the Fish Canyon sanidine standard, and improved accuracy for $_{40}$Ar/^{39}Ar geochronology" by P. R. Renne *et al*. (2010). *Geochim. Cosmochim. Acta* **75**, 5097 (2011). doi:10.1016/j.gca.2011.06.021

57. P. R. Renne, R. Mundil, G. Balco, K. Min, K. R. Ludwig, Joint determination of ^{40}K decay constants and ^{40}Ar∗/^{40}K for the Fish Canyon sanidine standard, and improved accuracy for ^{40}Ar/^{39}Ar geochronology. *Geochim. Cosmochim. Acta* **74**, 5349 (2010). doi:10.1016/j.gca.2010.06.017

58. R. H. Steiger, E. Jager, *Earth Planet. Sci. Lett.* **36**, 359 (1977).

59. W. Cassata, D. L. Shuster, P. R. Renne, B. P. Weiss, Evidence for shock heating and constraints on Martian surface temperatures revealed by ^{40}Ar/^{39}Ar thermochronometry of Martian meteorites. *Geochim. Cosmochim. Acta* **74**, 6900 (2010). doi:10.1016/j.gca.2010.08.027

60. J. Levine, P. R. Renne, R. A. Muller, Solar and cosmogenic argon in dated lunar impact spherules. *Geochim. Cosmochim. Acta* **71**, 1624 (2007). doi:10.1016/j.gca.2006.11.034

61. R. G. Mayne, H. Y. McSween Jr., T. J. McCoy, A. Gale, Petrology of the unbrecciated eucrites. *Geochim. Cosmochim. Acta* **73**, 794 (2009). doi:10.1016/j.gca.2008.10.035

62. F. Jourdan, J. P. Matzel, P. R. Renne, ^{39}Ar and ^{37}Ar recoil loss during neutron irradiation of sanidine and plagioclase. *Geochim. Cosmochim. Acta* **71**, 2791 (2007). doi:10.1016/j.gca.2007.03.017

63. A. Yamaguchi, G. J. Taylor, K. Keil, Global crustal metamorphism of the eucrite parent body. *Icarus* **124**, 97 (1996). doi:10.1006/icar.1996.0192

64. D. Stöffler, K. Keil, E. R. D. Scott, Shock metamorphism of ordinary chondrites. *Geochim. Cosmochim. Acta* **55**, 3845 (1991). doi:10.1016/0016-7037(91)90078-J

65. J. Crank, *The Mathematics of Diffusion* (Oxford University Press, Oxford, ed. 2, 1975).

66. P. Schenk *et al*., in *43rd Lunar and Planetary Science Conference* (Houston, TX, 2012), abstr. 2757.

67. B. P. Weiss, E. A. Lima, L. E. Fong, F. J. Baudenbacher, Paleomagnetic analysis using SQUID microscopy. *J. Geophys. Res.* **112**, B09105 (2007). doi:10.1029/2007JB004940

68. E. A. Lima, A. Irimia, J. P. Wikswo, in *The SQUID Handbook,* J. Clarke, A. I. Braginski, Eds. (Wiley-VCH, Weinheim, Germanym 2006), vol. 2, pp. 139–267.

69. D. J. Dunlop, *J. Geophys. Res.* **107**, (2002). 10.1029/2001JB000486

70. W. Lowrie, Identification of ferromagnetic minerals in a rock by coercivity and unblocking temperature properties. *Geophys. Res. Lett.* **17**, 159 (1990). doi:10.1029/GL017i002p00159

71. F. Martín-Hernández, M. J. Dekkers, I. M. A. Bominaar-Silkens, J. C. Maan, Magnetic anisotropy behaviour of pyrrhotite as determined by low- and high-field experiments. *Geophys. J. Int.* **174**, 42 (2008). doi:10.1111/j.1365-246X.2008.03793.x

72. D. J. Dunlop, O. Ozdemir, *Rock Magnetism: Fundamentals and Frontiers* (Cambridge Studies in Magnetism, Cambridge Univ. Press, New York, 1997).

73. G. W. Pearce, G. S. Hoye, D. W. Strangway, B. M. Walker, L. A. Taylor, *Proc. Lunar Sci. Conf. 7th*, 3271 (1976).

74. D. J. Vaughan, J. R. Craig, *Mineral Chemistry of Metal Sulfides* (Cambridge Univ. Press, Cambridge, 1978).

75. J. Gattacceca, P. Rochette, F. Lagroix, P. E. Mathé, B. Zanda, Low temperature magnetic transition of chromite in ordinary chondrites. *Geophys. Res. Lett.* **38**, L10203 (2011). doi:10.1029/2011GL047173

76. M. Uehara, J. Gattacceca, P. Rochette, F. Demory, E. M. Valenzuela, Magnetic study of meteorites recovered in the Atacama desert (Chile): Implications for meteorite paleomagnetism and the stability of hot desert surfaces. *Phys. Earth Planet. Inter.* **200-201**, 113 (2012). doi:10.1016/j.pepi.2012.04.007

77. C.-W. Yang, D. B. Williams, J. I. Goldstein, A revision of the Fe-Ni phase diagram at low temperatures (<400°C). *J. Phase Equilibria* **17**, 522 (1996). doi:10.1007/BF02665999

78. M. Uehara, J. Gattacceca, H. Leroux, D. Jacob, C. J. van der Beek, Magnetic microstructures of metal grains in equilibrated ordinary chondrites and implications for paleomagnetism of meteorites. *Earth Planet. Sci. Lett.* **306**, 241 (2011). doi:10.1016/j.epsl.2011.04.008

79. P. Wasilewski, Magnetic characterization of the new magnetic mineral tetrataenite and its contrast with isochemical taenite. *Phys. Earth Planet. Inter.* **52**, 150 (1988). doi:10.1016/0031-9201(88)90063-5

80. T. Nagata, *Proc. Lunar Sci. Conf. 11th*, 1789 (1980).

81. K. Kitts, K. Lodders, Survey and evaluation of eucrite bulk compositions. *Meteorit. Planet. Sci.* **33**, , A197 (1998). doi:10.1111/j.1945-5100.1998.tb01334.x

82. M. B. Duke, L. T. Silver, Petrology of eucrites, howardites and mesosiderites. *Geochim. Cosmochim. Acta* **31**, 1637 (1967). doi:10.1016/0016-7037(67)90112-3

83. A. Yamaguchi *et al*., A new source of basaltic meteorites inferred from Northwest Africa 011. *Science* **296**, 334 (2002). doi:10.1126/science.1069408 Medline

84. C. P. Hunt, B. M. Moskowitz, S. K. Banerjee, in *Rock Physics and Phase Relations. A Handbook of Physical Constants,* T. J. Ahrens, Ed. (American Geophysical Union, Washington, DC, 1995), pp. 189–204.

85. W. A. Gose, G. W. Pearce, D. W. Strangway, E. E. Larson, *Earth Moon Planets* **5**, 106 (1972).

86. D. J. Dunlop, W. A. Gose, G. W. Pearce, D. W. Strangway, *Proc. Lunar Sci. Conf. 4th*, 2977 (1973).

87. M. Fuller, Lunar magnetism. *Rev. Geophys. Space Phys.* **12**, 23 (1974). doi:10.1029/RG012i001p00023

88. C. Meyer, www-curator.jsc.nasa.gov/lunar/compendium.cfm (2011).

89. S. Mostefaoui, G. W. Lugmair, P. Hoppe, A. El Goresy, Evidence for live ^{60}Fe in meteorites. *New Astron. Rev.* **48**, 155 (2004). doi:10.1016/j.newar.2003.11.022

90. A. W. Beck *et al*., MIL 03443, a dunite from asteroid 4 Vesta: Evidence for its classification and cumulate origin. *Meteorit. Planet. Sci.* **46**, 1133 (2011). doi:10.1111/j.1945-5100.2011.01219.x

91. P. A. Bland, M. E. Zolensky, G. K. Benedix, M. A. Sephton, in *Meteorites and the Early Solar System II*, D. S. Lauretta, H. Y. McSween, Eds. (Univ. of Arizona Press, Tucson, AZ, 2006), pp. 853–867.

92. V. F. Buchwald, R. S. Clarke, *Am. Mineral.* **74**, 656 (1989).

93. J. L. Gooding, in *International Workshop on Antarctic Meteorites* (LPI Technical Report 86-01, Lunar and Planetary Science Institute, Houston, TX, 1986), pp. 48–54.

94. J. S. Delaney, M. Prinz, H. Takeda, The polymict eucrites. *J. Geophys. Res.* **89**, C251 (1984). doi:10.1029/JB089iS01p0C251

95. J.-P. Lorand, V. Chevrier, V. Sautter, Sulfide mineralogy and redox conditions in some shergottites. *Meteorit. Planet. Sci.* **40**, 1257 (2005). doi:10.1111/j.1945-5100.2005.tb00187.x

96. P. H. Warren, E. A. Jerde, Composition and origin of Nuevo Laredo Trend eucrites. *Geochim. Cosmochim. Acta* **51**, 713 (1987). doi:10.1016/0016-7037(87)90082-2

97. H. Shimizu, A. Masuda, T. Tanaka, *Mem. Natl. Inst. Polar Res.* **30**, 341 (1983).

98. D. W. Mittlefehldt, M. M. Lindstrom, Generation of abnormal trace element abundances in Antarctic eucrites by weathering processes. *Geochim. Cosmochim. Acta* **55**, 77 (1991). doi:10.1016/0016-7037(91)90401-P

99. A. Yamaguchi, H. Takeda, D. D. Bogard, D. H. Garrison, Textural variations and impact history of the Millbillillie eucrite. *Meteoritics* **29**, 237 (1994). doi:10.1111/j.1945-5100.1994.tb00677.x

100. E. M. Stolper, Experimental petrology of eucritic meteorites. *Geochim. Cosmochim. Acta* **41**, 587 (1977). doi:10.1016/0016-7037(77)90300-3

101. I. Garrick-Bethell, B. P. Weiss, D. L. Shuster, J. Buz, Early lunar magnetism. *Science* **323**, 356 (2009). doi:10.1126/science.1166804 Medline

102. J. L. Kirschvink, The least-squares line and plane and the analysis of palaeomagnetic data. *Geophys. J. R. Astron. Soc.* **62**, 699 (1980). doi:10.1111/j.1365-246X.1980.tb02601.x

103. A. Cox, *Geophys. J. R. Astron. Soc.* **18**, 545 (1969).

104. L. Tauxe, H. Staudigel, *Geochem. Geophys. Geosyst.* **5**, (2004). 10.1029/2003GC000635

105. A. R. Prunier, D. A. Hewitt, Calculation of temperature-oxygen fugacity tables for H_2-Co_2 gas mixtures at one atmosphere total pressure. *Geol. Soc. Am. Bull.* **92**, (7_Part_II), 1039 (1981). doi:10.1130/GSAB-P2-92-1039

106. G. Kletetschka *et al.*, TRM in low magnetic fields: A minimum field that can be recorded by large multidomain grains. *Phys. Earth Planet. Inter.* **154**, 290 (2006). doi:10.1016/j.pepi.2005.07.005

107. S. Levi, M. T. Merrill, A comparison of ARM and TRM in magnetite. *Earth Planet. Sci. Lett.* **32**, 171 (1976). doi:10.1016/0012-821X(76)90056-X

108. G. Acton *et al.*, Micromagnetic coercivity distributions and interactions in chondrules with implications for paleointensities of the early solar system. *J. Geophys. Res.* **112**, B03S90 (2007). doi:10.1029/2006JB004655

109. S. M. Cisowski, D. W. Collinson, S. K. Runcorn, A. Stephenson, M. Fuller, *Proc. Lunar Planet. Sci. Conf. 13th*, A691 (1983).

110. P. A. Selkin, J. S. Gee, L. Tauxe, W. P. Meurer, A. J. Newell, The effect of remanence anisotropy on paleointensity estimates: A case study from the Archean Stillwater Complex. *Earth Planet. Sci. Lett.* **183**, 403 (2000). doi:10.1016/S0012-821X(00)00292-2

111. J. Gattacceca *et al.*, On the efficiency of shock magnetization processes. *Phys. Earth Planet. Inter.* **166**, 1 (2008). doi:10.1016/j.pepi.2007.09.005

112. K. Nishiizumi, D. Elmore, P. W. Kubik, Update on terrestrial ages of Antarctic meteorites. *Earth Planet. Sci. Lett.* **93**, 299 (1989). doi:10.1016/0012-821X(89)90029-0

113. Y. Yu, L. Tauxe, Acquisition of viscous remanent magnetization. *Phys. Earth Planet. Inter.* **159**, 32 (2006). doi:10.1016/j.pepi.2006.05.002

114. T. Kohout, G. Kletetschka, M. Kobr, P. Pruner, P. J. Wasilewski, The influence of terrestrial processes on meteorite magnetic records. *Phys. Chem. Earth* **29**, 885 (2004). doi:10.1016/j.pce.2004.06.004

115. B. Baldwin, Y. Sheaffer, Ablation and breakup of large meteoroids during atmospheric entry. *J. Geophys. Res.* **76**, 4653 (1971). doi:10.1029/JA076i019p04653

116. C. B. Atkins, P. J. Barrett, S. R. Hicock, Cold glaciers erode and deposit: Evidence from Allan Hills, Antarctica. *Geology* **30**, 659 (2002). doi:10.1130/0091-7613(2002)030<0659:CGEADE>2.0.CO;2

117. D. J. Dunlop, K. S. Argyle, Thermoremanence, anhysteretic remanence and susceptibility of submicron magnetites: Nonlinear field dependence and variation with grain size. *J. Geophys. Res.* **102**, (B9), 20199 (1997). doi:10.1029/97JB00957

119. D. A. Crawford, P. H. Schultz, The production and evolution of impact-generated magnetic fields. *Int. J. Impact Eng.* **14**, 205 (1993). doi:10.1016/0734-743X(93)90021-X

119. E. Jarosewich, Chemical analyses of meteorites: A compilation of stony and iron meteorite analyses. *Meteoritics* **25**, 323 (1990). doi:10.1111/j.1945-5100.1990.tb00717.x

120. R. L. Parker, Ideal bodies for Mars magnetics. *J. Geophys. Res.* **108**, 5006 (2003). doi:10.1029/2001JE001760